Alma Mater Studiorum · Università di Bologna

DOTTORATO DI RICERCA IN

INGEGNERIA BIOMEDICA, ELETTRICA E DEI SISTEMI

Ciclo XXXII

Settore Concorsuale: 09/G2
Settore Scientifico Disciplinare: ING-INF/06

FRACTAL DESCRIPTORS FOR QUANTIFYING BRAIN COMPLEXITY IN MRI

Presentata da: **Chiara Marzi**

Coordinatore Dottorato:
Prof. Daniele Vigo

Supervisore:
Prof. Mauro Ursino

Co-supervisore:
Dott. Marco Giannelli

Esame finale anno 2020

Chiara Marzi: *MRI brain complexity: study, development and application of fractal descriptors,* © Ciclo XXXII

SUPERVISORS:
Prof. Mauro Ursino
Dott. Marco Giannelli

Alma Mater Studiorum - University of Bologna

Non è la conoscenza, ma l'atto di imparare; non il possesso ma l'atto di arrivarci, che dà la gioia maggiore. Quando ho chiarito e esaurito un argomento, mi ci allontano, per tornare nell'oscurità; l'uomo non soddisfatto è così strano, che se ha completato una struttura non ce la fa a restarci in pace, ma deve iniziarne un'altra. Immagino che si debba sentir così il conquistatore del mondo che, quando un regno è stato a malapena conquistato, si lancia subito verso un altro.

Karl Friedrich Gauss (1777-1855)

ABSTRACT

Magnetic Resonance Imaging (MRI) is the in vivo technique most commonly employed to characterize changes in brain structures. The conventional MRI-derived morphological indices are able to capture only partial aspects of brain structural complexity. Fractal geometry and its most popular index, the *fractal dimension* (FD), can characterize *self-similar* structures including grey matter (GM) and white matter (WM). Previous literature shows the need for a definition of the so-called fractal scaling window, within which each structure manifests self-similarity. This justifies the existence of fractal properties and confirms Mandelbrot's assertion that *"fractals are not a panacea; they are not everywhere"*.

In this work, we propose a new approach to automatically determine the fractal scaling window, computing two new fractal descriptors, i.e., the minimal and maximal fractal scales (mfs and Mfs). Our method was implemented in a software package, validated on phantoms and applied on large datasets of structural MR images.

We demonstrated that the FD is a useful marker of morphological complexity changes that occurred during brain development and aging and, using ultra-high magnetic field (7T) examinations, we showed that the cerebral GM has fractal properties also below the spatial scale of 1 mm. We applied our methodology in two neurological diseases. We observed the reduction of the brain structural complexity in SCA2 patients and, using a machine learning approach, proved that the cerebral WM FD is a consistent feature in predicting cognitive decline in patients with small vessel disease and mild cognitive impairment. Finally, we showed that the FD of the WM skeletons derived from diffusion MRI provides complementary information to those obtained from the FD of the WM general structure in T1-weighted images.

In conclusion, the fractal descriptors of structural brain complexity are candidate biomarkers to detect subtle morphological changes during development, aging and in neurological diseases.

CONTENTS

LIST OF FIGURES

LIST OF TABLES

ACRONYMS

2D	two dimensional
3D	three dimensional
AD	Alzheimer's disease
ADC	apparent diffusion coefficient
ADT	apparent diffusion tensor
ALS	amiotrophic lateral sclerosis
AMICO	accelerated microstructure imaging via convex optimization
AxD	axial diffusivity
bvFTD	behavioral variant FTD
BW	bandwidth
CAA	cerebral amyloid angiopathy
CADASIL	cerebral autosomal dominant arteriopathy with subcortical infarcts and leukoencephalopathy
CSF	cerebrospinal fluid
CT	cortical thickness
CV	cross validation
D	diffusion
DK	diffusional kurtosis
DKI	diffusional kurtosis imaging
DT	diffusion tensor
DTI	diffusion tensor imaging
EEG	electroencephalography
EPVS	enlarged perivascular spaces
eTIV	estimated total intracranial volume
FA	fractional anisotopry
FD	fractal dimension
FLA	flip angle

FLAIR	axial fluid attenuation inverse recovery
fMRI	functional MRI
FOV	field of view
FTD	fronto-temporal dementia
G	Gaussian curvature
GA	gestational age
GM	grey matter
H	mean curvature
IACRS	inherited ataxia clinical rating scale
ICARS	international cooperative ataxia rating scale
ICBM	International Consortium for Brain Mapping
IFS	iterated function system
KT	kurtosis tensor
LASSO	least absolute shrinkage and selection operator
MAE	mean absolute error
MARS	microbleed anatomical rating scale
MCI	mild cognitive impairment
MD	mean diffusivity
mfs	minimal fractal scale
Mfs	maximal fractal scale
MO	mode of anisotropy
MRI	magnetic resonance imaging
MS	multiple sclerosis
MSA	multi system atrophy
MSA-C	multi system atrophy of type c
NEX	number of excitations
NKI2	Nathan Kline Institute - Rockland Sample Pediatric Multimodal Imaging Test-Retest Sample
NODDI	neurite orientation dispersion and density imaging

nfvPPA	non fluent variant PPA
OCD	obsessive-compulsive disorder
PPA	primary progressive aphasia
RD	radial diffusivity
ROI	region of interest
SCA1	spinocerebellar ataxia of type 1
SCA2	spinocerebellar ataxia of type 2
SCA3	spinocerebellar ataxia of type 3
SCA6	spinocerebellar ataxia of type 6
SCZ	schizophrenia
sMRI	structural MRI
SRM	standardised response mean
SVD	small vessels disease
svPPA	semantic variant PPA
TBI	traumatic brain injury
TBSS	tract based spatial statistics
Td	diffusion time
TE	echo time
TI	inversion time
TR	repetition time
VBM	voxel based morphometry
VMCI	vascular MCI
WM	white matter
WMH	white matter hyperintensities
WS	Williams syndrome

INTRODUCTION

"The human brain is probably the most complex system in the Universe" (Gandolfi, 2008). Indeed, the human brain possesses the emerging properties of complex systems. A complex system, although it cannot be defined univocally, can be described, using a more practical approach, through some of its characteristics. It has a *high number of elements* (millions or billions), whose *interactions are often non-linear*, have *delayed effects* and *positive and negative feedback*; it has a *network structure*, in which the different elements show *partial autonomy* and *differentiated sensitivity*. There is often a *systemic hierarchy* with *phenomena of self-organization*. A complex system is *open*, *dynamic* and *robust*, *creative* and *innovative*, *unpredictable* and *universal* (complexity is not confined to a scale of magnitude); it shows *discontinuous behaviour* (alternating periods of stability and chaotic instability) and for this reason it is *not easily controllable*.

The human brain has a high level of structural and functional complexity, in continuous evolution, changing during the lifespan.

Morphological alterations of brain structures are present in many neurological diseases and Magnetic Resonance Imaging (MRI) is the in vivo technique employed as a reference for the characterization of these changes. Currently, their evaluation in MR T1-weighted and diffusion-weighted imaging (DWI) is mainly performed by measuring brain atrophy (both globally and locally) and diffusion-tensor-derived indices, respectively. However, these indices capture only some partial aspects of brain morphology and are not able to describe its real complexity, which emerges from multiscale phenomena. Fractal geometry is a mathematical framework able to characterize complex structures, such as the cortical grey matter (GM) and subcortical white matter (WM); a structure is defined fractal if presents mathematical or statistical self-similarity and its fractal dimension (FD), typically computed using the 3D box counting algorithm, is a measure of the structural complexity of the object. The use of concepts of fractal analysis in neuroimaging shows the need of the definition of a specific interval of spatial scales (called "fractal scaling window"), in which the GM or WM, like any other biological structure, manifests *self-similarity*. That definition is a fundamental prerequisite for the assessment of fractal dimension, justifies the existence of fractal properties and confirms Mandelbrot's assertion that *"fractals are not a panacea; they are not everywhere"*.

For these reasons, my Ph.D. thesis concerns the study of existing fractal indexes and the design of new fractal descriptors able to concisely express the morphological complexity of brain structures observed in MR. In addition, in this thesis, the design and implementation of a software package for the automated computation of these fractal indices has been proposed. All these activities have been carried out through parallel computing procedures, necessary for the analysis of extended datasets of MR images.

The contents of this thesis are organized as follows.

Chapter 1 contains the theoretical concepts of fractal geometry, with a particular attention to the various definitions of fractal dimension. In particular, the box-counting algorithm, used to calculate the fractal dimension, is described in detail.

Chapter 2 deals with the state-of-the-art about fractal analysis in the neuroimaging. The first works that hypothesized that the human brain possesses fractal properties are accurately described. Similarly, the studies in which the fractal dimension has been proposed for the investigation of the brain development and aging and of neurological diseases are presented. In Chapter 2, the main methodological issues about the application of fractal analysis in neuroimaging are also described.

Chapter 3 is the core of the Ph.D. thesis. It includes the improvement of the 3D box-counting algorithm through the automated selection of the fractal scaling window, in which the human brain manifests fractal properties. In the first part of the chapter, a procedure to automatically select the fractal scaling window is proposed. In the second part, the software implementation is illustrated and validated on phantoms and healthy human brains.

Chapter 4 describes the results of fractal analysis in three neurological diseases: spinocerebellar ataxia of type 2 (SCA2), small vessels disease (SVD) and cerebral amyloid angiopathy (CAA). The study of patients with CAA was made possible thanks to the collaboration with the Stroke Research Center, Massachusetts General Hospital, Department of Neurology at Harvard Medical School in Boston.

Chapter 5 concerns the study of brain complexity in diffusion-MRI images. It includes the description of the most popular models used in the processing of DWI images (DTI, Diffusion Tensor Imaging; DKI, Diffusional Kurtosis Imaging; NODDI, Neurite Orientation Dispersion and Density Indexes). Then, the study of brain complexity using fractal analysis on DTI-derived skeletons, is finally presented.

1

THE FRACTAL GEOMETRY

This chapter contains the theoretical concepts of fractal geometry, with a particular attention to the different definitions of fractal dimension. In particular, the box-counting algorithm, used to calculate the fractal dimension, is described in detail.

1.1 THE FRACTAL DIMENSION

1.1.1 *What is a fractal object?*

Looking at the Nature, the chaotic order in which most of the elements manifest themselves is surprising. They are a representation of highly eclectic and complex forms and their description using simple models, belonging to the Euclidean geometry, such as lines, planes, spheres, etc., could be difficult and in some cases incomplete. If the Earth can be imagined as a sphere and its orbit of revolution as an ellipse, also the "spongiform" aspect of a cloud, the endless roses of a Roman broccoli, the ramifications of a tree and the structure of the circulatory system, can be described through the fractal geometry. In other words, the fractal geometry allows to generalize and model irregular and very complex phenomena, which can follow simple mathematical laws on different viewing scales (Mandelbrot, 1982).

Examples of fractal objects

Some examples of pure fractal objects are the Koch snowflake (Fig. 1a), the Peano curve (Fig. 1b), the Sierpinski triangle (Fig. 1c), the Menger's sponge (Fig. 1d) and the Mandelbrot's set (Fig. 1e).

The objects represented above are ideal fractals, synthetically constructed through simple recursive algorithms. An easy way to generate fractal forms is to repeat a transformation or a function for a high number of times (ideally infinite) (Falconer, 2004). With this procedure, named IFS (Iterated Function System), an object that is

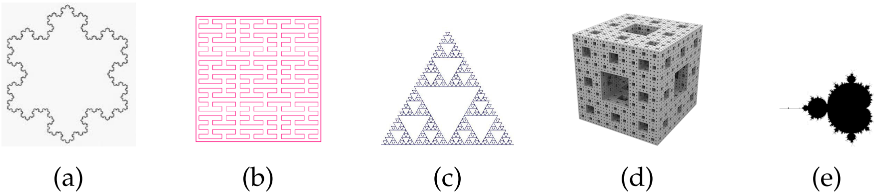
(a) (b) (c) (d) (e)

Figure 1: Examples of pure fractal objects: (a) the Koch snowflake, (b) the Peano curve, (c) the Sierpinski's triangle, (d) the Menger's sponge and (e) the Mandelbrot set.

initially very simple, evolves into a structure (or in a system) with complex characteristics, dynamically chaotic. The final object is difficult to be interpreted with the rules of traditional geometry and mathematics, which could be actually used to describe the initial state of the system. Therefore, a fractal object can be thought as the last stage (e.g., the attractor) of an IFS, that is the object to which the initial state tends when the number of transformations is repeated a sufficient number of times. An example of IFS algorithms for the construction of the Dragon Curve and the Sierpinski triangle is represented in Fig. 2.

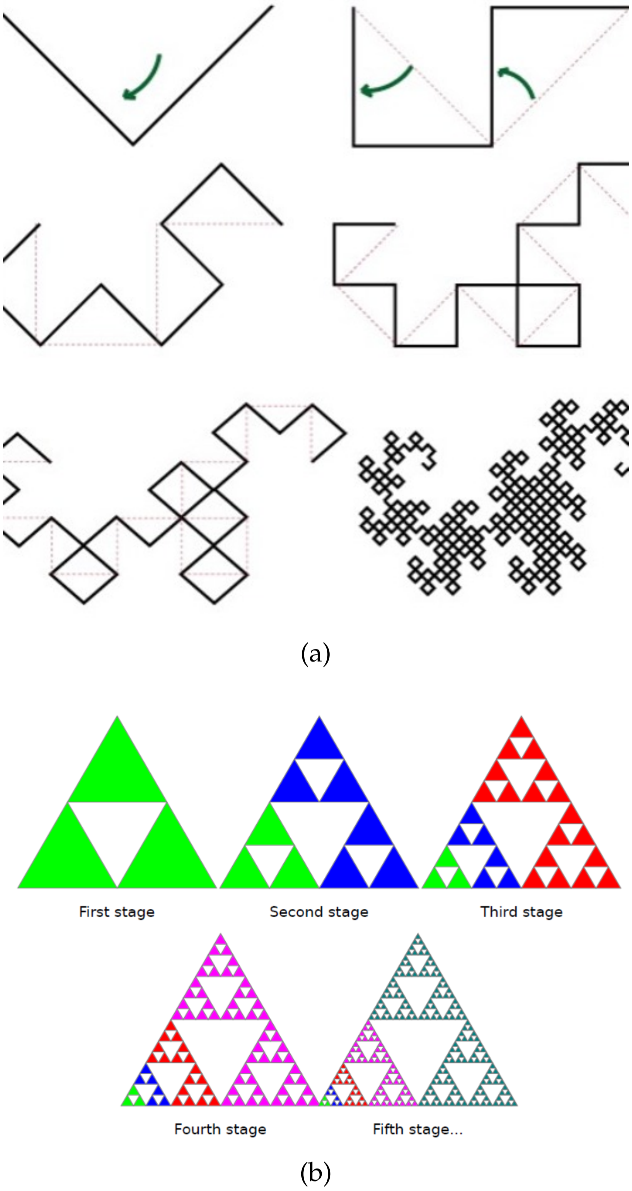

Figure 2: Example of IFS algorithm to build (a) the Dragon Curve and (b) the Sierpinski triangle.

On the contrary, the fractal objects observed in Nature show only roughly fractal properties, because their scaling features are not ideal over infinite viewing scales. Romanesco broccoli, trees and ferns are examples of natural fractal objects (Fig. 3).

Figure 3: Examples of natural fractal objects. From left to right, respectively, a Romanesco broccoli, a tree and a fern.

One question arises: what is the exact definition of fractal object? The fractal geometry was formalized in the seminal book "The Fractal Geometry of Nature" in 1982 (Mandelbrot, 1982), by the polish mathematician Benoit B. Mandelbrot (1924-2010), who ordered concepts and ideas already circulating previously. However, he did not succeed in coining a unique definition of a fractal object. Initially, any element that had fractional fractal dimension (see section 1.1) was considered a fractal object, as opposed to those with integer topological dimension. Indeed, the name "fractal" derives from the Latin "fractus", i.e., broken, in part, not intact. Then, the Mandelbrot's set (Fig. 1e) showed a fractal dimension of 2, thus in contrast with the previous definition (Shishikura, 1998). A more appropriate way to define a fractal object is to describe it as an object with some of the following properties (Falconer, 2004):

Properties of fractal objects

1. too irregular to be described in traditional Euclidean geometric terms;
2. detailed at any viewing scale;
3. self-similar in some sense (exact, approximate or statistical);
4. its Hausdorff-Besicovitch dimension is greater than its topological dimension (see section 1.1.5);
5. its construction uses a simple recursive algorithm.

As we will see in section 2.1, according to some of these five characteristics, also the human brain can be considered a fractal structure and thus analyzed and rediscovered under a new light, that of the fractal geometry.

1.1.2 *The Richardson's dimension*

A first definition and measure of *fractal dimension* has been proposed by Lewis Fry Richardson (1881 - 1953). He had the intention of evaluating the relationship between the war outbreak between two neighbouring countries and the length of the common boundaries. He realized how the value of the measured perimeter increases as the unit of measure decreases: analyzing and computing the perimeter of the boundaries with a compass from the opening increasingly smaller allows, in fact, to capture details, indentations and concavities that are not visible at larger viewing scales.

Let us suppose to measure the length of the coast of the island of Majorca with different units of measurement s and to represent each pairs of values in a logarithmic plot. If $s = 28$ km, a perimeter of 362.2 km is obtained; however, if $s = 14$ km, then the length of the coast assumes the value of 416.7 km. Decreasing the viewing scale s to 7 km and then to 3.5 km, the perimeter corresponds to 467.7 km and 524.8 km, respectively. If the viewing scale s becomes even smaller, the length increase indefinitely, giving rise to the *Richardson's effect*.

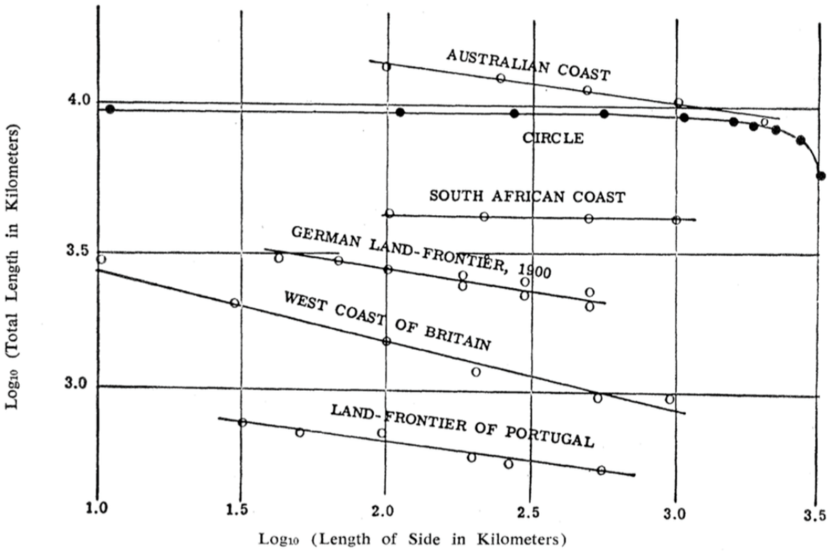

Figure 4: Logarithm plot showing the relationship between the length of the boundaries of a nation and the measurement unit.

The experimental samples represented in Fig. 4 show a linear relationship:

$$\log l = -d * \log s + \log c = d * \log(1/s) + \log c = d * \log(1/s) + k \quad (1)$$

Richardson's dimension

with:

l = measured perimeter;

s = viewing scale, unit of measurement;

d = Richardson's dimension;

$k = \log c$ = the intercept with the ordinate axis.

The linearity shown in the logarithmic scale is an important aspect, because it allows to describe a very complex phenomenon by relying on the simplest rules and functions of linear algebra. The equation 1 can be expressed as an exponential function between l and s in which d is the exponent, on a natural scale, following a few straigthforward steps:

$$\begin{aligned} \log l &= d * \log(1/s) + k = \log(1/s)^d + \log c = \log{(1/s)^d} * c \\ e^{\log l} &= e^{\log s^{-d} * c} \\ l &= c * s^{-d} \qquad (2) \end{aligned}$$

1.1.3 *The self-similarity dimension*

In the case of strictly fractal objects (see e.g., Fig. 5), which meet the constraint of exact *self-similarity* on multiple scales of observation (conceptually infinite), it is feasible to compute the *self-similarity dimension*. A fractal object, as mentioned in section 1.1.1, can be broken down in smaller and smaller parts, each one containing the same number of structural elements of the entire object, i.e., a representation in miniature (Sagan, 1994). Let us consider an object having Euclidean dimension E and divide it in n elements, each one reduced by a factor s in each dimension. In this way we get a number of elements n equal to $\frac{1}{s}^E$. We can repeat this procedure over and over again to obtain an object in which one portion has exactly the same shape of the whole structure. Notwithstanding, this object "alives" on a different scale. The relationship between the number of parts which constitutes each partition and the size of the viewing scale (i.e., the reduction factor), in accordance with the above equation, can be expressed in a logarithmic form as follows:

$$\log n = D_s * \log(1/s) \qquad (3)$$

where:

Self-similarity dimension

n = number of elements contained in each partition;

s = reduction factor;

D_s = *self-similarity dimension*.

Observing the Fig. 5, in which some steps needed to generate the fractal objects described in section 1.1.1 are shown, it is clear that their *self-similarity dimension* generally assumes fractional values, except in some cases (see section 1.1.1).

As can be seen in Fig. 5a, each step of the Koch snowflake construction procedure corresponds to the division of an initial segment into four parts ($n = 4$), each one of length equal to a third ($s = 1/3$) of that of the initial segment. Then, applying equation 3, the *self-similarity dimension* of the Koch snowflake is:

Self-similarity dimension of the Koch snowflake

$$\begin{aligned} \log 4 &= D_s * \log 3 \\ D_s &= \log 4 / \log 3 = 1.2619 \end{aligned} \tag{4}$$

Similarly, for the Peano curve (Fig. 5b), $n = 9$ and $s = 1/3$. Thus, the similarity dimension is:

Self-similarity dimension of the Peano curve

$$\begin{aligned} \log 9 &= D_s * \log 3 \\ D_s &= \log 9 / \log 3 = 2 \end{aligned} \tag{5}$$

In the case of the Sierpinski's triangle (Fig. 5c), $n = 3$ and $s = 1/2$ and the *self-similarity dimension* becomes:

Self-similarity dimension of the Sierpinski triangle

$$\begin{aligned} \log 3 &= D_s * \log 2 \\ D_s &= \log 3 / \log 2 = 1.585 \end{aligned} \tag{6}$$

In the Menger's sponge (Fig. 5d), example of a fractal object in three dimensions, each one of the twenty "cubes" ($n = 20$) occupies a volume which is nine times smaller ($s = 1/3$) than that at of the previous step:

Self-similarity dimension of the Menger's sponge

$$\begin{aligned} \log 20 &= D_s * \log 3 \\ D_s &= \log 20 / \log 3 = 2.7268 \end{aligned} \tag{7}$$

1.1.4 *Relationship between Richardson's and self-similarity dimension*

When a structure presents the *self-similarity* property in a mathematical sense, the *Richardson's dimension* (see section 1.1.2) and the *self-similarity dimension* (see section 1.1.3) are intrinsically related according to the Equation 8. In fact, using the equations 1 and 3, if $l = n * s$, we obtain:

$$\begin{aligned} \log l &= \log n + \log s \\ &= \log c - d * \log s \\ \log n + \log s &= \log c - d * \log s \\ \log n &= \log c - d * \log s - \log s \\ &= \log c - (d+1) * \log s \\ &= \log c - D_s * \log s \\ D_s &= d + 1 \end{aligned} \tag{8}$$

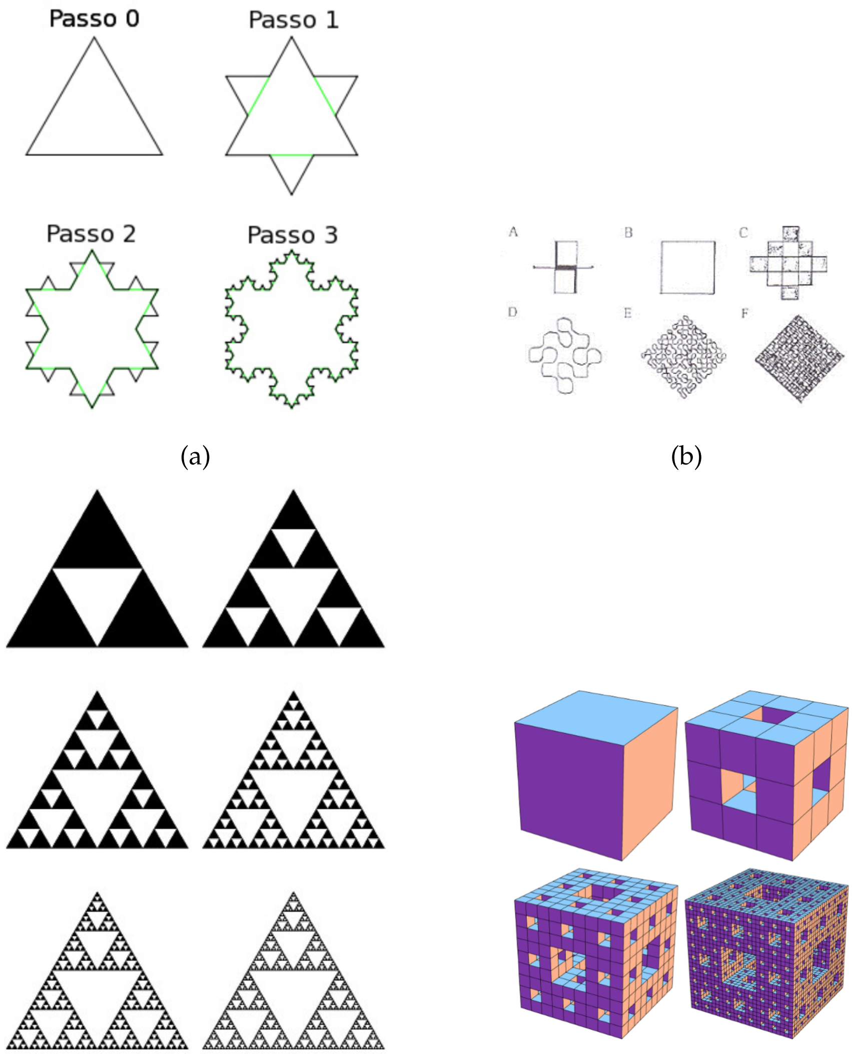

(a) (b)

(c) (d)

Figure 5: Construction of self-similar fractal objects: (a) 4 steps of the construction of the Koch snowflake, (b) 6 steps of the construction of the Peano curve, (c) 6 steps of the construction of the Sierpinski's triangle and (d) 4 steps of the construction of the Menger's sponge.

1.1.5 *The Hausdorff-Besicovitch dimension*

The *Hausdorff-Besicovitch dimension* is an important definition of fractal dimension, because it is based on the theory of measurement and it can be applied to any set of points, not just to self-similar ones. We define the *Hausdorff-Besicovitch dimension* based on the formalism presented by Kenneth Falconer in "Fractal Geometry: Mathematical Foundations and Applications" (Falconer, 2004). Let U be a non-empty subset of the Euclidean space $\mathbb{R}^n$: $U \subset \mathbb{R}^n$; the diameter of U is represented by the greatest distance between two points contained in U: $|U| = \sup\{|x-y| : x, y \in U\}$. If $\{U_i\}$ is a finite collection of points, whose diameter value is smaller than a certain value δ, $0 \leqslant |U_i| \leqslant \delta \, \forall i$, covering F, i.e., $F \subset \bigcup_{i=1}^{+\infty} U_i$, then the collection $\{U_i\}$ is a δ-cover of F. Let us suppose that F is a subset of $\mathbb{R}^n$, $F \subset \mathbb{R}^n$, and s is a non-negative number, $s \geqslant 0$; $\forall \delta \geqslant 0$, we define $H^s_\delta(F) = \inf\{\sum_{i=1}^{+\infty} |U_i|^s \; : \; \{U_i\}$ is δ-cover of $F\}$. The equation above looks at all covers of F by sets of diameter smaller or equal than δ and minimize the sum of the s-th powers of the diameters. As δ decreases, the number of possible covers of F is reduced, thus the s−dimensional *Hausdorff measure* of F, $H^s(F)$, is defined as the limit as $\delta \to 0$ of $H^s(F)$:

$$H^s(F) = \lim_{\delta \to 0} H^s_\delta(F) \tag{9}$$

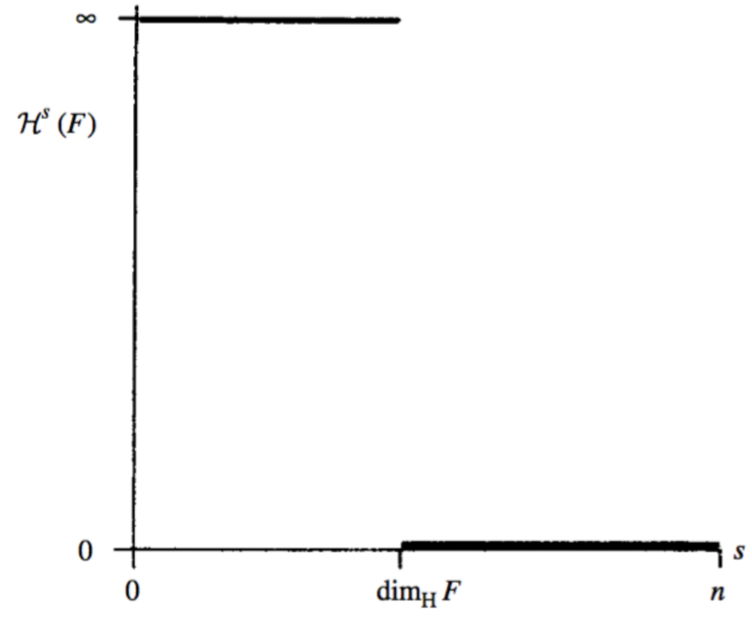

Figure 6: $H^s_\delta(F)$ as function of s (Falconer, 2004).

If $\delta < 1$, $H^s_\delta(F)$ is non-increasing with s, then $H^s(F)$ is also non-increasing; we can see the usual trend of $H^s(F)$ against s in Fig. 6: for some $s < s^* = \dim_H F$, $H^s(F) \to +\infty$, while for $s > s^* = \dim_H F$, $H^s(F) \to 0$. The critical value of s at which $H^s(F)$ "jumps" from $+\infty$ to 0 is the so-called *Hausdorff dimension* $\dim_H F$. Mathematically:

$$\dim_H(F) = \sup\{s \geqslant 0 : H^s(F) = +\infty\} = \inf\{s \geqslant 0 : H^s(F) = 0\} \quad (10)$$

Hausdorff-Besicovitch dimension

with

$$H^s(F) = \begin{cases} +\infty & 0 \leqslant s < \dim_H(F) \\ 0 & s > \dim_H(F) \end{cases} \quad (11)$$

The *Hausdorff-Besicovitch dimension* described above is a solid basis for the description of the fractal dimension and is a starting point for the implementation of numerical algorithms that can compute the fractal dimension. To clarify the real meaning of this measure, we introduce the following example. Let us calculate the *Hausdorff-Besicovitch dimension* $\dim_H(Q)$ of a square Q:

- if one tries to cover Q with segments, by placing $s = 1$, the number of objects required to fill the entire square Q is infinite, thus $H_s(F) = +\infty$;
- if, on the other hand, one covers Q it with cubes, by setting $s = 3$, the number of elements needed to fill the square Q is null, thus $H_s(F) = 0$;
- finally, choosing $s = 2$, i.e., trying to determine the *Hausdorff-Besicovitch dimension* with elements that "live" in a two-dimensional space, such as the square Q, the number of objects needed for covering Q assumes a certain value k. Thus, $H_s(F) = k$, which represents the minimum cover of Q, according to Lebesgue's theory (Falconer, 2004).

The proposed example is a particular case of an object in two dimensions, but the *Hausdorff-Besicovitch dimension* concept can be easily generalized in several dimensions. It represents the exponent who "matches" the right amount of space occupied by the object under examination, whether it is a regular geometric shape, or a fractal object. In the case of an object, for example, whose *Hausdorff-Besicovitch dimension* is equal to 2,7268, it shows that the space occupied is greater than that of a surface (topological dimension equal to 2) but smaller than that of a volume (topological dimension equal to 3).

1.1.6 *The Minkowski-Bouligand dimension*

The definition of fractal dimension proposed by Minkowski and Bouligand, is a fundamental step between the theoretical definitions and the numerical implementations of the fractal dimension. Minkowski and Bouligand have introduced their measure on the basis of the various considerations set out in the previous sections. In order to calculate the *Minkowski-Bouligand dimension* of a generic object let us superimpose a grid, consisting of boxes (or cubes) with known length side r, on that structure, and count the number of boxes (or cubes) $N(r)$, which overlap with the object. This operation is then repeated for different values of r. The *Minkowski-Bouligand dimension* is expressed as the limit for d tending to 0 of the ratio between the logarithm of the number of boxes covering the structure $N(r)$ and the logarithm of the box size r:

$$D_{MB} = \lim_{d \to 0} \frac{\log N(d)}{\log(1/d)} \tag{12}$$

Minkowski-Bouligand dimension

where:

$N(r)$ = counts of the boxes of lenght side r that overlap with the object;

r = side length of the box,

D_{MB} = *Minkowski-Bouligand dimension*.

1.2 THE BOX-COUNTING ALGORITHM

The *box counting* algorithm is the most common procedure for calculating the fractal dimension of real objects. It descends from the Hausdorff-Besicovitch dimension (Katsaloulis et al., 2009) as well as it is an implementation of the Minkowski-Bouligand dimension. The widespread use of this algorithm derives from the following factors:

1. is a fully automatic procedure (Foroutan-poor et al., 1999);
2. is an algorithm that can be easily implemented on a computer (Foroutan-poor et al., 1999; Katsaloulis et al., 2009);
3. is a method applicable to a wide range of structures, because there is no the requirement of self-similarity in a strict sense (Foroutan-poor et al., 1999; Katsaloulis et al., 2009; Zhang et al., 2007b).

The *box counting dimension*, henceforth referred to as fractal dimension (FD) (Goni et al., 2013), is obtained by superimposing on the object under examination a grid consisting of boxes with side length ϵ and counting the number of boxes $N(\epsilon)$ containing at least part of the structure (Landini et al., 1995; Smith et al., 1996); the procedure is then repeated for different side values ϵ, as shown in Fig. 7.

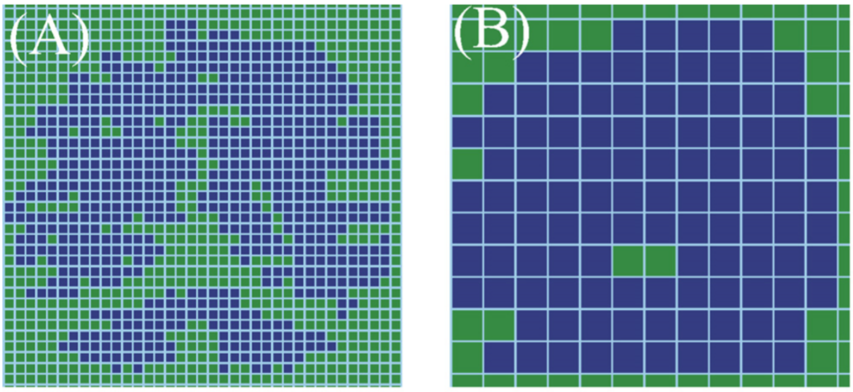

Figure 7: Example of a 2D box-counting procedure. A grid with boxes having side length ϵ is overlapped to a WM segmentation. $N(\epsilon)$ is the number of boxes required to cover the structure (blu boxes) (Zhang et al., 2007b).

The number of boxes $N(\epsilon)$ needed to cover the entire object is a function of the box size ϵ (Smith et al., 1996) and represents the number of counts $N(\epsilon)$ against the side length of the box ϵ in a bilogarithmic plot. Thus, performing a linear regression model, we obtain a line whose slope (in module) represents the FD (equation 13):

$$FD = \frac{\log \epsilon_0 - \log N(\epsilon)}{\log \epsilon} \tag{13}$$

where $\log \epsilon_0$ is the intercept of the regression line and ϵ_0 is usually referred as prefactor (Mandelbrot, 1982).

The box-counting fractal dimension

2

THE FRACTAL DIMENSION OF THE BRAIN

Over the last decades, the fractal geometry has been used as a universal tool for the analysis and quantification of the morphological complexity of natural objects, including the human brain (Di Ieva et al., 2015). It has been used and is currently performed in different biological fields (see Di Ieva et al., 2015 for a complete review), regarding, for example, the microcirculation of the human brain (Minnich et al., 2001; Cassot et al., 2006; Heinzer et al., 2006; Lauwers et al., 2008), the retinal microvascularization (Cavallari et al., 2011; Cheung et al., 2013; Doubal et al., 2010; Jiang et al., 2013; Kawasaki et al., 2011; Ong et al., 2013; Tălu, 2011), the EEG analysis (Ahmadlou et al., 2010; Ahmadlou et al., 2011; Michail et al., 2010), the nuclear medicine perfusion imaging (Michallek and Dewey, 2013) and the cerebral hemodynamic signals in functional MRI (fMRI) (Herman et al., 2001; Panerai, 2009; Olejarczyk, 2007; Bullmore et al., 2004; Li and Huang, 2014; Rubin et al., 2013).

The fractal analysis of the brain in the structural neuroimaging field (sMRI) is complementary to conventional morphometry techniques, which aim to quantify morphological changes in different brain structures (e.g., the GM) by measuring volume, cortical thickness (Salat et al., 2004), area, sulcal depth (Panizzon et al., 2009), curvature (Pienaar et al., 2008) and gyrification index (Van Essen et al., 2006).

In the first part of this chapter, I will describe how the human brain can be considered *fractal*, *fractal-labelled* (Avnir et al., 1998; Mandelbrot, 1998) or *pre-fractal* (Feder, 1988), revisiting the first authors who analyzed the brain morphological complexity in sMRI. Then, I will present studies on the fractal dimension of the brain in healthy subjects and in neurological diseases.

2.1 IS THE BRAIN A FRACTAL STRUCTURE?

The brain can be imagined as a network composed of interconnected components. The theory of fractal geometry has been demonstrated to be a powerful tool for quantifying its complexity (Di Ieva et al., 2015).

2.1.1 *The cerebral cortex*

As initially suggested by Mandelbrot (Mandelbrot, 1982) and later measured by Majumdar and Prasad (Majumdar and Prasad, 1988), the highly folded cortical surface, i.e., the cerebral gray matter, is similar to a 2D sheet, that, folding on itself, fills a 3D space, thus showing a fractal dimension more than 2, but less than 3 (Fig. 8).

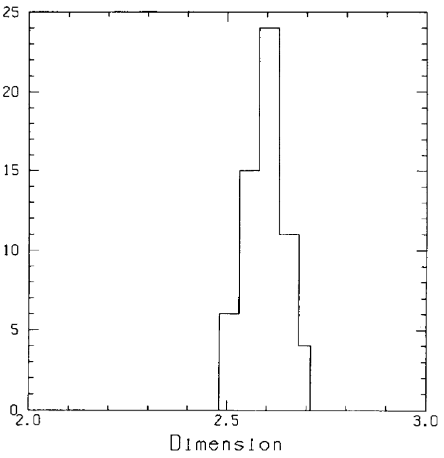

Figure 8: An example of the histogram of 65 fractal dimension measurements obtained from transverse, sagittal, and coronal sections of the human brain. The mean fractal dimension is 2.60 (Majumdar and Prasad, 1988).

Hofman (1991), drawn by those previous works, was the first who really showed that the whole brain cortex manifests fractal features. The human brain, indeed, performing a great number of complex functions with a minimum expenditure of material for the construction of the system, is highly folded and irregular and is not completely described by the ideal constructs of Euclidean geometry (Hofman, 1991). The cortical folding is due to the increase of the surface area beyond that expected for geometrically similar objects of different volumes (Jerison, 1982; Todd, 1984; Hofman, 1989).

In classical scaling theory, any series of similar objects show a surface area proportional to the square of a length dimension, whereas they showed a volume proportional to the cube (Gould, 1971). According to this geometric principle, also known as Galileo's principle of *similitude* (Thompson, 1915; Thompson, 1942; Armstrong and Falk, 1982), the surface area is proportional to the two-thirds power of volume:

$$area = k * volume^{(2/3)} \tag{14}$$

with:

k = scaling constant;

2 = topological dimension of a surface;

3 = topological dimension of a volume.

The equation 14 can be generalized in the form $area = k * volume^{(D/3)}$, where D is a general measure of the filled space, and, for the cerebral cortex, assumes, experimentally, fractional values (Fig. 9).

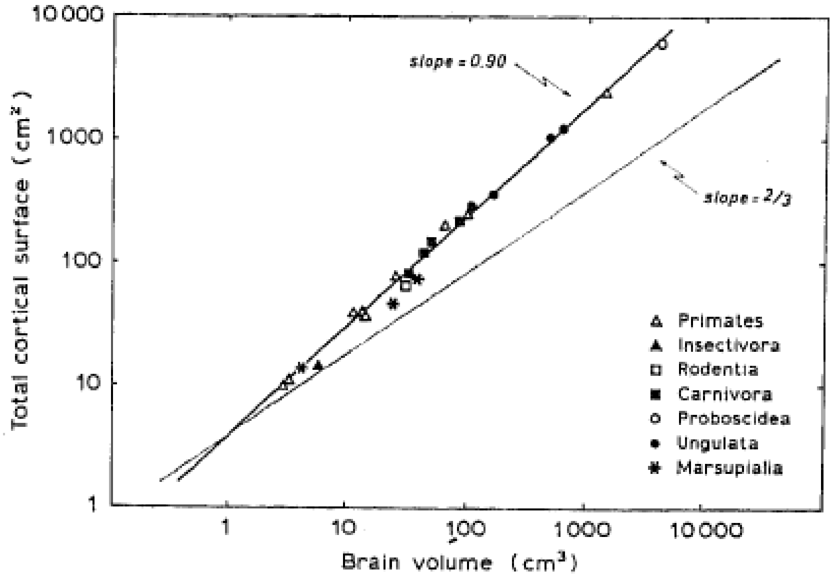

Figure 9: The total cortical surface area as a function of brain volume in mammals. The dashed line represents the surface-volume relation of a purely geometric objects: an Euclidean hemisphere where $area = 3.84(volume)^{\frac{2}{3}}$. The solid line in the standard major axis ($\alpha = 0.90 \pm 0.012$), representing the surface-volume relation for convoluted brains. Note that the cortical surface area of species with convoluted brains ($area > 10cm^2$), rather than being proportional to 2/3 power of geometric similarity, is nearly a linear function of brain volume (Hofman, 1991).

For a human brain, Hofman found experimentally $D = 2.70$ (Hofman, 1991). In general, D is a number that tells us something about the overall structure and complexity of an object (Mandelbrot, 1982; Stanley and Ostrowsky, 1986; Morse et al., 1985). The empirical area-volume relation, for example, found in (Hofman, 1991) indicates that the cortical surface is partly space-filling and that its surface area fractally evolves into a volume, or that its volume, by fractal folding, attains the property of an area (Hofman, 1991).

A fractal model of the brain

Moreover, Hofman, in his work, generated a fractal object having the form and the fractal dimension similar to those of a folded brain (10). In a two-dimensional space, dividing the side of a regular hexagon into three segments ($N = 3$) of length equal to four ninths of the initial length ($r = 4/9$), the final attractor morphologically resembles an axial view of the human brain. The self-similarity dimension, applying the equation 3, is equal to $D = \log 3/\log(9/4) = 1.3548$. A similar procedure in 3D space, with a decahedron as initiator, yelds a fractal dimension equal to 2.7095, a value very close to that computed experimentally (Hofman, 1991).

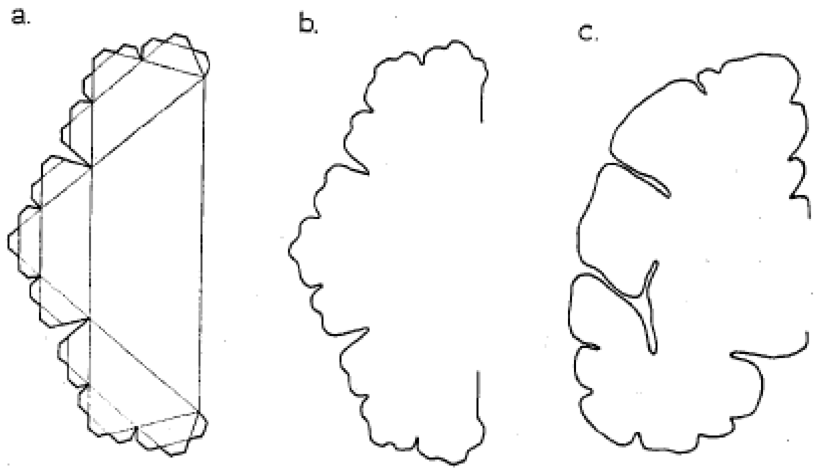

Figure 10: A fractal model of the mammalian brain (Hofman, 1991).

Free and others (Free et al., 1996) and Kiselev and others (Kiselev et al., 2003), albeit using different algorithms to compute the 3D fractal dimension of the cerebral cortex, confirmed that the human brain shows fractal properties and that the fractal dimension is a quantitative descriptor of cortical convolutions and could detect morphological abnormalities and subtle global changes in the folding structure associated with abnormal brain development and neurodegeneration (Free et al., 1996; Kiselev et al., 2003).

2.1.2 *The cerebral WM*

Hofman has shown that also the WM, sharing the GM/WM interface surface with the cerebral cortex, has itself fractal properties (Hofman, 1991). Thereafter, other works confirmed the results, analyzing either the GM/WM interface surface (Bullmore et al., 1994; Cook et al., 1995; Sato et al., 1996; Free et al., 1996), the general structure, or the skeleton of the WM (Zhang et al., 2006). To the best of our knowledge, the latter (Zhang et al., 2006) is the first work that analyzed, at the same time, the general structure, the contour and the skeleton of the WM by the fractal analysis, asserting that significant structural changes may occur also beneath the surface (within the structure) (Zhang et al., 2006). They found a fractal dimension value between 2 and 3 for each WM structure (general strucure, contour and skeleton) in two groups of young and elder healthy subjects, as we will detail in section 2.2.

2.1.3 *The cerebellar GM and WM*

For the same reasons, also the cerebellum has fractal properties. A few works in literature have analyzed the GM and WM of the cerebellum by fractal analysis. Rybaczuk and Kedzia (Rybaczuk and Kedzia, 1996; Rybaczuk et al., 1996) evaluated the cerebellum surface complexity, by measuring the FD in adult and fetal brains, while Liu *et al.* (Liu et al., 2003), since the shape of the cerebellar WM is well represented by its skeleton, evaluated the fractal properties of the its skeleton in 24 young and healthy subjects. They showed a mean fractal dimension equal to 2.57, a fractional value between 2 and 3, as for the cerebellar WM.

2.1.4 *Theoretical and methodological issues*

Fractals fulfil a certain number of theoretical and methodological criteria including a high level of organization, shape irregularity, functional and morphological self-similarity, scale invariance, iterative pathways and a peculiar non-integer FD (Losa, 2014). The application of these criteria inevitably leads to theoretical and methodological issues, that the previous literature has tried to overcome in very different ways. In this section, I will briefly present some of these problems, so that the reader can better understand previous studies concerning fractal analysis of the healthy and diseased brain, as well as the need to deepen, understand and, finally, harmonize fractal analysis in neuroimaging.

Fractal scaling window

Whereas mathematical objects are deterministic invariant or self-similar over an unlimited range of scales, biological components are statistically self-similar only within a fractal domain defined by lower and upper limits, called *fractal scaling window*, in which the relationship between the viewing scale and the measured size or length of the object can be established (Losa and Nonnenmacher, 1996; Losa, 2014). Biological elements do indeed express statistical self-similar patterns and fractal properties within a defined interval of scales and this is because the size of the elementary constituents of biological systems (cells) is not very different (in orders of magnitude) from the size of a complete structure or organism. Therefore, when the morphology of a biological fractal is investigated under increasing magnification, the 'increasing detail' vanishes at some point in this process, and the geometry of the structural components (cells, membranes, etc) becomes apparent (Landini and Rigaut, 1997). In this so called fractal scaling window, a direct relationship between the viewing scale and the measured size/length of an object can be ascertained and in turn quantified by a peculiar FD (Losa and Nonnenmacher, 1996). In other words, the fractal dimension of a biological component remains constant within the fractal scaling window (Dollinger et al., 1998; Losa, 2002) and serves to quantify variations in length, area or volume with changes in the dimensions of the measuring unit (Losa, 2014).

The fractal scaling window in Neuroimaging

In a certain number of reports (Blanton et al., 2001; Esteban et al., 2007; Esteban et al., 2009; Ha et al., 2005; Kalmanti and Maris, 2007; King et al., 2010; Madan and Kensinger, 2016; Mustafa et al., 2012; Narr et al., 2004; Rajagopalan et al., 2013; Rajagopalan et al., 2019; Sandu et al., 2008; Sandu et al., 2014a; Sheelakumari et al., 2017; Squarcina et al., 2015; Thompson et al., 1998; Thompson et al., 2005; Wu et al., 2009; Zhang et al., 2008), for a better understanding see the sections 2.2 and 2.3, the fractal dimension was evaluated fitting a regression line to all data points and determining the slope of this line, without the scaling domain being established or, sometimes, with only the lower bound scale shown on the loglog plot (corresponding to the maximal resolution scale) being checked (Losa, 2014; Jelinek et al., 2005). In some works the linear region has also been calculated by determining the local slopes: one method for this, described by Caserta in 1995, is to calculate the n-points local slopes, as the difference in $\log N(r)$ divided by $\log r$ for every n successive points. The region in which the local slopes are constant is then taken as the linear region (Caserta et al., 1995; Jelinek et al., 2005). Another method to choose the fractal scaling window is to select only a portion of the data points, fitting more than one regression line to the data points and taking the average of several slopes along the data points (Jelinek and Fernández, 1998). These methods are all valid alternatives for estimating the fractal dimension, but may result in different values (Jelinek and Fernández, 1998).

Points not uniformly distributed in the bi-logarithm plot

Another important problem is how the line of best fit is obtained from the data to determine the slope and hence the fractal dimension. In some works, the points are not uniformly spaced in the bi-logarithm plot, because the authors have chosen to increase r values, from r_{min} to r_{max} using the natural scale; since in that case the linear regression model is built on an interval of points not equally spaced in the logarithmic plot (and therefore with different "weight" in the linear fitting), this is not an entirely trivial operation (Russ, 1994). In more recent works, computing the fractal analysis via the box counting algorithm, the boxes (cubes in 3D) sizes have been scaled as a power of 2 and are therefore evenly spaced in the bi-logarithm plane (Jelinek and Fernández, 1998).

General structure, contour or skeleton?

The last issue we encounter concerns the choice of the shape/structure under consideration. The brain, for example, can be studied in its general structure, the contour only or its skeletonized shape. Even in this context, the fractal analysis will lead to different results and, in particular, the previous literature showed that skeletonised images had consistently lower fractal dimension values.

The lower estimated fractal dimension values for skeletonised images are a result of removing one of the main contributions to image complexity, that is the border ruggedness and the space filling effect of the cell interior (Jelinek and Fernández, 1998).

2.2 THE FRACTAL DIMENSION OF THE HEALTHY BRAIN

The discovery of the fractal properties of the brain has given a series of studies on the morphological complexity in healthy subjects. They include the employment of the fractal dimension as a new index in neuroimaging (Im et al., 2006; Goni et al., 2013), for the analysis of morphological changes in the brain during the normal development (Blanton et al., 2001; Sandu et al., 2014a) and aging (Kalmanti and Maris, 2007; Madan and Kensinger, 2016; Zhang et al., 2007b; Farahibozorg et al., 2015) and for the possible association between brain morphological complexity and cognitive abilities (Mustafa et al., 2012; Sandu et al., 2014b).

Im and colleagues in 2006 (Im et al., 2006) analyzed the fractal properties of the GM cortical surface in 44 healthy subjects (mean age ± standard deviation 26.4 ± 5.5 years), by means of the 3D box-counting algorithm and demonstrated that the FD expresses a quantitative estimate of gyrification, condensing in a single value the sulcal depth, the frequency of folding, and the convolution of gyral shape (Im et al., 2006). For example, a high value of FD could unveil a thinner and more convoluted cortical surface.

A few years later, Goni and colleagues (Goni et al., 2013) have investigated the reproducibility of the FD at varying some parameters of the box-counting algorithm. They used two different datasets consisting respectively of 50 healthy subjects aged 24 ± 3.2 years (3 sessions of scanning for each subject) and 24 healthy subjects aged 57 ± 8.6 years (4 sessions of scanning for each subject). They have shown how the value of FD of not ideal fractal structures (e.g., the cortical ribbon, the WM volume, the pial surface and the GM/WM interface surface) varies according to the positioning of the origin of the exploratory grid. For this reason, they proposed the use of a random offset on the origin of the grid and the repetition of the procedure for 20 different random offsets. The average value of the 20 counts was proved to be a more stable and reproducible estimate for the computation of the box-counting FD (Goni et al., 2013).

To the best of our knowledge, the FD of the brain has not yet been studied at varying the the static magnetic field intensity B_0. Still there are no studies that investigated associations between the FD of the cerebral end cerebellar WM and more traditional morphological measures (e.g., volume, area, etc..).

GM FD during the lifespan

Let us focus on the use of FD as a potential marker of morphological subtle changes both in the GM and WM during the entire lifespan. Several works have shown that the GM cortical complexity, as measured by different implementations of the FD, consistently decreased with of age (Kalmanti and Maris, 2007; Sandu et al., 2014a; Madan and Kensinger, 2016). Kalmanti et al., (Kalmanti and Maris, 2007) found a significant negative correlation between the 2D box-counting FD values and age, in a range spanning from 3 months to 78 years. The same results have been confirmed using a 3D box-counting algorithm. Indeed, Sandu and colleagues (Sandu et al., 2014a) have found higher FD values in a group of 17 healthy adolescents (aged 14.1 ± 0.27) than in a group of 17 healthy adults (aged 24.24 ± 2.76), while Madan and Kensinger (Madan and Kensinger, 2016) have shown a significant negative correlation between the FD values of the cortical ribbon and age in 427 healthy subjects aged from 20 to 86 (see Fig. 11). Blanton et al., (Blanton et al., 2001), in a population of healthy children aged 6-16 years, revealed a significant positive association between FD and age in frontal regions, likely reflecting ongoing maturation processes such as myelination and synaptic remodeling that continue into the second decade of life.

WM FD during the lifespan

The association between FD values and age from adulthood has been analyzed also in the WM structure : the WM can be studied as its general structure (the WM volume), the skeleton and the boundary (the GM/WM interface surface) (Zhang et al., 2007b; Farahibozorg et al., 2015). Zhang *et al.*, demonstrated that the FD of the general structure and the skeleton present significantly higher values in a group of 24 healthy young subjects, aged 17-35 (27.7 ± 4.4) compared with those calculated for a group of 12 healthy old subjects, aged 72-80 (74.8 ± 2.6) (Zhang et al., 2007b). Farahibozorg *et al.*, studied 209 healthy subjects aged 20-80 years (49.31 ± 15.5) extracted from the IXI ("Information eXtraction from Images") database (http://brain-development.org/ixi-dataset/). They found an increase of FDs of the general structure and the skeleton from young to mid-age, and a faster decrease from mid-age to the old (see Fig. 12) (Farahibozorg et al., 2015).

The fractal dimension of the WM was also studied in relation to cognitive functions in a sample of healthy subjects belonging to the "Aberdeen 1936 Birth Cohort" dataset. Mustafa and colleagues (Mustafa et al., 2012) studied the WM in 217 healthy subjects aged 68 years and they found that individual differences in fractal measures of the brain are significantly associated with lifelong cognitive changes and independent of the influence of sex and WM volume. They have proposed the fractal measures (complexity) as a descriptor of structural maturation. In fact, subjects with greater brain complexity have greater fluid abilities than would be expected

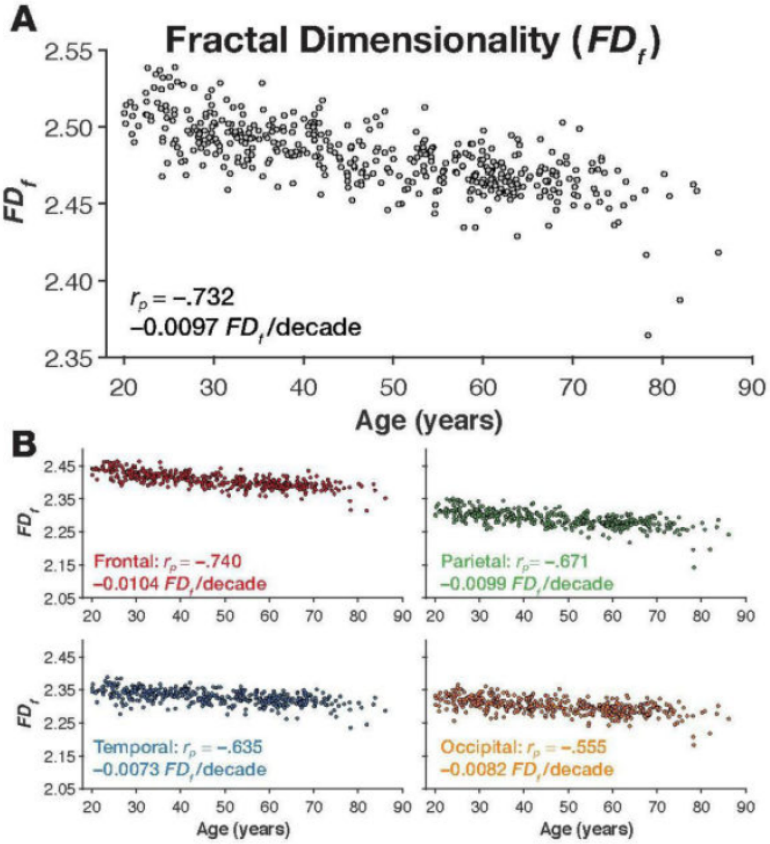

Figure 11: Fractal dimension for the individuals in the IXI dataset. Panel A shows the scatter plot of age and FD for the cortical ribbon, along with the correlation and slope. Scatter plots of age and FD for each lobe, are shown in panel B, along with the respective correlations and slopes (Madan and Kensinger, 2016).

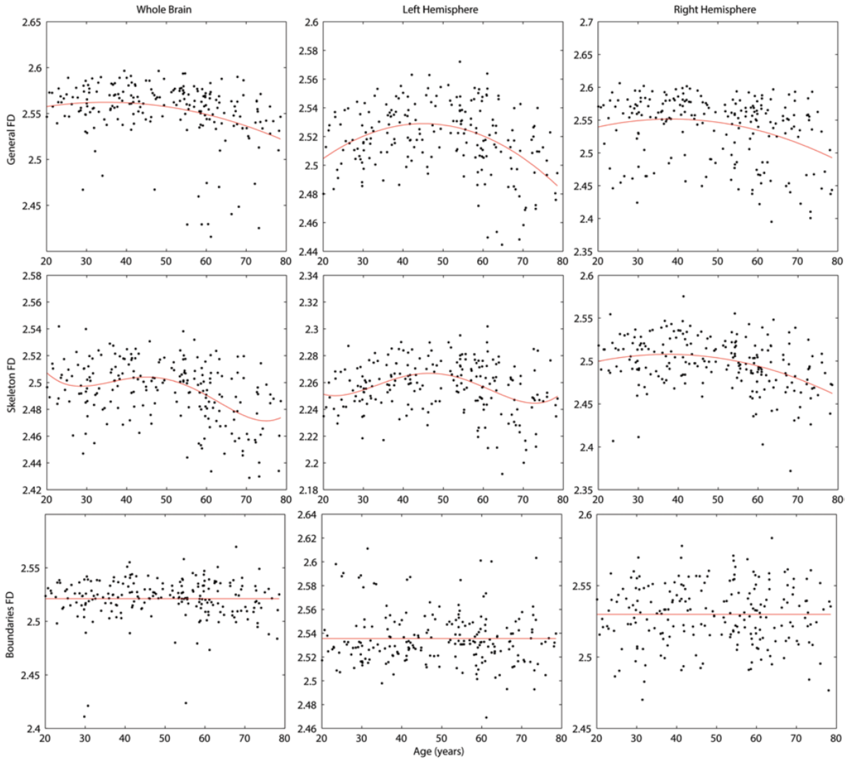

Figure 12: Patterns of changes of the general, skeleton, and boundary fractal dimensions (FDs) of the whole brain and left and right hemisphere with age (years). The black point sets represent the actual data points; the solid fit curves are the polynomials as detected by Akaike InformationCriterion model selection and fitted by polyfit.m function in MATLAB (Farahibozorg et al., 2015).

from childhood intelligence measures and smaller estimated decline at age 68 years (Mustafa et al., 2012). The same sample of subjects has been used in another longitudinal study by Sandu et al., (Sandu et al., 2014b). They studied 245 healthy subjects aged 68 years and 148 of these have been re-analyzed after five years. They showed that FD values significantly decrease between 68 and 73 years old subjects and that greater WM complexity was associated with retention of cognitive ability across the life course and individual differences in ability in late life. They finally suggested that *"FD is a measure of resilience to cognitive decline and those with less structural complexity may be more vulnerable to cognitive decline, mild cognitive impairment and dementia"* (Sandu et al., 2014b).

2.3 THE FRACTAL DIMENSION OF THE DISEASED BRAIN

The application of fractal analysis of MRI in patients with neurological diseases has provided results of potential diagnostic significance. In particular, the FD has been shown to be more accurate than other methods (e.g., volumetric voxel-based morphometry) for the detection of morphological changes in several diseases and for identifying different clinical phenotypes (Di Ieva et al., 2015).

Fetal subjects

Wu and colleagues (Wu et al., 2009) showed the effectiveness of FD in assesing normal and abnormal maturation of cortical development in 44 MR images of fetal subjects ranging from 22 to 36 weeks of gestational age (GA). They showed that the increase of cortical complexity is highly correlated with fetal developing weeks of GA, with a more rapid FD increase after 28 weeks of GA, because of faster development of convolved folds, while both the twins and subjects with cortical dysplasia presented a lower FD than that in normal cases (Wu et al., 2009). Similar results have been figured out by De Luca *et al.*, who proved that fractal indices are able not only to characterize the alterations induced by malformation of cortical development, but also to distinguish the healthy tissue of pathologic brains from the malformed areas (De Luca et al., 2016).

William syndrome

Thompson and colleagues compared 42 subjects with genetically confirmed William Syndrome (WS) and 40 age-matched healthy controls, with traditional and fractal morphological analysis. The WS is a genetic disorder caused by the deletion of about 27 genes from the long arm of one of the two chromosome 7s. While in WS cortical thickness was increased by 5-10 % only in a circumscribed right hemisphere perisylvian and inferior temporal region, the surface complexity was significantly increased in the overall cerebrum (Thompson et al., 2005).

Schizophrenia

Other authors revealed changes of cortical folding in patients with schizophrenia (SCZ), which were not evident with conventional MRI morphometric methods (Di Ieva et al., 2015). Sandu and colleagues used MRI data of 7 patients with SCZ and 6 healthy subjects. They showed that patients had larger FD values for the whole brain and right hemisphere than controls (Sandu et al., 2008). Since the value was reduced in patients, they supposed that loss of brain tissue most likely resulted in a shrinking of the pial surface with an increase in cortical microfoldings. The same results have been figured out by Narr et al., (Narr et al., 2004), who examined gyral complexity in 50 patients experiencing their first episode of schizophrenia compared with 50 demographically matched healthy comparison subjects. They found that male patients were shown to exhibit significant increases in gyral complexity in right superior frontal cortices, compared with healthy male subjects. Different results have been obtained by Ha et al., (Ha et al., 2005) and Squarcina et al., (Squarcina et al., 2015). The formers computed the 3D FD of skeletonized cerebral cortical surface of 50 patients with schizophrenia, 45 patients with obsessive-compulsive disorder (OCD) and 26 healthy normal controls. They found that the schizophrenic group had a significantly smaller mean FD than OCD group, and the OCD group smaller than the control group. It should be noted that the brain FD reflecting cortical complexity or pattern did not correlate with any of tissue volume measures in controls and schizophrenics, suggesting that 3D FD of cortical surface may be a sensitive index for the investigation of the structural brain abnormalities in mental disorders, especially those developmentally disturbed. In recent years fractal analysis has been used to distinguish groups of schizophrenics with different symptoms (Nenadic et al., 2014) and to assess morphological abnormalities of subcortical GM (Zhao et al., 2016). Nenadic and colleagues (Nenadic et al., 2014) analyzed a sample of 87 patients with DSM-IV schizophrenia, divided into three subgroups based on sympton profiles and each group was compared with 108 matched healthy controls. Their findings suggest that regional heterogeneity of cortical folding complexity might be related to biological subgroups of schizophrenia with differing degrees of altered cortical development pathology. With regard to morphological abnormalities of subcortical structures, although we believe that fractal analysis is not adequate to describe such regular and smooth forms, Zhao et al., (Zhao et al., 2016) found a significant reduction of FD in left hippocampus, the right hippocampus as well as left thalamus, in 19 schizophrenia patients, as compared to 19 healthy individuals.

Traumatic brain injury

Traumatic brain injury (TBI) is a major cause of death and disability worldwide, especially in children and young adults. Rajagopalan and colleagues analyzed 17 individuals with moderate to severe TBI and 13 healthy controls with traditional morphological analysis (i.e., whole brain WM volume, GM volume, cortical thickness, cortical area), diffusion tensor imaging (DTI) metrics and fractal analysis (Rajagopalan et al., 2019). Only the FD was significantly different (lower) between the TBI group and healthy subjects. No other significant difference in either whole brain WM volume, GM volume, cortical thickness, cortical area or DTI-derived metrics was observed in any of the brain regions between TBI and healthy controls. In addition, WM FD accounted for a significant amount of variance in executive functioning and processing speed, measured by a neuropsychological test battery sensitive to cognitive impairment associated with TBI.

Multiple sclerosis

It has been demonstrated that changes in both WM (Esteban et al., 2007) and GM (Esteban et al., 2009) are well characterized by the FD in MRI scans of patients with multiple slerosis (MS). Esteban and colleagues showed that FD allows to detect some fundamental differences in brain architecture, providing a global measurement of morphological changes induced by neurological diseases such as MS (Esteban et al., 2007). Indeed, WM (including the normal appearing WM) FD is decreased in patients with MS, both at the GM/WM boundary (WM border) and at the internal structure of the WM (WM skeleton) of the entire brain. Although lesions involving the WM are well recognized in MS disorder, recent studies have indicated extensive damage of the GM in MS, including microglia activation, cortical demyelination, and axonal, synaptic, and neuronal loss. Two years later, Esteban *et al.*, found that patients with MS had a significant increase in the FD of the cerebral GM compared to controls and that this alteration appears early in the course of the disease (Esteban et al., 2009).

Amyotrophic lateral sclerosis

Another kind of sklerosis, the amyotrophic lateral sclerosis (ALS), also known as motor neuron disease due to the death of neurons controlling voluntary muscles, has been deepened by Rajagopalan *et al.*, using both voxel based morphometry (VBM) and fractal analysis applied on WM structures (skeleton, surface and general structure) (Rajagopalan et al., 2013). No significant VBM WM changes were observed between ALS patients and controls and among the ALS subgroups. In contrast, significant FD reductions in skeleton and general structure were observed between ALS with dementia and other ALS subgroups. Their results suggest that WM shape complexity is more sensitive to ALS disease process when compared to VBM analysis and that FD changes are dependent on the ALS phenotype. The correlation analysis between FD and clinical measures suggests that FD could potentially serve as a biomarker of ALS pathophysiology.

Stroke

The fractal dimension has been also used to describe the changes in WM complexity in patients with stroke. A lower FD value, indicating a reduced WM complexity, has been detected in the stroke-affected hemisphere, while no significant correlations were observed when motor function was related to lesion volume (Zhang et al., 2008).

Dementia

Dementia is the loss of cognitive functioning—thinking, remembering, and reasoning—and behavioral abilities to such an extent that it interferes with a person's daily life and activities. Different types of dementia exist. The fractal analysis has been applied to the most frequent type of dementia, i.e., the Alzheimer's disease (AD) (Thompson et al., 1998; King et al., 2009; King et al., 2010) and to the frontotemporal dementia (FTD) (Sheelakumari et al., 2017).

Alzheimer's disease

The Alzheimer's disease has been broadly investigated via traditional morphometry analysis (King et al., 2010; Di Ieva et al., 2015). Only a few studies have quantified the brain complexity in patients with AD using fractal analysis (Thompson et al., 1998; King et al., 2009; King et al., 2010). In the first work, King *et al.*, used a small sample of AD patients (n=15) and healthy subjects (n=15), taken from the public "Alzheimer's Disease Neuroimaging Initiative" (ADNI) database (King et al., 2009). They showed that the mean FD of the cortical ribbons from AD patients was lower than age-matched controls, demostrating that FD is complementary to volumetric measures and may assist in identifying disease state or disease progression. Moreover, in a second study containing more subjects from ADNI database, the FD has been computed for three cortical models (the pial surface, GM/WM surface and entire cortical ribbon) (King et al., 2010). The fractal dimension of the cortical ribbon and GM/WM surface showed highly significant differences between AD patients and healthy controls, while no significant difference between the two groups was found in the pial surface. As figured out in previous works (Im et al., 2006; King et al., 2009), the FD is complementary to other morphological metrics and all three models had a significant positive correlation with the cortical gyrification index (r=0.55, p<0.001). Only the cortical ribbon had a significant correlation with cortical thickness (r=0.832, p<0.001). In addition, the cortical ribbon FD showed a larger effect size ($d = 1.12$) in separating control and mild AD subjects than cortical thickness (d=1.01) or gyrification index (d=0.84) (King et al., 2010).

Frontotemporal dementia

Frontotemporal dementia is a young-onset dementia with focal atrophy of frontal and anterior temporal lobes leading to characteristic change in personality and social conduct. The three clinical syndromes include the most common frontal variant of FTD (bvFTD) and two language variants: semantic dementia (svPPA) and progressive nonfluent aphasia (nfvPPA) which is collectively known as primary progressive aphasia (PPA) (Sheelakumari et al., 2017). Sheelakumari and colleagues investigated the GM (skeleton, surface and general structure) morphometric abnormalities in the behavioral variant FTD (bvFTD) and primary progressive aphasia (PPA)

(Sheelakumari et al., 2017). They found that patients with bvFTD had a significant reduction in FD values of the skeleton and general structure when compared to controls. In PPA, a more significant decrease in FD was noted in the whole brain and left hemisphere skeleton along with the left hemisphere general structure.

Multiple system atrophy

Multiple system atrophy of the cerebellar type (MSA-C) is a degenerative neurological disease of the central nervous system. The FD analysis of MRI scans using the box-counting method has been demonstrated to be superior to conventional volumetric methods (i.e., fractal analysis produces smaller variances and less gender effect); patients with MSA-C exhibited significantly lower FD values in both cerebellar WM and GM, suggesting a degeneration of the cerebellar structure (Wu et al., 2010; Di Ieva et al., 2015).

Also in the case of literature dealing with neurological diseases, fractal analyses often differ in the method used, algorithmic implementation and parameters, leading to results, although potentially useful, not directly comparable.

The message we can get from the previous literature on fractal analysis in neurological diseases is that, regardless of the actual calculation of the fractal dimension, fractal analysis is often stronger and more accurate in the morphological description of brainnas compared to traditional morphological indices.

3

THE AUTOMATED SELECTION OF THE FRACTAL SCALING WINDOW

In this chapter, we will present an optimized approach for the computation of the fractal dimension of brain structures. In particular, we have focused on the selection of the fractal scaling window, in which the object under examination can be defined as fractal. In the first part of the chapter, a procedure to automatically select the fractal scaling window will be shown; in the second part, the software implementation will be presented.

As we have already figured out in section 2.1.4, mathematical fractal objects are self-similar over an unlimited range of spatial scales. On the contrary, natural objects, including the human brain, exhibit this property over a limited spatial range only. This fractal domain is defined by upper and lower limits, called *fractal scaling window* and it is the range in which the relationship between the viewing scale and the measured size can be established (Losa and Nonnenmacher, 1996; Losa, 2014).

Previous works (Kiselev et al., 2003; Goni et al., 2013; Madan and Kensinger, 2016) suggested to select a priori the range/interval of spatial scales of the fractal scaling window. In particular, Kiselev et al., analyzing the cerebral cortex of 6 healthy subjects, set the superior limit of the spatial scales equal to the brain size and their results suggested to set the inferior limit to 3 mm, corresponding reasonably well to the cortical thickness (Kiselev et al., 2003). Still, Goñi et al. calculated the FD of the pial surface, the segmented cortical ribbon and the WM volume extracted from MR T1-weighted images. They chose an *a priori* fractal scaling window range within 5 - 40% of the smallest Euclidean dimension of the object under examination (Goni et al., 2013). These choices might be all valid alternatives, but, to the best of our knowledge, nobody really knows the exact fractal scaling window of the brain for a given subject. The employment of a range of spatial scales selected *a priori* seems quite arbitrarily and may also impact on the FD values.

For these reasons, we propose an improved box-counting algorithm with automated selection of the fractal scaling window (Marzi et al., in preparation).

3.1 METHODS

The 3D box-counting algorithm

Let $I(x, y, z)$ be a binary image, e.g., the segmentation of the cortical ribbon mask; the fractal dimension of $I(x, y, z)$ is calculated through the 3D box counting algorithm (Russell et al., 1980): a grid containing 3D cubes of side r is superimposed on $I(x, y, z)$, and the number of boxes (cubes) $N(r)$ needed to fully cover the object is counted. The procedure is repeated for various r values (Fig. 13); in order to prevent the systematic influence of the grid placement on the object contained in $I(x, y, z)$ (Falconer, 2004; Feder, 1988; Barnsley, 1988), for each r, 20 uniformly distributed random offsets were applied on the grid origin and all the box counts (one for each offset) have been averaged to obtain a single $N(r)$ value (Goni et al., 2013). If $I(x, y, z)$ is a fractal object, the data points of $N(r)$ versus r in a log-log plane may be well modeled by a linear function, whose slope (with a negative sign) represents the FD (Mandelbrot, 1982). This linear relationship in the log-log plane corresponds, in the natural scale, to a power law $N(r) = k * r^{-FD}$, where FD is the exponent (with a negative sign) and k has been denoted as prefactor by Mandelbrot (Mandelbrot, 1982). Since the linear regression is computed in a log-log plane, the box counting algorithm was executed using a uniform sampling of the spatial scales in the log-log plane, which corresponds to an exponential sampling in the natural scale, i.e., using $r = 2^k$ mm, with $k = [0, 1, ..., k_{max}]$, where k_{max} is the exponent value to obtain the maximum image size; e.g., $k = 8$ for a 256x256x256 image size.

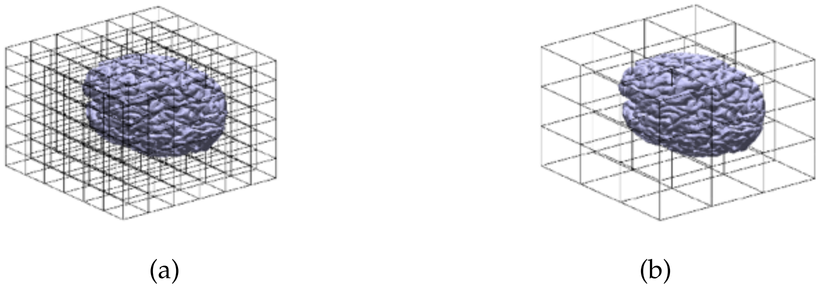
(a) (b)

Figure 13: In the box counting algorithm, a grid containing 3D cubes of side r is superimposed on the segmented brain portion (cerebral GM, cerebral WM, cerebellar GM and cerebellar WM) and the number of boxes (cubes) needed to fully cover the object is counted. This procedure is repeated for various r values uniformly distributed in a logarithmic scale ($r = 2^k$ voxels, where $k = 0, 1, ..., 8$). In panels (a) and (b), an example of the superimposition of the 3D grid using a small (r = 32 mm) and a large (r = 64 mm) r size is shown, respectively (Marzi et al., 2018a).

The automated selection of the fractal scaling window

As we have already mentioned above, in general, the range of spatial scales in which a structure manifests fractal properties is limited and unknown a priori. For this reason, we propose an automated selection of spatial scales where $I(x, y, z)$ manifests its fractal properties, based on the identification of the range of r values where the linear regression shows the highest coefficient of determination (adjusted for the number of data points) R^2_{adj}, as a goodness-of-fit indicator.

$$R^2_{adj} = 1 - \left[(1 - R^2) * \frac{n-1}{n-j-1} \right] \qquad (15)$$

with:

R^2 = coefficient of determination;

n = total number of points;

j = number of points used for the linear regression model.

The coefficient of determination R^2 has been chosen as a goodness-of-fit indicator because it describes the proportion of variance in the dependent variable, i.e. the counts $N(r)$, that is predictable from the independent variable, i.e. the measurement size r. Moreover, we computed the coefficient of determination adjusted for the number of point, R^2_{adj}, because it takes into account the phenomenon of the R2 increasing when the sample size of the explanatory variable increases.

To this purpose, the algorithm carries out the linear regression for each combination of minimum and maximum spatial scales allowed. We considered a minimum number of 4 data points, because it is reasonable to suppose that a window containing less than 4 points in the log-log plane (one of the worst cases is 3 points between 1 (i.e. 2^0) and 4 (i.e. 2^2) and so less than half decade) seems too short to define $I(x, y, z)$ a fractal object, which is described by the self-similarity property varying the spatial scale of observation (Losa and Nonnenmacher, 1996; Mandelbrot, 1998). Once the inferior and superior limits of the spatial scales range has been chosen automatically by the algorithm, the FD is computed as the absolute value of the slope of the regression line estimated within the selected spatial scales.

3.2 GREY AND WHITE MATTERS SEGMENTATION

As we have already mentioned in section 3.1, the fractal analysis proposed has been designed for binary images. For this reason, to perform fractal analysis on GM and/or WM. A preliminarly segmentation is required. We chose the software *FreeSurfer*, which is documented and freely available for download online (http://surfer.nmr.mgh.harvard.edu/). The technical details of these procedures are described in prior publications (Dale et al., 1999; Dale and Sereno, 1993; Fischl and Dale, 2000; Fischl et al., 2001; Fischl et al., 2002; Fischl et al., 2004a; Fischl et al., 1999a; Fischl et al., 1999b; Fischl et al., 2004b; Han et al., 2006; Jovicich et al., 2006;

Segonne et al., 2004; Reuter et al., 2010; Reuter et al., 2012). Briefly, this processing includes motion correction and averaging (Reuter et al., 2010) of multiple volumetric T1-weighted images (when more than one is available), removal of non-brain tissue using a hybrid watershed/surface deformation procedure (Segonne et al., 2004), automated Talairach transformation, segmentation of the subcortical white matter and deep gray matter volumetric structures (including hippocampus, amygdala, caudate, putamen, ventricles) (Fischl et al., 2002; Fischl et al., 2004a); intensity normalization (Sled et al., 1998), tessellation of the GM/WM boundary, automated topology correction (Fischl et al., 2001; Segonne et al., 2007), and surface deformation following intensity gradients to optimally place the GM/WM and GM/cerebrospinal fluid (CSF) borders at the location where the greatest shift in intensity defines the transition to the other tissue class (Dale et al., 1999; Dale and Sereno, 1993; Fischl and Dale, 2000). Once the cortical models are complete, a number of deformable procedures can be performed for further data processing and analysis including surface inflation (Fischl et al., 1999a), registration to a spherical atlas which is based on individual cortical folding patterns to match cortical geometry across subjects (Fischl et al., 1999b), parcellation of the cerebral cortex into units with respect to gyral and sulcal structure (Desikan et al., 2006; Fischl et al., 2004b), and creation of a variety of surface based data including maps of curvature and sulcal depth. This method uses both intensity and continuity information from the entire 3D MR volume in segmentation and deformation procedures to produce representations of cortical thickness, calculated as the closest distance from the GM/WM boundary to the GM/CSF boundary at each vertex on the tessellated surface (Fischl and Dale, 2000). The maps are created using spatial intensity gradients across tissue classes and are therefore not simply reliant on absolute signal intensity. The maps produced are not restricted to the voxel resolution of the original data thus are capable of detecting submillimeter differences between groups. Procedures for the measurement of cortical thickness have been validated against histological analysis (Rosas et al., 2002) and manual measurements (Kuperberg et al., 2003; Salat et al., 2004). Also, *FreeSurfer* morphometric procedures have been demonstrated to show good test-retest reliability across scanner manufacturers and across field strengths (Han et al., 2006; Reuter et al., 2012).

In all the analyses shown in this thesis, cortical reconstruction and GM/WM surfaces were manually inspected for defects. The correction techniques suggested by *FreeSurfer* developers, including editing of brain mask and WM and adding control points and rerunning of the *FreeSurfer* pipeline (https://surfer.nmr.mgh.harvard.edu/fswiki/FsTutorial/TroubleshootingData) were applied more than one time to assure that all defects were corrected. All views (coronal, sagittal, and axial) were used to confirm segmentation and surfaces reconstruction errors. Cerebellum segmentations were manually edited using a free-hand pencil using the Freeview utility, part of *FreeSurfer* suite.

3.3 THE SOFTWARE IMPLEMENTATION

One of the purposes of this thesis dissertation is the numerical implementation of the methods for computing the FD with the automated selection of the fractal scaling window. The block diagram represented in Fig. 14 shows the processing required to calculate the FD of a binary structure using a T1-weighted MR image of the human brain.

The box counting algorithm has been implemented on a Mac notebook (equipped with a dual-core Intel Core i7 processor, 16 GB of RAM memory). The code has been written in C++ language, using the ITK (Insight Segmentation and Registration Toolkit) image processing libraries (Ibanez et al., 2003). The linear regression with the automated selection of the fractal scaling window has been implemented in MATLAB R2014b, *The Mathworks, Inc., Natick, Massachusetts*. The C++ and Matlab programs have been interfaced with Bash scripts.

All experimental activities on phantoms and in-vivo and ex-vivo datasets as described in details in section 3.4) were performed on a Dell PowerEdge T620 platform equipped with two 8-core Intel Xeon E5-2640 v2, for a total of 32 CPU threads and 128 GB of RAM, using the Oracle Grid Engine parallel computing system.

3.3.1 *The box-counting algorithm*

The proposed box counting method is divided into three main sections:

1. setting the parameters for the execution of the box-counting algorithm;
2. execution of the box counting procedure;
3. generation of the output results.

In the first section, we determine the conditions under which the procedure will be executed, such as the choice of the number of the random positions (offsets) that the origin of the grid must assume (see section 3.1). The algorithm is implemented for isotropic binary 3D images.

The second section of the algorithm foresees the actual execution of the box-counting method for calculating the FD as defined in section

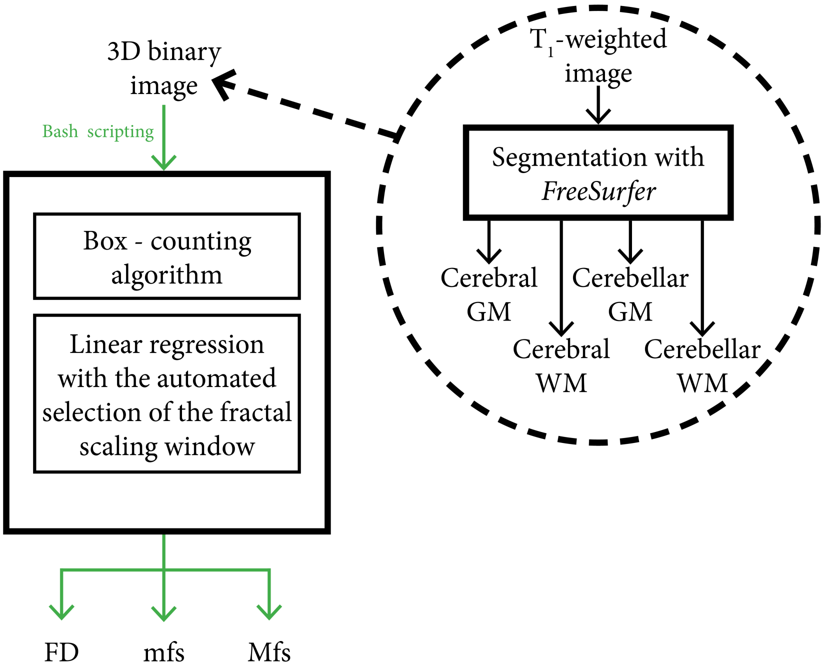

Figure 14: Architecture of the improved box-counting algorithm with automated selection of the fractal scaling window. In the dashed ellipsoid an example of 3D binary image starting from cerebral MR image.

3.1. The vector of the r values (i.e., the length of the grid cube side) is generated starting from the smallest observation window (i.e., $r = 1$ voxel) up to the maximum number of voxels contained in each axis, using an uniform sampling of the spatial scales in the log-log diagram (i.e., $r = 2^k$, with $k = [0, 1, ..., k_{max}]$, where k_{max} is the exponent value to obtain the maximum image size; e.g. $k = 8$ for a 256x256x256 image size). Since the user can choose the number of random offsets for positioning the origin of the exploration grid, the algorithm is able to calculate the mean values of all counts carried out for each r, indicated with N_FD_*ave*.

The last section of the algorithm collects the results in a text file containing the r values and the corresponding counts performed (N_FD_*ave*). The text file containing the results of the box counting method implemented in C++ language, it is then processed by an algorithm written in Matlab environment, as we will see in the following section.

3.3.2 *The automated selection of the fractal scaling window*

The counts calculated using the box-counting method are processed in Matlab environment to obtain the FD value as the slope (in absolute value) of the best linear regression line in the log-log plot.

The use of Matlab environment has allowed to easily represent the results both in a numerical and in a graphical form, for quality control. The linear regression model has been built by minimizing the error between the experimental points and the model using the least squares method. The choice of the spatial range in which the linear regression is performed can be manual or automated. In the former case, the user chooses the lower and upper value of the spatial range of interest. In the latter case, the linear regression algorithm is able to automatically determine the range of points where the object manifests optimal fractal properties, by maximising the value of the coefficient of determination R^2_{adj}(corrected for the number of points on which it is performed) (see equation 15), estimated for all possible combinations of intervals, containing at least a specified number of data points (see section 3.1).
Data and parameters used as inputs of the linear regression algorithm are the following:

- datafile: a text file containing the results of the C++ box-counting algorithm described above (see section 3.3.1);
- minWindowSize: the minimum number of data points of the fractal scaling window; minWindowSize should be $\geqslant 4$;
- stepWindowSize: the number of points of the increment of the fractal scaling window in the forthcoming iteration;
- mfs (minimal fractal scale): the lower bound of the fractal scaling window;
- Mfs (maximal fractal scale): the upper bound of the fractal scaling window;

In the case mfs and Mfs parameters are set to "[]", the choice of the range on which the linear regression is computed, is automatic; otherwise, the linear regression is performed only within that range defined *a priori*.

Once the linear regression of the selected data has been performed, the algorithm produces the following results:

- sel_mfs: the lower limit of the fractal scaling window automatically chosen for the calculation of the linear regression;
- sel_Mfs: the upper limit of the fractal scaling window automatically chosen for the calculation of the linear regression;
- FD: the fractal dimension, obtained as the absolute value of the slope of the linear regression line;

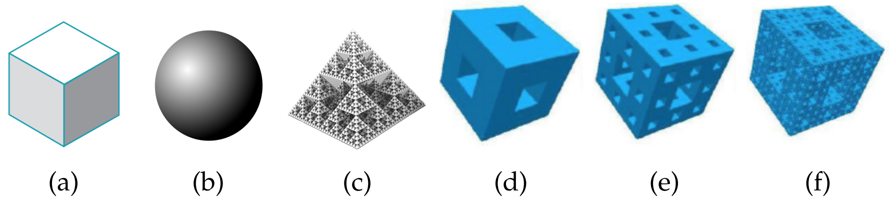

Figure 15: Synthetic volumetric images used to assess the accuracy in the measurement of FD of our improved 3D box counting algorithm with the automated selection of fractal scaling window; a) a filled cube and its surface, b) a sphere, c) the fractal pyramid, d), e) and f) are the 1-level, 2-level and 4-level, respectively, of the Menger sponge.

- Pref : the value of intersection of the regression line with the axis of the ordinates;

- R^2_{adj}: the coefficient of determination, adjusted for the number of points on which the regression has been performed. R^2_{adj} has been adopted to express the goodness of the fit in the selected fractal scaling window;

- EvaluateCounter: number of iterations performed, i.e. equal to the number of intervals in which the regression model was calculated.

3.4 VALIDATION

3.4.1 *Phantoms*

To assess the accuracy in the measurement of FD of our improved 3D box counting algorithm with the automated selection of fractal scaling window, the proposed implementation has been applied to five binary synthetic volumetric images including three 3D Euclidean and two 3D fractal objects: a cube, the surface of the same cube, a sphere, the fractal pyramid and the Menger sponge (Fig. 15).

In details:

1. a filled cube of size 128x128x128 voxels (image size 256x256x256 voxels);

2. the surface of the same cube;

3. a sphere with a diameter of 200 voxels (Madan and Kensinger, 2016);

4. the fractal pyramid: a 3D fractal object, based on a square pyramid, where each square pyramid is replaced by 5 half-size square pyramids. This procedure can be iteratively repeated for each of the sub-square pyramid, theoretically producing a

structure with infinite surface area, but zero volume. Here we constructed:

  a) a 6-level fractal pyramid (image size 256x256x256 voxels);

5. the Menger sponge: a 3D fractal object, based on a cube, where the cube is divided into a 9×9×9 grid and the middle sub-cubes from every face are removed, as well as the center-most sub-cube. Thus, of the 27 sub-cubes (i.e., 9^3), only 20 remain. This procedure can be iteratively repeated for each of the sub-cubes, theoretically producing a structure with infinite surface area, but zero volume. A cube can be considered a zero-level Menger sponge (Madan and Kensinger, 2016). Here, we used three Menger sponges:
   a) a 1-level Menger sponge with a width of 200 voxels (Madan and Kensinger, 2016);
   b) a 2-level Menger sponge with a width of 200 voxels (Madan and Kensinger, 2016);
   c) a 4-level Menger sponge with a width of 200 voxels (Madan and Kensinger, 2016);

The filled cube, the cube surface and the sphere are non-fractal objects; their theoretical Hausdorff-Besicovitch dimension is equal to their integer topological dimension, i.e., 3 for the cube and the sphere and 2 for the cube surface. On the other hand, the analytical Hausdorff-Besicovitch dimension of the fractal pyramid is $\log_2 5 = 2.3219$ and for the Menger sponge is equal to $\log_3 20 = 2.72$.

Table 1 shows that FD values computed using the automated selection of spatial scales were very similar to the theoretical Hausdorff-Besicovitch dimension, proving that the proposed algorithm allows an accurate measurement of FD within an absolute value of the percentage relative error < 7% . The coefficients of determination R^2_{adj} were very close to 1, demonstrating the excellent fit of the regression lines using the automated selection of spatial scales in the log-log plot.

3.4.2 *Healthy subjects*

In this section, we aimed at evaluating in-vivo the effect of different criteria in the selection of the interval of fractal spatial scales in the FD estimation of the cerebral cortex in T1-weighted MR images. For the validation of our algorithm (see section 3.1) and for the investigation of the healthy brain development and aging, we employed two public and international MRI datasets for a total of 163 healthy subjects, aged between 6 and 85 years.

Table 1: Theoretical Hausdorff-Besicovitch FD and FD measured through the algorithm using automated selection of spatial scales. Adjusted coefficients of determination R^2_{adj} are also reported, showing the excellent fit of the regression lines in the log-log plane.

Synthetic structure	Hausdorff-Besicovitch FD	Measured FD	Absolute percentage relative error (%)	R^2_{adj}
Cube	3	2.9226	2.58	0.9999
Cube surface	2	1.9994	0.03	1.0000
Sphere	3	2.93	2.33	0.9999
6-level fractal pyramid	2.32	2.2827	1.69	0.9999
1-level Menger sponge	2.73	2.92	6.96	0.9999
2-level Menger sponge	2.73	2.84	4.03	0.9997
4-level Menger sponge	2.73	2.56	6.22	0.9999

We compared four different strategies for the selection of the fractal scaling window, in which the human brain exibits fractal properties. The first two strategies have been taken from previous works (Kiselev et al., 2003; Goni et al., 2013; Madan and Kensinger, 2016), that suggested to select a priori the interval of spatial scales of the boxes. In particular, Kiselev et al., set the superior limit of the spatial scales equal to the brain size and the inferior limit equal to 3 mm, corresponding reasonably well to the cortical thickness (Kiselev et al., 2003). Also, Goñi et al., choose a range of the box sizes within 5-40% of the smallest Euclidean dimension of the object under examination (Goni et al., 2013). The third strategy is the completely automated selection of both maximum and minimum fractal spatial scales within which the cerebral cortex manifests the highest self-similarity. The last strategy is a mixed approach using an automated selection of the maximum fractal scale only. The existence of a minimum fractal scale reflects the fact that, at increasing the magnification, the effect of increasing detail (as occurs for pure fractals) may vanish because the morphology of the constituent elements, such as, neuronal cells, becomes evident (Landini and Rigaut, 1997). Therefore when the morphology of a biological fractal is investigated under increasing magnification, the 'increasing detail' vanishes at some point in this process, and the geometry of the structural components (cells, membranes, etc) becomes apparent (Landini and Rigaut, 1997). However, it is not conceivable that this effect may be relevant at the typical resolution of high-resolution T1-weighted MRI, i.e., 1 mm, and above. In addition, the goodness of the regression fit is generally very high and thus, the selection of the fractal scaling window on the basis of a goodness of the regression fit index may be sensitive to noise (little changes in the data may produce very small changes (e.g., in the 4 or 5 decimal place of R^2_{adj}), but may drive the selection of the interval of scales. For both reasons, we submit the hypothesis that the minimal fractal scale could be reasonable fixed to the maximum possible resolution, i.e. 1 mm, enabling the automated selection of fractal scaling window to automatically choose the maximum fractal scale only.

To determine which method for the selection of the fractal spatial scales gives better predictions, we used both a Pearson correlation analysis and an age prediction assessment through a machine learning approach based on ElasticNet regression in a nested cross-validation (CV) loop. In particular, we fitted a separate regression model for each FD estimate strategy in order to choose the best predictive model (i.e., the strategy for selection of the interval of fractal spatial scales which gives the most predictive FD estimates).

3.4.2.1 *Methods*

DATASETS

We adopted the scans collected by two public and international datasets.

The first dataset is the "Nathan Kline Institute - Rockland Sample Pediatric Multimodal Imaging Test-Retest Sample" (NKI2) dataset (available at http://fcon_1000.projects.nitrc.org/indi/CoRR/html/nki_2.html).

The second dataset has been collected by the International Consortium for Brain Mapping (ICBM). It belongs to the 1000 Functional Connectomes Project (freely accessible at http://fcon_1000.projects.nitrc.org/), which has been proposed for the purpose of providing the broader imaging community complete access to a large-scale functional imaging dataset.

Demographic information and MRI examinations protocols for both datasets are shown in Table 2.

CEREBRAL CORTEX SEGMENTATION

Each T1-weighted image was pre-processed and segmented using *FreeSurfer* image analysis suite v. 5.3 (see section 3.2 for a detailed description), in order to extract a binary representation of the cerebral cortex for each subject. After the cortical segmentation, the mean cortical thickness of each hemisphere was automatically estimated. The mean value between left and right mean cortical thickness is an estimate of the global mean cortical thickness.

Table 2: Demographic information and MRI examinations protocols

	NKI2	ICBM	Allen Brain Human Atlas
Available at	http://fcon_1000.projects.nitrc.org/indi/CoRR/html/nki_2.html	http://fcon_1000.projects.nitrc.org/	http://human.brain-map.org/mri_viewers/data
Demographic information			
N (M/F)	73 (43/30)	86 (41/45)	7 (5/2)
Age (years)			
mean ± standard deviation (range)	11.8 ± 3.1 (6 - 17)	44.2 ± 17.1 (19 - 85)	41.4 ± 10.9 (24 - 55)
MRI examination			
Field strength	3	3	3
In-plane resolution (mm)	1	1	1
Slice thickness (mm)	1	1	1
Futher details	Nooner et al., 2012	Mazziotta et al., 2001a; Mazziotta et al., 2001b	http://help.brain-map.org/display/humanbrain/Documentation

FRACTAL ANALYSIS

Thus, we have calculated the FD of the cerebral cortex of each subject belonging to the NKI2 and ICBM datasets by using our improved 3D box counting algorithm (see section 3.3) with four different parameters configurations:

1. *Strategy A priori # 1*: *a priori* spatial scales range, as suggested by Kiselev *et al.*, (Kiselev et al., 2003):

   mfs = 3 mm (a typical value of cortical thickness)

   Mfs = 25 cm (head size)

2. *Strategy A priori # 2*: *a priori* spatial scales range, as suggested by Goñi *et al.*, (Goni et al., 2013):

   mfs = 5% of the smallest Euclidean dimension of the object

   Mfs = 40% of the smallest Euclidean dimension of the object

3. *Strategy Automated Min and Max*: a completely automated selection of both the mfs and Mfs;

4. *Strategy Automated Max*: a mixed approach:

   mfs = 1 mm (the side length of a voxel, i.e. the voxel spacing)

   Mfs = automatically selected

STATISTICAL ANALYSIS

We computed the descriptive statistics of the mean cortical thickness and FD values of cerebral cortex for each combination of dataset and method for the selection of the fractal scaling window. In order to assess the potential use of the FD as a neuroimaging marker of brain development and aging, we performed a linear regression analysis and computed the Pearson's correlation coefficient between FD measurements (assessed using both a priori fixed and automated spatial scales range) and age in the NKI2 and in the ICBM datasets. For all tests, a p-value<0.05 was considered statistically significant. The same steps have been followed for the mean cortical thickness.

ELASTIC NET REGRESSION

We fitted a separate regression model for each FD estimate strategy. In particular, we studied the potential of the mean cortical thickness and all fractal descriptors (see Fig. 16) in predicting age using the least-square linear regression with regularization by the combination of L1- and L2-norm (ElasticNet regression method) (Zou and Hastie, 2005). In detail, we determined the fitted regression coefficients β^* by minimizing the residual sum of squares plus two penalty terms proportional to the L1- and L2-norm of the coefficients:

$$\beta^*(\alpha,\rho) = \mathrm{argmin}_\beta\left(\frac{1}{2N}||y - X\beta||_2^2 + \alpha\rho||\beta||_1 + \frac{\alpha(1-\rho)}{2}||\beta||_2^2\right) \quad (16)$$

$$= \mathrm{argmin}_\beta\left(\frac{1}{2N}||y - X\beta||_2^2 + \alpha P_\alpha(\beta)\right) \quad (17)$$

$$P_\alpha(\beta) = \rho||\beta||_1 + \frac{1-\rho}{2}||\beta||_2^2 \quad (18)$$

where α and ρ are positive weighting parameters on the L1 and L2 penalties, X the vector of explanatory variables, $|| \, ||_1$ the L1-norm, $|| \, ||_2$ the L2-norm and N the number of samples (subjects) used for fitting. $P_\alpha(\beta)$ is the elastic-net penalty (Zou and Hastie, 2005) with $0 \leqslant \rho \leqslant 1$. For $\rho = 0$, the penalty is a L2-norm penalty (ridge regression model) and for $\rho = 1$, the penalty is a L1-norm penalty (least absolute shrinkage and selection operator (LASSO) regression model). Elastic-Net regression model combines the power of ridge and LASSO regression into one algorithm. This combination allows for learning a sparse model where few of the weights are non-zero like LASSO, while still maintaining the regularization properties of ridge, such as the shrinking of the coefficients weights according to their importance, without setting the value exactly to zero (Dangeti, 2017). In particular, Elastic-Net is useful when there are multiple features which are correlated with one another.

For each model, in order to reduce the possibility of overfitting and for hyperparameters (α and ρ weights) optimization, the regression task was performed in a nested 10-fold cross-validation (CV) loop

(Mueller and Guido, 2017). In this procedure, for each fold of the outer 10-fold CV, the training set is used for an inner 10-fold CV in order to evaluate the performance of the inner classifier while varying the α and ρ penalty terms in the set $\{0, 0.25, 0.5, 0.75, 1\}$. Once α and ρ values that minimized the out-of-sample prediction error (Hastie et al., 2013) have been found in the inner CV, the model with that α and ρ values is re-trained on the outer training set and tested on the test set kept out from the outer CV. This procedure is repeated for each fold of the outer CV. Before each training of the ElasticNet regression (both in the inner and in the outer CV), each feature was standardized with reference to the training set only. Test set data were not used in any way during the learning process, thus preventing any form of peeking effect (Diciotti et al., 2013). Performance was quantified in terms of the mean absolute error (MAE) between predicted and actual age values computed on the test set of the outer CV

In this study, as a reference model, we modeled age using mean cortical thickness throughout the whole cortex, estimated total intracranial volume (eTIV) and gender values as input features (Tustison et al., 2014). Then, we fitted a separate regression model for each FD estimate strategy in order to choose the best predictive model. Further, we added also the spatial scales automatically determined as input features to assess which strategy for selection of spatial scales produced better predictive FD estimates.

We used own code developed in Python programming language (release 3.7.1, available at https://www.python.org/) for data analysis. In particular, the linear regression model was implemented by using the ElasticNetCV function of the scikit-learn module (version 0.20.1).

3.4.2.2 *Results*

NKI2 DATASET

The different strategies for FD estimation have been applied on the Nathan Kline Institute - Rockland Sample Pediatric Multimodal Imaging Test-Retest Sample dataset (NKI2), composed of MRI scans of 77 young and healthy subjects with age ranging from 6 to 17 years (45 males and 32 females, age 11.7±3.22 years, mean ± standard deviation) (Nooner et al., 2012; Cao et al., 2014). The descriptive statistics of the FD values obtained for each strategy and the association between age and FD estimations are reported in Table 3.

In particular, the Pearson coefficient of correlation between age and FD values was significant ($p<0.001$) only for the two strategies with automated selection of at least one spatial scale. Those significant correlation coefficients were negative (-0.75 and -0.80) meaning that FD (i.e., complexity) reduces when age increases. Among those values, the Automated Max strategy obtained the

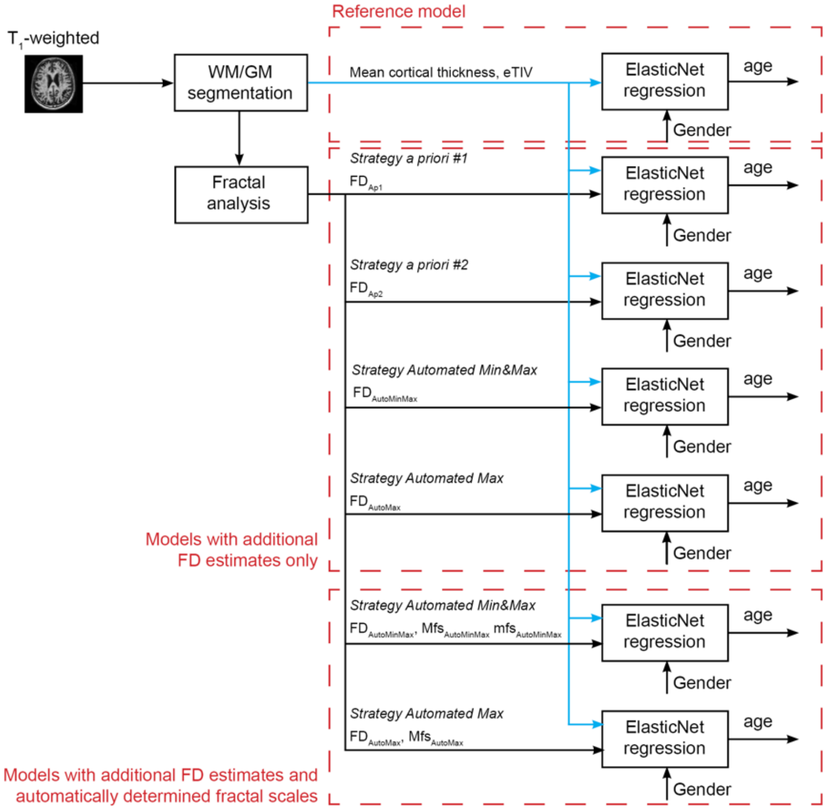

Figure 16: Overview of the feature extraction procedure for individual age prediction through ElasticNet regression, separately, for both NKI2 and ICBM datasets. We fitted a separate regression model for each FD estimate strategy in order to select the best predictive model. In each model, mean cortical thickness, estimated total intracranial volume (eTIV) and gender have been inserted as additional predictors (see the text for other abbreviations).

Table 3: Descriptive statistics (mean ± standard deviation) of the estimated FD values in the NKI2 and ICBM datasets using four different strategies for selection of the interval of spatial scales (see text for details). The Pearson coefficients of correlation (with relative p-value) between FD estimates and age are also reported.

Strategy for selection of fractal scaling window	FD estimates mean $\pm\sigma$	Pearson coefficient of correlation (p-value)
NKI2 dataset		
A priori #1	2.26 ± 0.02	-0.15 (0.20)
A priori #2	2.47 ± 0.07	-0.19 (0.10)
Automated Min&Max	2.57 ± 0.02	-0.75 ($<10^{-13}$)
Automated Max	2.55 ± 0.02	-0.80 ($<10^{-16}$)
ICBM dataset		
A priori #1	2.26 ± 0.02	-0.11 (0.30)
A priori #2	2.46 ± 0.06	-0.09 (0.43)
Automated Min&Max	2.54 ± 0.02	-0.62 ($<10^{-9}$)
Automated Max	2.49 ± 0.02	-0.71 ($<10^{-13}$)

ICBM = International Consortium for Brain Mapping, NKI2 = Nathan Kline Institute - Rockland Sample Pediatric Multimodal Imaging Test-Retest Sample.

correlation coefficient of -0.80, the greatest in absolute value. For this strategy, the scatter plots of age vs. FD values along with regression lines are shown in Fig. 17a. As a reference, the scatter plot of age vs. mean thickness is depicted in Fig. 17b.

The quality of the FD estimations has also been assessed by individual age prediction through a machine learning approach based on an ElasticNet regression. The performance has been measured through the mean absolute error (MAE) between predicted and actual age values. FD substantially reduces MAE (Table 4). Among all models, one for each strategy, the MAE value was lowest for the AutomatedMin and Max strategy (MAE=1.39 years). When automatically determined spatial scales were also added as input features, the lowest MAE value was found for the AutomatedMax strategy (MAE=1.27 years). All MAE values are provided in Table 4.

In order to investigate a comprehensive meaning of the $\text{Mfs}_{\text{AutoMax}}$, we sought a potential association with age. Since $\text{Mfs}_{\text{AutoMax}}$ can assume discrete values only (power of 2), we divided the datasets in age groups of width equal to 4 years (see section 3.4.2.1) and the mean $\text{Mfs}_{\text{AutoMax}}$ has been calculated in each age group. The mean $\text{Mfs}_{\text{AutoMax}}$ was significantly directly associated with age (Pearson coefficient of correlation = 0.96, p=0.0001, Fig. 18).

ICBM DATASET

The different strategies for FD estimation have also been applied on the International Consortium for Brain Mapping (ICBM) dataset. It

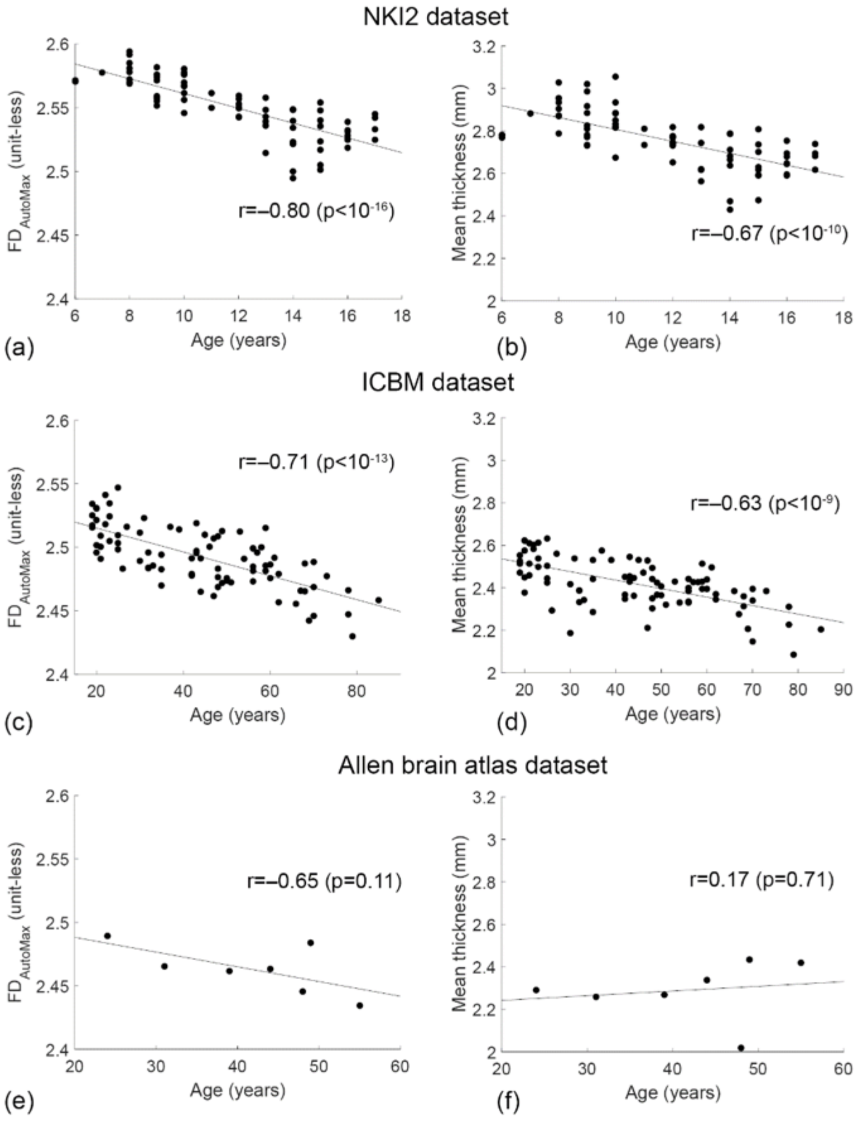

Figure 17: The scatter plots of age vs. FD estimates computed using the Automated Max strategy and age vs. mean thickness in the NKI2 (panes (a) and (b)), ICBM (panes (c) and (d)) and Allen Brain Atlas datasets (panes (e) and (f)) are shown, respectively. In each pane, the regression lines, the Pearson coefficient of correlation r along with the relative p-value are also reported.

Table 4: Individual age prediction assessment in NKI2 and ICBM datasets using different sets of input features: the MAE and the Pearson coefficient of correlation r (with relative p-value) between ElasticNet predicted values of test set of the outer CV and actual values of the nested 10-fold CV are provided. Pearson coefficient of correlation r between ElasticNet predicted values of the test set of the outer CV and actual values.

Features*	MAE (years)	r
NKI2 dataset		
CT	1.76	0.78
CT, FD_{Ap1}	1.56	0.83
CT, FD_{Ap2}	1.77	0.78
CT, $FD_{AutoMinMax}$	1.39	0.88
CT, $FD_{AutoMinMax}$, $Mfs_{AutoMinMax}$, $mfs_{AutoMinMax}$	1.38	0.88
CT, $FD_{AutoMax}$	1.53	0.86
CT, $FD_{AutoMax}$, $Mfs_{AutoMax}$	1.27	0.90
ICBM dataset		
CT	12.1	0.62
CT, FD_{Ap1}	12.1	0.62
CT, FD_{Ap2}	12.2	0.62
CT, $FD_{AutoMinMax}$	11.7	0.64
CT, $FD_{AutoMinMax}$, $Mfs_{AutoMinMax}$, $mfs_{AutoMinMax}$	11.9	0.63
CT, $FD_{AutoMax}$	11.1	0.71
CT, $FD_{AutoMax}$, $Mfs_{AutoMax}$	11.1	0.70

CT = mean cortical thickness, ICBM = International Consortium for Brain Mapping, FD_{Ap1} = fractal dimension computed using the a priori method #1 for selection of spatial scales, FD_{Ap2} = fractal dimension computed using the a priori method #2 for selection of spatial scales, $FD_{AutoMax}$ = fractal dimension computed using automated selection of the maximal spatial scale, $FD_{AutoMinMax}$ = fractal dimension computed using automated selection of both minimal and maximal spatial scales, MAE = mean absolute error, $Mfs_{AutoMax}$ = maximal fractal scale computed using automated selection of the maximal spatial scale, $Mfs_{AutoMinMax}$ = maximal fractal scale computed using automated selection of both minimal and maximal spatial scales, $mfs_{AutoMinMax}$ = minimal fractal scale computed using automated selection of both minimal and maximal spatial scales, NKI2 = Nathan Kline Institute - Rockland Sample Pediatric Multimodal Imaging Test-Retest Sample.

*In all models, estimated intracranial volumes (eTIV) and gender were also included as input features.

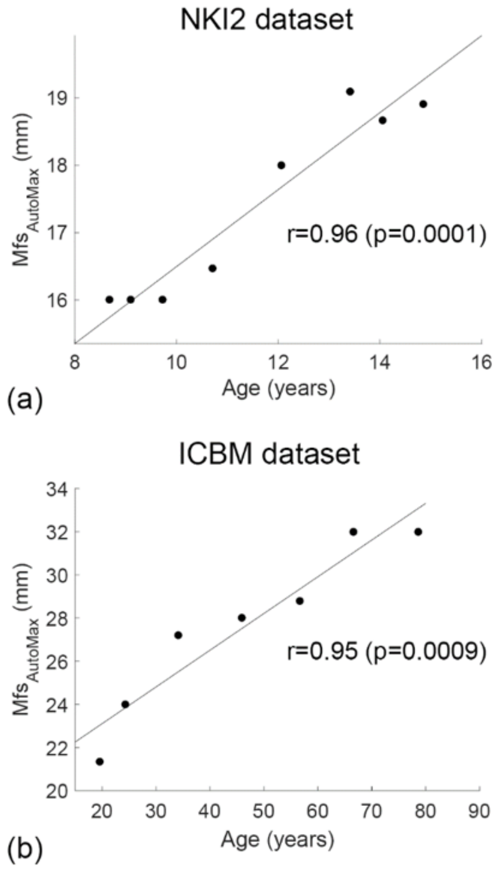

Figure 18: The datasets were divided in age groups of width equal to 5 and 10 years for NKI2 and ICBM datasets, respectively. The scatter plots of mean age vs. mean $\mathrm{Mfs}_{\mathrm{AutoMax}}$ (computed in each age group) in the NKI2 and ICBM datasets are shown in panes (a) and (b), respectively. In each pane, the regression line, the Pearson coefficients of correlation r along with the relative p-value are also reported (see the text for abbreviations).

is composed of MRI examinations of 86 healthy subjects with age ranging from 19 to 85 years (41 males and 45 females, age 44.2±17.1 years, mean±standard deviation). The descriptive statistics of the FD values for each strategy and the association between age and FD estimations are reported in Table 3. In particular, the Pearson coefficient of correlation between age and FD values was significant ($p<0.001$) only for the two strategies with automated selection of at least one spatial scale. Those significant correlation coefficients were negative (-0.62 and -0.71) meaning that FD (i.e., complexity) reduces when age increases. Among those values, the Automated Max strategy obtained the correlation coefficient of -0.71, the greatest in absolute value. For this strategy, the scatter plot of the age vs. FD values along with regression line are shown in Fig. 17c. The same data for age vs. mean thickness data are depicted in Fig. 17d.

The quality of the FD estimations has also been assessed by age prediction through a machine learning. Among all FD estimates, adding FD as predictor, the MAE value was lowest for the AutomatedMax strategy (MAE=11.1 years) and when automatically scales were added as predictors, the same strategy remained the best (MAE=11.1 years). All MAE values are provided in Table 4.

In order to investigate a comprehensive meaning of the $\mathrm{Mfs}_{\mathrm{AutoMax}}$, we sought a potential association with age. Since $\mathrm{Mfs}_{\mathrm{AutoMax}}$ can assume discrete values only (power of 2), we divided the datasets in age groups in decades (see section 3.4.2.1) and the mean $\mathrm{Mfs}_{\mathrm{AutoMax}}$ has been calculated in each age group. The mean $\mathrm{Mfs}_{\mathrm{AutoMax}}$ was significantly directly associated with age (Pearson coefficient of correlation = 0.95, p = 0.0009, Fig. 18).

EX-VIVO MRI OF POST-MORTEM DATA

Potential age-related artifacts in MRI acquisition may influence FD estimations (Reuter et al., 2015; Savalia et al., 2017) especially in older adults for whom head motion is generally greater than in young adults (Andrews-Hanna et al., 2007; Reuter et al., 2015; Pardoe et al., 2016). To this end, we have computed the mean cortical thickness and FD estimations using the AutomatedMax strategy of the cerebral cortex on the Allen Human Brain Atlas (http://human.brain-map.org/mri_viewers/data) (Sunkin et al., 2012). It is composed of post-mortem T1-weighted MRI examinations of 8 healthy subjects with age ranging from 24 to 57 years (6 males and 2 females, age 43.4±11.5 years, mean±standard deviation). One *FreeSurfer* segmentation failed and it was excluded from further analysis. The FD values showed an apparent decreasing trend with age (not statistically significant) (Fig. 17e), while no evident association between mean cortical thickness and age appeared in this small sample (Fig. 17f).

3.4.2.3 *Discussion*

THE AUTOMATED SELECTION OF THE FRACTAL SCALING WINDOW

In this study we compared four different strategies for selection of the fractal scaling window, including two a priori selections (inspired by the works of Kiselev et al., 2003; Goni et al., 2013), an automated selection of both maximum and minimum fractal spatial scales within which the cerebral cortex manifests the highest self-similarity and a mixed approach, using an automated selection of the maximum fractal scale only. We employed two public and international datasets of MRI scans for a total of 163 healthy subjects for the study of brain development and aging. Among all strategies, we showed that, using the mixed approach, we consistently observed the best associations with age and the best machine learning models for individual age prediction in both datasets. Furthermore, the association between age and FD estimates with the mixed approach were consistently greater than that between age and mean thickness. In addition, in both children and adults, the FD shows a significant decrease with age, while the mean $\mathrm{Mfs}_{\mathrm{AutoMax}}$ automatically selected using the mixed approach increases with age. These results may indicate that the GM becomes less morphologically complex with increasing age, but, at the same time, more homogeneous (as the observation scale changes, the observed structure remains unchanged for several consecutive scales).

The possibility to automatically determine the range of spatial scales has allowed to observe that this optimal range may differ among subjects and, in particular, that the mean $\mathrm{Mfs}_{\mathrm{AutoMax}}$ values show an association with age in both datasets. The machine learning approach candidates the FD and automatically determined scales as indices able to describe the structural complexity of the cerebral cortex, and, potentially, to monitor its changes during the brain development and aging.

NKI2 DATASET

The significant negative correlation (-0.80, p-value $<10^{-16}$) we found between age and FD values of the cerebral cortex, in the NKI2 dataset, suggests that the reduction of the structural complexity begins during the first years (from the age of 6-years) of the brain development. So far, a few studies evaluated the possible modifications with age of the FD of the normal brain focusing on children and adolescents (Blanton et al., 2001) or adult or elderly subjects (Madan and Kensinger, 2016). In particular, Blanton *et al.*, evaluated the FD of the pial surface of four regions (inferior and superior frontal lobe, temporal lobe and parieto-occipital lobe) in children of 6-16 years of age and reported an increase in cortical complexity only in frontal lobe regions. They hypothesized that these changes might reflect ongoing processes such as myelination and synaptic remodelling that extends into the second decade of life. In addition, they supposed that the increasing structural complexity of the frontal lobe during the development and adolescence may be referred to the emergence of the executive functions, as planning and abstract reasoning, typical phenomena at this stage of growth (Cole and Cole, 1993; Blanton et al., 2001). Although our results show a significant negative trend of FD values from 6 years of age, they are not at odds with those found by Blanton *et al.*, (Blanton et al., 2001). Firstly, from a methodological point of view, they calculated the FD of the pial surface rather than that of the cerebral cortex, thus analyzing only the structural changes that occur at the surface level, without considering the volume present inside the surface, which could contribute directly to the modifications of the surface shape (King et al., 2009). Moreover, in our work, we computed the FD of the cerebral cortex of the whole-brain rather than separately for each lobe; our value of FD takes into account the phenomena that occur in all lobes, which can manifest a different behavior with age, both from a structural and functional point of view. In the work by Jernigan *et al.*, (Jernigan et al., 1991), e.g., a decrease of the GM volume of the superior cerebral cortex was reported as a feature of normal brain maturation in 39 healthy subjects aged 8-35 years; only the frontal lobe was characterized by several structural changes, which include, at the same time, an increase in the volume of the skull and a decrease in the volume of the GM. A possible explanation is that, in this region concurs a combination of late myelination of WM axons and a local accumulation of CSF (Jernigan et al., 1991). In this situation, the pial surface of the frontal lobe may increase its structural complexity with age (Blanton et al., 2001), while the entire cerebral cortex may show a global FD decreasing with age. Our results are consistent with some predominantly cross-sectional MRI studies that addressed modifications over time of the volume of the cerebral cortex in normal individuals covering a wide range of ages (Caviness et al., 1996; Pfefferbaum et al., 1994; Reiss et al., 1996). Accordingly, in a study of 85 children aged 5-17 years (Reiss et al., 1996), the ratio of cortical GM volume to total cerebral volume showed a significant negative correlation with age. This was explained because of the regressive processes needed to refine the connection between neurons through cellular and synaptic pruning during the childhood (Cowan et al., 1984). In another work, the cortical GM volume was modelled with a cubic function and suggested a peak around age 4 years and a decrease thereafter in 88 subjects aged 3 months-30 years with normal MRI (Pfefferbaum et al., 1994). In a study of 30 children aged 7-11 years (Caviness et al., 1996), it has been found that the GM volume does not show significant changes in the strict range of 7-11 years and that it has already reached the 95% of the GM volume of an adult brain, whereas the WM volume is only 85% of the adult WM volume. For this reason, the authors supposed that the relative rate of volume increase of GM structures prior to age 7 years has been significantly greater than that of WM and beyond this stage of transition it is a stabilisation in the total volume of GM. In this "second" phase, when the late myelination process takes the place of the gyrification, the structural complexity of the cerebral cortex may start to decrease. Possible explanations of the decreased volume of the cerebral cortex since 5 years of age include regressive phenomena, such as cell death, synaptic and axonal pruning, and atrophic processes (Pfefferbaum et al., 1994). In particular pruning implies the normal elimination of about 40% of cortical synapses during childhood (Huttenlocher, 1979).

ICBM DATASET

In this work, the reduction of the structural complexity has been shown also during healthy aging with a significant negative correlation (r=-0.71; p-value $< 10^{-13}$) between age and FD of the cerebral cortex. Only a few previous studies have evaluated structural complexity changes in normal aging brain, using different implementations of the fractal analysis. Also, Madan *et al.*, (Madan and Kensinger, 2016), utilizing a sample of 427 individuals (20-80 years old) from a freely available dataset, observed a negative correlation between cerebral cortex FD and age (r = -0.732, p <0.001). In this latter study, FD was more sensitive to age-related differences than other metrics of cortical complexity such as cortical thickness or gyrification. On the contrary, the FD of the cerebral cortex, which is related to both cortical thickness and to the folding properties of the cortex, summarizes in a unique number a quantitative description of the structural complexity in the cerebral cortex, and might be better able to detect age-related changes with respect to standard morphometric methods. Post mortem (Raz and Rodrigue, 2006; Kemper, 1994; Skullerud, 1985) and in-vivo MRI studies (Courchesne et al., 2000; Good et al., 2001; Lemaître et al., 2005; Smith et al., 2007) have consistently shown an age-related decrease in GM and WM volume associated with an enlargement of the CSF spaces. Cortical reductions involve the entire cerebral cortex (Driscoll et al., 2009; Fjell et al., 2014), not being confined to specific regions, with annual change rates of around 0.2–0.5% in most regions (Fjell et al., 2014; Scahill et al., 2003; Fotenos et al., 2005; Hedman et al., 2012). Also, several studies have identified prefrontal cortices as especially prone to the effects of aging (Madan and Kensinger, 2016; Fjell et al., 2009; Hogstrom et al., 2013; Hutton et al., 2009; Salat et al., 2004; Peng et al., 2016), but have provided conflicting results concerning other regional differences in age-vulnerability, for example with respect to the involvement of primary cortices (Raz and Rodrigue, 2006; Good et al., 2001; Lemaître et al., 2005; Smith et al., 2007; Salat et al., 2004; Bakkour et al., 2013; Jernigan et al., 2001; Raz et al., 1997). Previous morphometric MR studies on normal aging have utilized both volumetric techniques, such as ROI (Jernigan et al., 2001; Raz et al., 1997) and voxel-based morphometry (VBM) analysis (Good et al., 2001; Smith et al., 2007), or surface-based measures, such as cortical thickness (Fjell et al., 2009; Salat et al., 2004), surface area (Dickerson et al., 2009), and gyrification measures (Rettmann et al., 2006).

Interestingly, postmortem studies have found that aging is mainly associated to loss of neuropil and nerve fibers, with a reduction of dendrites, spines density and synapses, and all these changes are expected to alter brain fractal properties. On the contrary, the direct loss of neurons is relatively limited in healthy aging (Pakkenberg et al., 2003; Peters et al., 1998; Jacobs et al., 1997). As reported by previous literature, anatomical structures which present fractal properties, may show a loss of structural complexity (Goldberger et al., 2002a), and this makes the structures poor in information content (Goldberger, 1997) and reduces the individual ability to adapt to the environment (Goldberger et al., 2002b).

Our results using post-mortem data are in agreement with ones found by Madan *et al.*, (Madan and Kensinger, 2016): the FD values showed a decreasing trend with age (not statistically significant), while no association between mean cortical thickness and age appeared in this small sample.

3.4.3 *The structural complexity of the cortical GM at ultra-high field MRI*

In this section, we aim at analyzing the fractal properties of cerebral GM in datasets acquired at various magneto-static field strengths (1.5T, 3T and 7T), using the proposed algorithm with the automated selection of the fractal scaling window (section 3.1). It is worth noting that, the fractal analysis has not been applied on images acquired at ultra-high field, i.e. 7T, yet. In particular, we aimed at computing the FD of the cortical GM using T1-weighted images through the automated selection of spatial scales in which the GM manifests the highest self-similarity in order to 1) assess if the minimal fractal scale (mfs) in which GM manifests self-similarity depends on the image resolution using 1.5T, 3T and 7T data and 2) evaluate if the higher spatial resolution at ultra-high magnetic field allows to capture a higher level of structural complexity, in terms of FD, of the cortical GM.

3.4.3.1 *Methods*

PARTICIPANTS

For the *dataset A*, we adopted the scans collected in the public and international dataset "Multi-Modal MRI Reproducibility Resource" (MMRR), accessible via the Neuroimaging Informatics Tools and Resources Clearinghouse (NITRC, http://www.nitrc.org/projects/multimodal). This dataset, named "Kirby-21", contains MRI scans-rescans of 21 healthy volunteers with age ranging from 22 to 61 years (11 men and 10 women, aged 31.8±9.5 years, mean ± standard deviation) (Landman et al., 2011). Imaging modalities include T1-weighted, fluid attenuation inversion recovery (FLAIR), diffusion tensor imaging (DTI), resting state functional magnetic resonance imaging (fMRI), B0 and B1 field maps, arterial spin labeling (ASL), vascular space occupancy (VASO), quantitative T1 mapping, quantitative T2 mapping, and magnetization transfer imaging on the same 3T scanner (Philips Achieva).

The *dataset A* contains two subjects of the "Kirby-21" dataset (men, aged 22 and 24 years), which were acquired also on a 7T scanner. Thus, we selected these two subjects, who were examined both at 3T and 7T; T1-weighted MR images were employed only. The images were acquired with a high resolution 3D sequence [Magnetization Prepared Rapid Gradient Echo, MPRAGE (3T) and Turbo Field Echo TFE (7T)], with isotropic resolution of 1 mm for the 3T scanner and of 0.7 mm for the 7T scanner.

In the *dataset B*, we adopted 20 out of the 24 healthy control subjects [14 men and 6 women, mean age± standard deviation (range), 26.4 ± 2.1 (22.0 - 29.2) years] (Pantoni et al., 2019), with the purpose of age- (p=0.19 at ANOVA test) and gender- (p=0.36 at χ^2 test) matching with *datasets C* and *D* (see below).
All subjects were examined on a clinical 1.5 T system (Intera, Philips Medical System, Best, The Netherlands) equipped with 33 mT/m maximum gradient strength and a 6-channel head coil. After the scout image, sagittal 3D T1-weighted turbo gradient echo [repetition time (TR)=8.1 ms, echo time (TE)=3.7 ms, flip angle=8°, inversion time=764 ms, field of view (FOV)=256 mm × 256 mm, matrix size=256×256, 160 contiguous slices, slice thickness=1 mm] images were acquired.

The *dataset C* is a subset of the "kirby-21" dataset, acquired at 3T (see detailed description in *dataset A* and Landman et al., 2011). In order to match age and gender of the datasets *B* (see above) and *D* (see below), we used data from 14 subjects [8 men and 6 women, mean age± standard deviation (range), 26.6 ± 2.6 (22.0 - 30.0) years].

In the last dataset, the *dataset D*, we adopted some of the T1-weighted scans of healthy subjects belonging to the Consortium for Reliability and Reproducibility (CoRR) and acquired on a 7T MR scanner (Gorgolewski et al., 2014). This dataset contains 22 participants (10 women), selected from a database of people having previously taken part in 7 T experiments (from 5 to 51 times, mean 23) at the Max Planck Institute for Human Brain and Cognitive Sciences (Leipzig, Germany) and were therefore accustomed with the procedure. All subjects had given written informed consent and the study was approved by the Ethics Committee of the University of Leipzig. All experiments were performed on a 7 T whole-body MR scanner (MAGNETOM 7 T, Siemens Healthcare, Erlangen, Germany). A combined birdcage transmit and 24 channel phased array receive coil (NOVA Medical Inc, Wilmington MA, USA) was used for imaging. For structural imaging, a 3D MP2RAGE (Marques et al., 2010) sequence was used: 3D-acquisition with field of view 224 mm × 224 mm × 168 mm (H-F; A-P; R-L), imaging matrix 320 × 320 × 240, 0.7 mm^3 isotropic voxel size, Time of Repetition (TR)=5.0 s, Time of Echo (TE)=2.45 ms, Time of Inversion (TI) 1/2 =0.9 s/2.75 s, Flip Angle (FLA) 1/2 =5°/3°, Bandwidth (BW)=250 Hz/Px, Partial Fourier 6/8, and GRAPPA acceleration with iPAT factor of 2 (24 reference lines). To match age and gender with the datasets *B* and *C*, as shown above, we used data from 17 subjects [8 men and 9 women, mean age± standard deviation (range), 25.2 ± 2.4 (22.0 - 30.0) years].

A summary of the main characteristics of each dataset is shown in table 5.

Table 5: Demographic data of the four datasets explored. No significant differences between datasets *A*, *B* and *C* for age (pvalue = 0.19 at ANOVA test) and gender (pvalue = 0.36 at χ^2 test).

	Magnetostatic field strength	Isotropic in-plane resolution	Number of subjects (M/F)	Age (years) mean (range)
Dataset A	3T and 7T	1 mm and 0.7 mm	2 (2/0)	23 (22 - 24)
Dataset B	1.5T	1 mm	20 (14/6)	26.4 (22 – 29.2)
Dataset C	3T	1mm	14 (8/6)	26.6 (22 - 30)
Dataset D	7T	0.7 mm	17 (8/9)	25.2 (22 - 30)

GM/WM SEGMENTATION

Completely automated cortical reconstruction and volumetric segmentation of each subject's structural T1-weighted MRI scan was performed by employing the *FreeSurfer* image analysis suite v. 6.0, which is documented and freely available (http://surfer.nmr.mgh.harvard.edu/). The technical details of these procedures are described in prior publications (Dale et al., 1999; Dale and Sereno, 1993; Fischl and Dale, 2000; Fischl et al., 2001; Fischl et al., 2002; Fischl et al., 2004a; Fischl et al., 1999a; Fischl et al., 1999b; Fischl et al., 2004b; Han et al., 2006; Jovicich et al., 2006; Segonne et al., 2004; Reuter et al., 2010; Reuter et al., 2012). The stable version 6.0 introduced some improvements useful for a correct segmentation and surface reconstruction of MR images acquired on a 7T scanner. Firstly, the possibility to run the pipeline (recon-all) for data with voxel size less than 1 mm. Secondly, since the procedure would be very time-consuming, many routines were OpenMP-parallelized, in order to compute at the same time as many steps as possible, according to the features of the available hardware (http://surfer.nmr.mgh.harvard.edu/fswiki/ReleaseNotes).

For each dataset, all the scans acquired at 1.5 T and 3T were processed in their native resolution of 1 mm (called "1.5T_1mm" and "3T_1mm" data), while the images collected at 7T were segmented both at the resampled resolution of 1 mm ("7T_1mm" data) and at their original resolution equal to 0.7 mm ("7T_0.7mm" data).

After the end of the automated procedures, all the segmentations and surfaces reconstructions were visually inspected for defects and the correction methods proposed by *FreeSurfer* developers were applied (http://surfer.nmr.mgh.harvard.edu/fswiki/FsTutorial/TroubleshootingData). The correction procedures consist of editing of brain mask and WM (especially for the scans acquired at 7T) and adding control points and re-running of the *FreeSurfer* pipeline.

In this study, we analyzed the cerebral cortical GM segmentation only.

FRACTAL ANALYSIS

The mfs and FD of cerebral cortical GM have been measured by the improved 3D box counting algorithm with the automated selection of the fractal scaling window, as described in sections 3.1 and 3.3.

STATISTICAL ANALYSIS

The *dataset A* was used within the pilot study "The fractal dimension of the brain at ultra-high field MRI", presented at the sixth national congress of Bioengineering (GNB) (Marzi and Diciotti, 2018). Since the sample is composed of only 2 subjects, no statistical analysis was carried out. The *datasets B*, *C* and *D* were chosen to confirm the results of the previous preliminary study (Marzi and Diciotti, 2018).

Differences between datasets for the automatically selected mfs and FD values were evaluated through a non-parametric Kruskal-Wallis Analysis of Variance (ANOVA), with a significance threshold of 0.05.

In addition, differences between *datasets C* and *D* for the automatically selected mfs and FD values were evaluated through a Mann-Whitney test for unpaired data (3T_1mm vs. 7T_0.7mm data and 3T_1mm vs. 7T_1mm data) and a Wilcoxon matched pairs test for paired data (7T_0.7mm vs. 7T_1mm data). In order to control the family wise error rate of the Mann Whitney test, the Bonferroni correction for multiple comparisons was applied with a significance threshold of 0.05. These results were presented at the 25th international conference of the Human Brain Mapping Organization (Marzi and Diciotti, 2019).

EXPERIMENTAL TESTS

In the "Kirby-21" dataset, the *FreeSurfer* outputs for the images acquired on a 3T scanner are available online (http://www.mindboggle.info/data). Notwithstanding, because the segmentation outputs may vary according to the workstation and the software release (Gronenschild et al., 2012), we performed all the computations on the same platform and with the same version of *FreeSurfer* software. The workstation was a Dell PowerEdge T620 equipped with two 8-core Intel Xeon E5-2640 v2, for a total of 32 CPU threads, and 128 GB RAM, using the Oracle Grid Engine batch-queuing system. The *FreeSurfer* segmentation and reconstruction procedure required ~ 10 hours (with additional ~ 5 hours after manual correction) for 1.5 T and 3T images and 7T scans resampled at 1 mm of resolution, while 7T scans at native resolution needed ~ 35 hours (with additional ~ 17 hours after manual errors correction). The computation time of the FD was ~ 1 minute.

3.4.3.2 *Results and discussion*

DATASET A

In Table 6, the automatically selected mfs is shown, for each subject, magnetic field intensity and in-plane resolution.

These preliminary results figure out that the cerebral GM manifests fractal properties also at spatial scales less than 1 mm.

In Table 7, we reported the values of FD for each subject, magnetic field intensity and in-plane resolution.

The FD values of the cerebral GM acquired at 7T are higher than those computed at 3T. Interestingly, the FD values of the cerebral GM acquired at 7T resampled at 1 mm are within the FD observed at 3T and at 7T at their native resolution. The resampling procedure at lower resolution causes the loss of some details, which may lead to an intermediate level of observed structural complexity.

Table 6: Minimal fractal scale automatically selected of the cerebral GM in 3T and 7T acquisitions.

	3T (1 mm)	7T (1 mm)	7T (0.7 mm)
Cerebral GM of sub. #1	1	1	0.7
Cerebral GM of sub. #2	1	1	0.7

Table 7: FD of the cerebral GM in 3T and 7T acquisitions.

	3T (1 mm)	7T (1 mm)	7T (0.7 mm)
Cerebral GM of sub. #1	2.50	2.51	2.58
Cerebral GM of sub. #2	2.49	2.52	2.59

DATASETS B, C AND D

The results of the Kruskal-Wallis ANOVA confirmed the preliminary study results (Marzi and Diciotti, 2018) (Table 8).

Table 8: Minimal fractal scale automatically selected and FD of the cerebral GM in 1.5T, 3T and 7T acquisitions.

	1.5T_1mm data median (range)	3T_1mm data median (range)	7T_1mm data median (range)
mfs (mm)	2.0 (2.0 – 2.0)	2.0 (2.0 – 2.0)	1.4 (0.7 – 1.4)
FD (-)	2.59 (2.49 – 2.55)	2.54 (2.50 – 2.57)	2.59 (2.54 – 2.61)

The mfs values, automatically chosen by the algorithm, and the respective FD values are significantly different in the three datasets (p-value < 0.05).

In addition, in the preliminary study (Marzi and Diciotti, 2019), the mfs automatically selected in 7T_0.7mm data [1.4 (0.7-1.4) mm, median (range) mm] was significantly lower than that in 1-mm voxel size data [2.0 (2.0-2.0) mm, for both 3T_1mm and 7T_1mm data], and, in particular, assumed the value of 0.7 mm for 3 subjects.

The FD measured in 7T 0.7mm data [2.59 (2.54 - 2.61)] was significantly higher than that measured at 1-mm voxel size [2.54 (2.50 - 2.56) and 2.55 (2.49 - 2.55), for 3T_1mm and 7T_1mm data, respectively]. The corrected p-values were $< 10^{-3}$. No significant differences in mfs and FD was found between 3T_1mm and 7T_1mm data.

For the first time, the morphological complexity of the cerebral cortical GM, acquired at ultra-high field MR, has been analyzed by fractal analysis.

The higher spatial resolution at 7T enhances the sensitivity of the images to subtle changes in shape with an increase of the observed complexity of the cerebral GM, measured by FD, and a decrease in the mfs automatically selected. We suppose that cerebral cortical GM has fractal properties even at scales lower than those currently visible in MR images, acquired on clinical scanners.

4

THE FRACTAL ANALYSIS IN NEUROLOGICAL DISEASES

This chapter describes the results of fractal analysis in three neurological diseases: spinocerebellar ataxia of type 2 (SCA2), small vessels disease (SVD) and cerebral amyloid angiopathy (CAA). The study of patients with CAA was made possible thanks to the collaboration with the Stroke Research Center, Massachusetts General Hospital, Department of Neurology at Harvard Medical School in Boston, where I spent three months since October 2017 until January 2018.

4.1 THE MORPHOLOGICAL COMPLEXITY OF THE BRAIN IN PATIENTS WITH SCA2

SCA2 dataset

Spinocerebellar ataxia type 2 (SCA2) is the second more frequent SCA after SCA3 worldwide. At neuropathological examination, it is associated with a pattern of pontocerebellar degeneration with variable damage of the cerebral hemispheres (Auburger, 2012; Durr et al., 1995; Estrada et al., 1999). Accordingly, MRI shows volume loss in the brainstem, cerebellar peduncles, and both cerebellar GM and WM (Mascalchi and Vella, 2012). Volume loss in the cerebral cortex and cerebral WM of SCA2 patients is inconsistently reported and less prominent (Brenneis et al., 2003; D'Agata et al., 2011; Della Nave et al., 2008a; Della Nave et al., 2008b; Giuffrida et al., 1999; Goel et al., 2011; Mercadillo et al., 2014).

The fractal geometry has been found to be able to characterize GM and WM alterations in neurodegenarative diseases (for more details see section 2.3).

In multisystem atrophy cerebellar type and in SCA3, two conditions sharing with SCA2 a pattern of pontocerebellar degeneration at neuropathological examination (Estrada et al., 1999), it was shown that the cerebellar FD, especially in the WM, was lower in patients than in controls (Wu et al., 2010; Huang et al., 2017). Therefore, FD could have the potential to represent a useful tool in detecting subtle brain changes as well as in tracking the progression of neurodegeneration.

So far, fractal analysis has not been applied neither to SCA2 nor to investigate possible cerebral and longitudinal changes in pontocerebellar degenerations. Finally, data are not available on the capability of fractal analysis to track progression of changes in structural complexity associated to sporadic or inherited pontocerebellar degenerations. This is particularly important due to the need of imaging biomarkers for progressive ataxias (Baldarcara et al., 2015).

The aims of this SCA2 study were: (1) to investigate whether FD is able to demonstrate differences in the structural complexity of GM and WM of cerebellum or cerebrum between patients and healthy controls; and (2) to evaluate whether FD can monitor the progression of the damage over time.

4.1.1 *Materials and methods*

Participants

Nine patients (3 women, 6 men; mean age 48.7 ± 12.9 years) with genetically determined SCA2 gave their informed consent to participate in this study that was approved by the Local Ethics Committee. The cut-off number of triplet repeats expansions qualifying for diagnosis of SCA2 was 34 CAG on one allele, and the mean number of abnormal triplets was 40.6 ± 1.4 (Pareyson et al., 1999). All patients underwent MRI twice on the same scanner and with the same acquisition protocol, on average 3.6 ± .7 years apart (range, 2.2-4.0 years). At the time of both MRI examinations, the patients underwent evaluation by the same neurologist, who computed the duration of symptoms and signs and scored the neurological deficit using the Inherited Ataxia Clinical Rating Scale (IACRS) (Filla et al., 1990) and the International Cooperative Ataxia Rating Scale (ICARS) (Trouillas et al., 1997). IACRS semiquantitatively assesses using a 0–38 score scale (with 38 corresponding to maximum deficit) signs and symptoms related to ataxia as well as pyramidal tract dysfunction and impaired vibration or position sense, which are frequently observed in SCA2. ICARS semiquantitatively assesses only cerebellar functions using a 0–100 score scale (with 100 corresponding to maximum deficit). Demographic information and clinical evaluation of SCA2 patients at baseline and follow-up are reported in Table 9.

For the present investigation, we recruited as controls 16 age- and gender-matched healthy subjects (7 women, 9 men; mean age 50.3 ± 18.8 years) with no familiar or personal history of neurologic or psychiatric dysfunction and a normal neurological examination and who gave written consent to participate. They underwent MRI twice using the same scanner and acquisition protocol, on average 3.3 ± 1.0 years apart (range, 1.9-4.7 years) (Table 9).

Table 9: Demographic information and clinical evaluation of the SCA2 dataset. Mean ± standard deviation (range) values are reported.

	SCA2 patients		Healthy controls	
	Baseline	Follow-up	Baseline	Follow-up
Demographic information				
N (M/F)	9 (6/3)	9 (6/3)	16 (9/7)	16 (9/7)
Age (years)	48.7 ± 13.1 (28.4 - 67.4)	52.1 ± 13.2 (31.6 - 71.3)	49.8 ± 19.0 (25.1 - 72.4)	53.1 ± 18.1 (29.3 - 74.5)
Clinical evaluation				
Disease duration (years)	12.8 ± 7.3 (2 - 23)	-	-	-
IACRS	17.2 ± 4.3 (9 - 25)	21.3 ± 6.1 (14 - 31)	-	-
ICARS	39.7 ± 14.3 (15 - 54)	44.3 ± 14.5 (19 - 62)	-	-

MRI Examination

The details about MRI examinations of all patients and controls are showed in Table 10.

T1-weighted images were visually evaluated by a neuroradiologist for the identification of artifacts before entering further image processing. After this visual quality check, all images were retained for further processing.

Table 10: MRI examination of SCA2 dataset. The same scanner and protocol acquisition has been used for patients and healthy controls, both at baseline and follow-up.

MRI scanner	Philips Intera Best, The Netherlands
Magneto-static field strength	1.5 T
Maximum gradient strength	33 mT/m
Head coil channels	6
TR / TE / TI (ms)	8.1 / 3.7 / 764
FLA (°)	8
FOV	256 mm x 256 mm
Matrix size	256 x 256
Slice thickness	1 mm

Cerebral and Cerebellar Segmentation and Quality Control

The processing pipeline for the T1-weighted image of a single subject is schematized in Fig. 19.

Completely automated cortical reconstruction and segmentation of the WM of each subject's structural T1-weighted MRI scan were performed using the *FreeSurfer* image analysis suite v. 5.3 (http://surfer.nmr.mgh.harvard.edu/) (Fischl, 2012). Since the gross neuropathological appearance of SCA2 is a pontocerebellar atrophy

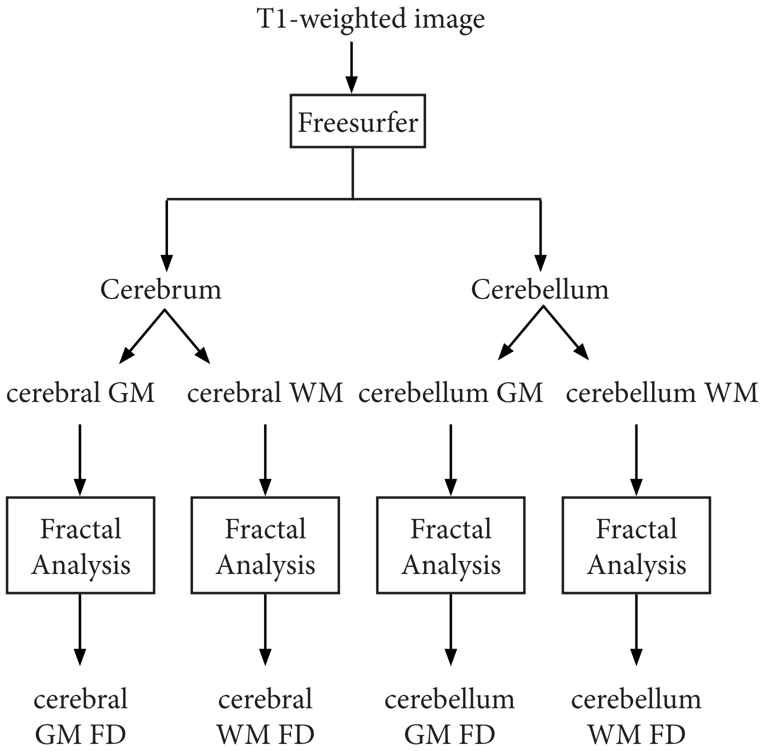

Figure 19: Processing pipeline for the T1-weighted image of a single subject (Marzi et al., 2018a).

with prominent loss of bulk in the cerebellum, (Mascalchi and Vella, 2012; Della Nave et al., 2008b), automated segmentation of each subject's cerebellum was also performed using the *FreeSurfer* suite.

Cortical reconstruction and GM/WM surfaces were manually inspected for defects; the correction techniques suggested by *FreeSurfer* developers, including editing of brain mask and WM and adding control points and rerunning of the *FreeSurfer* pipeline (https://surfer.nmr.mgh.harvard.edu/fswiki/FsTutorial/TroubleshootingData) were applied up to two times to assure that all defects were corrected. All views (coronal, sagittal, and axial) were used to confirm segmentation and surfaces reconstruction errors. Cerebellum segmentations were manually edited using a free-hand pencil using the Freeview utility, part of *FreeSurfer* suite.

In this work, we investigated the FD of the cerebral cortical GM (cerebral GM), of the cerebral WM and of the cerebellar GM and cerebellar WM. An example of these segmentations for a representative SCA2 patient is shown in Fig. 20.

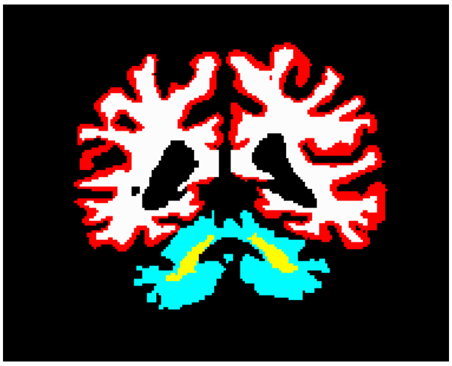

Figure 20: A coronal slice of the cortical gray matter segmentation of cerebrum (red) and cerebellum (cyan) and white matter of cerebrum (white) and cerebellum (yellow) in one patient with spinocerebellar ataxia type 2 (Marzi et al., 2018a).

Fractal Analysis

In order to compute the FD, we used the improved 3D box counting algorithm with the automated selection of the fractal scaling window (see chapter 3).

All computations have been performed on a Dell PowerEdge T620 workstation equipped with two 8-core Intel Xeon E5-2640 v2, for a total of 32 CPU threads, and 128 GB RAM, using the Oracle Grid Engine batch-queuing system. For each subject, the processing time required approximately 9 hours of CPU time for *FreeSurfer* segmentation process and about 1 minute for each FD computation.

Statistical Analysis

Differences between groups (SCA2 patients vs. healthy subjects) for FD values were evaluated at baseline through a Mann-Whitney test. For each FD value, the rate of change (defined as the ratio between the modification over time and time to- follow-up) was computed and differences between groups evaluated through a Mann-Whitney test. For each test, the Holm-Bonferroni correction (to control the family-wise error rate) for multiple comparisons was applied with a significance threshold of .05.

Due to the paucity of the patient sample, correlation of FD with genetic and clinical features was not performed.

4.1.2 *Results*

The descriptive statistics of FD of cerebellar and cerebral GM and WM are reported in Table 11. At baseline, FD values of cerebellar GM and WM were significantly ($P < .001$) lower in SCA2 patients than in controls. Also, FD values of cerebral GM were significantly ($P < 0.05$) lower in SCA2 patients than in controls, whereas the FD values of cerebral WM were not significantly different. No significant differences in rate of change of FD values between controls and SCA2 patients were found.

Table 11: Descriptive statistics of FD values at baseline and rate of change for healthy controls and SCA2 patients expressed as mean (standard deviation).

	Baseline (unitless)			Rate of change (unitless/year)		
	Controls	SCA2 patients	Uncorrected p-value	Controls	SCA2 patients	Uncorrected p-value
Cerebral GM	2.43 (0.02)	2.39 (0.03)	0.002 *	0.00 (0.00)	0.00 (0.01)	0.80
Cerebral WM	2.51 (0.03)	2.52 (0.02)	0.59	0.00 (0.01)	-0.01 (0.01)	0.03
Cerebellum GM	2.56 (0.02)	2.48 (0.04)	0.00007 **	0.00 (0.01)	0.00 (0.01)	0.76
Cerebellum WM	2.22 (0.19)	1.74 (0.09)	0.0002 **	-0.01 (0.08)	0.04 (0.09)	0.98

* $p < 0.05$ at Mann-Whitney test after Holm-Bonferroni correction (to control the family wise error rate) for multiple comparisons.

** $p < 0.001$ at Mann-Whitney test after Holm-Bonferroni correction (to control the family wise error rate) for multiple comparisons.

4.1.3 *Discussion*

SCA2 shares with other SCAs and multisystem atrophy cerebellar type a pattern of pontocerebellar atrophy at neuropathology and MRI examination (Mascalchi and Vella, 2012). In particular, the microscopic examination consistently shows in SCA2 widespread neuronal loss in the cerebellar cortex and pontine nuclei, the midbrain, and medulla (Auburger, 2012; Seidel et al., 2012), and extensive WM damage with loss of myelinated fibers and gliosis affecting the transverse pontine fibers, central cerebellum, and the cerebellar folia, the middle and inferior cerebellar peduncles, medial lemniscus, and trigeminal tracts, the fasciculus gracilis and cuneatus and the spinocerebellar tracts (Auburger, 2012; Seidel et al., 2012).

On the contrary, neuropathological studies have provided heterogeneous evidence of cerebral cortical or subcortical damage in SCA2 (Durr et al., 1995; Estrada et al., 1999).

In the present investigation, we used FD to explore the structural complexity of the cortical GM and WM of both the cerebellum and cerebrum in symptomatic SCA2 patients. Our baseline data demonstrated reduced complexity of the cerebellar cortex and WM in SCA2 that is in line with data obtained in other types of pontocerebellar degeneration (Wu et al., 2010; Huang et al., 2017). Two are the novel findings revealed by our study. First, at baseline, also cerebral cortical GM but not the cerebral WM shows reduced complexity in symptomatic SCA2 patients. Second, the longitudinal assessment failed to reveal significant differences of the rate of FD changes in the cerebellar and cerebral cortical GM and WM between SCA2 patients and healthy age-matched controls.

The loss of neurons and subsequent axonal degeneration observed in neurodegenerative conditions leads to cerebral atrophy that implies thinning of the cortical ribbon and widening of sulci (decreased folding area) (Wu et al., 2010; Thompson et al., 2007). When FD of the cortical ribbon, rather than that of the pial surface, is considered, as we did, these two effects are complementary in lowering the FD (King et al., 2010). Fractal geometry techniques may represent a useful tool with the potential to provide further information as respect to conventional morphometry techniques, such as voxel-based morphometry, which are based on volume measurement. As a matter of fact, one MRI study using visual assessment reported some degrees of cerebral atrophy in 12 of 20 symptomatic SCA2 patients (Giuffrida et al., 1999) and some voxel-based morphometry studies in SCA2 patients have reported decreased volume of the cerebral cortex in the frontal, temporal, insular, or parietal lobes (Brenneis et al., 2003; D'Agata et al., 2011; Della Nave et al., 2008b; Goel et al., 2011; Mercadillo et al., 2014), but the localization of the clusters of atrophy varied considerably from one to another study and one voxel-based morphometry study failed to reveal changes of the cerebral cortex volume (Della Nave et al., 2008a).

The use of a sophisticated quantitative neuroimaging technique of fractal analysis can outperform the nude eye (at neuropathological or MRI examination) in detecting subtle cerebral cortical changes in SCA2. Moreover, it could be valuable for studying the increasingly observed cognitive changes, even before onset of ataxia, in SCA2

(Olivito et al., 2017; Schmitz-Hubsch et al., 2008; Velazquez-Perez et al., 2014).

In our study, at baseline, we observed markedly decreased complexity of the cerebellar WM in SCA2 patients, whereas the complexity of the cerebral WM was not significantly different between patients and controls. These results are in line with the neuropathological data indicating a severe cerebellar WM damage, but inconsistent cerebral WM atrophy and gliosis in SCA2 (Estrada et al., 1999), and with MRI data showing decreased cerebellar WM volume in all visual and voxel-based morphometry studies (Brenneis et al., 2003; D'Agata et al., 2011; Della Nave et al., 2008b; Giuffrida et al., 1999; Goel et al., 2011; Mercadillo et al., 2014), but loss of cerebral WM volume in a few voxel-based morphometry studies (Brenneis et al., 2003; Della Nave et al., 2008b). The volume loss and simplified tissue architecture associated with axonal loss and demyelination observed at the neuropathological examination in the cerebellar WM can likely explain the decreased FD in the cerebellum of SCA2 patients.

Furthermore, to the best of our knowledge, so far, only two studies evaluated the progression of brain damage in SCA2 patients. Notably, both studies were performed in the same population of patients and controls of the present study. In the first study (Mascalchi et al., 2014), utilizing tensor-based morphometry, significant higher atrophy rates were found in the midbrain and cerebellum in patients with SCA2 with respect to controls, while no differences in WM or GM volume loss were observed in the supratentorial compartment. In the second study (Mascalchi et al., 2015), tract-based spatial statistics revealed that longitudinal axial diffusivity changes were greater in SCA2 patients than in controls in the right cerebral hemisphere and corpus callosum, while longitudinal mode of anisotropy changes were lower in SCA2 patients than in controls in many WM tracts (in brainstem, cerebellum, and cerebral hemisphere). In our study, fractal analysis failed to demonstrate a higher or lower rate of FD changes in SCA2 as compared to controls. This preliminary finding is likely to reflect the small sample size. However, the findings of the above-mentioned previous studies could suggest a relative low sensitivity of fractal analysis of GM and WM in T1-weighted images in tracking the progression of structural complexity in SCA2, albeit further studies are necessary to confirm this hypothesis.

We recognize the following limitations of our study.

First, due to the small sample size, which limits the statistical power, we did not perform correlation analysis between genetic and clinical features and FD values. Also, the small number of included patients hindered the possibility of performing analyses with a large number of variables, e.g., including brain volumes of the cerebral and cerebellar GM and WM, due to an inevitable and relevant loss of statistical power (i.e., the probability of obtaining a statistically significance outcome if the true effect is not zero), whatever adjustment for multiple comparison we use (Lazzeroni and Ray, 2012). In our opinion, since fractal analysis is based on processing of standard volumetric T1-weighted images that are usually obtained in clinical studies of patients with ataxia, both correlation analyses and joint analysis of FD values and brain volumes could be performed in the context of multicenter projects such as the ENIGMA-ataxia (enigma@ini.usc.edu), that is based on data pooling from qualified centers worldwide.

Second, we did not obtain cognitive assessment in our patients. Since SCA2 patients can show subtle but characteristic cognitive deficits (Olivito et al., 2017; Schmitz-Hubsch et al., 2008; Velazquez-Perez et al., 2014) which have been attributed to diffuse damage of the WM of the cerebellum and superior and middle cerebellar peduncles resulting in a cerebello-cerebral dysregulation (Olivito et al., 2017), inclusion of cognitive evaluation in future neuroimaging studies of SCA2 is recommended.

Third, in order to localize the alterations of the structural complexity of the cerebral GM, a regional analysis (e.g., studying brain lobes) of FD could be of great interest.

In conclusion, our longitudinal study indicates that the FD of cerebellar cortical GM and WM as well as of the cerebral cortex is reduced in SCA2 patients as compared to healthy controls. In our small sample, analysis of FD failed to demonstrate progression of changes in structural complexity in SCA2 over time.

4.2 THE MORPHOLOGICAL COMPLEXITY OF THE BRAIN IN PATIENTS WITH SVD

VMCI-Tuscany dataset

Mild cognitive impairment (MCI) defines a clinical status in which cognitive deficits are present but their severity, although clinically recognizable, does not impact on the personal autonomy in activities of daily living, and thus does not reach the level of dementia. Various dementia subtypes are preceded by an MCI stage (Gauthier et al., 2006). Small vessel disease (SVD) is recognized as a major cause of stroke and dementia (Rensma et al., 2018), and has been shown to be frequently associated with a cognitive impairment mainly characterized by deficits of attention and executive function (O'Brien et al., 2003; Pantoni, 2010). Neuroimaging plays today a crucial role in defining the presence of SVD in patients with cognitive decline in whom it may be the sole pathological process or coexist with degenerative processes (Pantoni, 2010). Efforts have been made to harmonize the neuroimaging definition of macroscopic lesions underlying SVD on conventional MRI, including recent small subcortical infarcts, white matter hyperintensities (WMH), lacunes, enlarged perivascular spaces (EPVS), cerebral microbleeds, and atrophy (De Guio et al., 2016; Wardlaw et al., 2013). A consensus paper reporting neuroimaging standards for research in SVD also recognized the importance of new MRI techniques to evaluate the different expressions of SVD (Wardlaw et al., 2013). However, it remains unclear, at present, which are the neuroimaging features that better predict clinical features, particularly cognitive status. Additionally, both subcortical and cortical changes are today accepted as features of SVD, but their respective role in terms of clinical correlates is not yet established. Also, the evaluation of different SVD features in a single patient is not easy and rather demanding in terms of time and use of MRI techniques.

During the last 20 years, quantitative assessment of brain volume using isotropic high-resolution T1-weighted MR images has been largely applied to evaluate macroscopic structural alterations occurring in both aging and neurological diseases (Toga and Thompson, 2002). However, volume assessment does not capture the inherent structural complexity of the cerebral WM and the cortical GM. This complexity may be investigated using fractal geometry, which describes the complexity of self-similar objects (see chapter 2 for more details). The FD of cerebral WM and cortical GM can be computed using high-resolution T1-weighted images commonly employed in SVD and therefore does not require additional MRI acquisitions. The WM and GM FD values have been found positively associated with cognitive performance in aged subjects (Mustafa et al., 2012) and the GM FD also with the Alzheimer's Disease Assessment Scale-Cognitive (ADAS-cog) scale in Alzheimer's disease patients (King et al., 2010) (see section 2.2 for further details). Along this line, it is reasonable to assume that the WM FD and GM FD, as measurements of the structural complexity of the brain, might represent a potentially useful feature also in SVD.

The aims of this study were to assess whether the FD of cerebral WM and/or of cortical GM computed using high-resolution isotropic T1-weighted MR images are valuable predictors of cognitive performance in patients with SVD and MCI, and if they are complementary to other standard neuroimaging features and to WM and GM volumes. We employed a machine learning strategy based on LASSO (least absolute shrinkage and selection operator) regression applied on several neuroimaging features in a nested cross-validation loop. This approach was aimed at 1) choosing the best predictive models, able to reliably predict the individual neuropsychological scores sensitive to attention and executive dysfunctions (prominent features of subcortical vascular cognitive impairment) and 2) identifying a features ranking according to their importance in the model through the assessment of the out-of-sample error, that is a measure of how accurately a model is able to predict values for unseen data.

4.2.1 *Materials and methods*

Participants

In this study, we included 76 patients with evidence of MCI and WM T2-weighted imaging hyperintensities of presumed vascular origin of moderate or severe extension who were enrolled in one (Florence) of the VMCI-Tuscany study centers and who were object of a previous report (Pasi et al., 2015). Twelve patients were excluded because *FreeSurfer* segmentations were not satisfactory after manual editing and re-running up to three times (see section 4.2.1 below). Final analyses were thus performed on 64 patients. The mean ± standard deviation (SD) age and years of education were 74.6 ± 6.9 and 7.9 ± 4.2 years, respectively; 34 patients (53%) were males.

A control group composed of 24 healthy control subjects (12 men and 12 women, mean age ± standard deviation, 72.5 ± 4.7 years) was included in the study. No significant difference in age (t-test, p=0.07) and in sex proportion (chi-square test, p=0.97) was present between the patient and control groups. Healthy controls had no familial or personal history of neurologic or psychiatric disorders, and underwent a neurologic examination that showed no abnormalities. Patients and controls underwent the same imaging protocol on the same scanner, but evaluation of some standard neuroimaging features of SVD (i.e., cerebral microbleeds, enlarged perivascular spaces, and quantitative WM lesion load) was available only for the patient sample as part of the Vascular MCI-Tuscany Study protocol.

Vascular MCI-Tuscany Study neuropsychological evaluation

The Vascular MCI-Tuscany Study is a 3-center, prospective, observational study aimed at evaluating the determinants of the transition from vascular MCI to dementia in patients with SVD. The study methodology has been reported in details elsewhere (Poggesi et al., 2012). The study was conducted in accordance with the Helsinki Declaration and was approved by the local Ethics Committee. Each patient gave a written informed consent.

According to the study protocol, at baseline, each patient underwent a comprehensive neuropsychological evaluation by means of the VMCI-Tuscany neuropsychological battery, that is an extensive tool specifically developed for patients with SVD and MCI (Salvadori et al., 2015). The VMCI-Tuscany neuropsychological battery includes both global cognitive functioning tests and second-level tests covering different cognitive domains. For the purpose of this study, among the cognitive tests of the VMCI-Tuscany neuropsychological battery, we selected those which are sensitive to attention and executive dysfunctions, because these are prominent features of subcortical vascular cognitive impairment (O'Brien et al., 2003). The cognitive tests selected were:

- *Montreal Cognitive Assessment (MoCA)*, a 10-minute cognitive screening tool (Conti et al., 2015; Nasreddine et al., 2005). Total score range is 0-30; higher scores represent better performance;
- *Visual Search*, for focused attention. The score range is 0-50; higher scores represent better performance;
- *Symbol Digit Modalities Test (SDMT)*, for sustained attention. The score range is 0-110; higher scores represent better performance;
- *Trail Making Test (TMT), Part A*, for psychomotor speed. The score is the time in seconds required to complete the test; higher scores represent worse performance;
- *Color Word Stroop Test*, for selective attention and response inhibition. The score is evaluated by means of execution time in seconds; higher scores represent worse performance;
- *Immediate copy of the Rey-Osterrieth Complex Figure (ROCF)*; involves planning and organizational strategies that are related to executive functions (Caffarra et al., 2002a; Elderkin-Thompson et al., 2004; Freeman et al., 2000; Salvadori et al., 2018; Shin et al., 2006). The score range is 0-36 ; higher scores represent better performance.

For the neuropsychological tests, we used the available normative data that are based on healthy Italian adult samples national norms to calculate demographically-adjusted scores by means of the regression equations extracted by normative studies (Caffarra et al., 2002a; Caffarra et al., 2002b; Conti et al., 2015; Della Sala et al., 1992; Giovagnoli et al., 1996; Nocentini et al., 2006). Since age and level of education resulted significantly associated with the performance in all the selected cognitive tests, a factor of correction was applied. For the visual search test, also sex was found to be a statistically significant factor, and the corresponding correction was then calculated and applied (Nocentini et al., 2006).

MRI examination

All subjects were examined on a clinical 1.5 T system (Intera, Philips Medical System, Best, The Netherlands) equipped with 33 mT/m maximum gradient strength and a 6-channel head coil. The details about the MRI examinations protocol are reported in Table 12.

All images were visually assessed by an experienced neuroradiologist in order to identify possible artifacts. After this visual quality control, all images were used for further processing.

Table 12: MRI examination protocol for VMCI-Tuscany dataset.

	Sagittal 3D T1-weighted turbo gradient echo	Axial T2-weighted FLAIR	Axial T2*-weighted gradient-echo
TR / TE / TI (ms)	8.1 / 3.7 / 764	11000 / 140 / 2800	696 / 23
FLA	8	90	18
FOV	256 mm x 256 mm	250 mm x 250 mm	250 mm x 200 mm
Matrix size	256 x 256	280 x 202	252 x 160
Number of slices	160	40	22
Slice thickness	1 mm	3 mm	5 mm
Interslice gap	0 mm	0.6 mm	1 mm
NEX	1	1	2

Neuroimaging features extraction

A general overview of the neuroimaging feature extraction procedure is shown in Fig. 21.

STANDARD NEUROIMAGING FEATURES OF SMALL VESSEL DISEASE

For the purposes of the present study, we decided to focus on the main MRI SVD-related markers, i.e., white matter hyperintensities, lacunes, enlarged perivascular spaces, and cerebral microbleeds, that were evaluated according to the conventional and quantitative MRI methods applied within the Vascular MCI-Tuscany Study. While lacunes, EPVS and cerebral microbleeds have been conventionally evaluated according to standard visual rating approaches centrally performed by an experienced neurologist, the WMH have been quantitatively expressed as the lesion load.

Lacunar infarcts were defined as cavities 3 to 10 mm in diameter mostly ovoid/spheroid, and were categorized as 0 = (absent), 1 = (1-3), 3 = (>3).

Microbleeds were defined as small, rounded or circular, well-defined hypointense lesions within brain tissue ranging from 2 to 10 mm in diameter; the Microbleed Anatomical Rating Scale (MARS) was used to assess the total number of microbleeds (Gregoire et al., 2009).

Enlarged perivascular spaces were defined as small, sharply delineated structures of cerebrospinal fluid intensity on imaging that followed the orientation of the perforating vessels, ran perpendicular to the brain surface, and were < 3 mm wide. EPVS have been assessed in the basal ganglia and centrum semiovale, and were

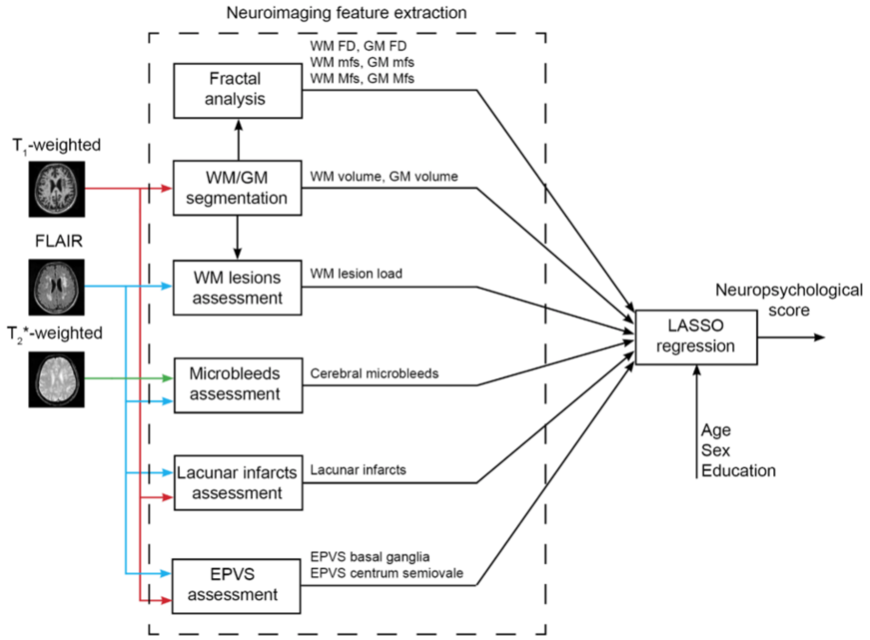

Figure 21: Overview of the neuroimaging feature extraction procedure for LASSO (least absolute shrinkage and selection operator) regression. We fitted a separate regression model for each neuropsychological test. WM and GM volumes are normalized to the estimated intracranial volume (EPVS = enlarged perivascular spaces, FD = fractal dimension, FLAIR = Fluid-attenuated inversion recovery, GM = gray matter, Mfs = maximum fractal scale, mfs = minimum fractal scale, WM = white matter). Demographic variables (age, sex and level of education) have been inserted as additional predictors to model possible residual effects in the patient population (Pantoni et al., 2019).

coded as 0=(absent), 1 = ($\leqslant$ 10), 2 = (11-20), 3 = (21-40), and 4 = ($\geqslant$ 40). A single observer outlined the T2-hyperintense WM lesions on FLAIR images of all patients with SVD and MCI using a semiautomated segmentation technique based on user-supervised local thresholding (Jim 5.0, Xinapse System, Leicester, UK; www.xinapse.com/Manual/). We thus defined the WM lesion load as the total lesions volume normalized by the individual cerebral WM volume.

WHITE AND GREY MATTERS VOLUMES

Cortical reconstruction and volumetric segmentation was performed with the *FreeSurfer* image analysis suite v. 5.3, which is documented and freely available (http://surfer.nmr.mgh.harvard.edu/). The technical details of these procedures are described in prior publications (Fischl, 2012). All the *FreeSurfer* outputs were visually inspected for defects: all planes (coronal, sagittal and axial) were examined to evaluate segmentation and surfaces reconstruction errors. The manual editing of a single operator and re-running was carried out up to three times to assure that all defects were corrected (McCarthy et al., 2015).

Volumes of cerebral WM, cortical GM and estimated intracranial volume (eTIV) were also computed. To reduce the effect of brain size, both WM and GM volumes were normalized to eTIV.

WHITE AND GREY MATTERS FRACTAL ANALYSIS

We computed the FD of both the cerebral WM and cortical GM, with the improved 3D box-counting algorithm with the automated selection of the fractal scaling window, presented in the chapter 3. In this study, both the minimum fractal scale (mfs) and the maximum fractal scale (Mfs) of WM and cortical GM have been also considered as potential predictors of cognitive scores. An example of a WM and a cortical GM segmentation mask in one patient with SVD and MCI is shown in Fig. 22.

Descriptive statistics and between-group analysis

Descriptive analyses were carried out to characterize the sample in terms of socio-demographic, cognitive scores and neuroimaging features. We also compared WM and GM volumes, fractal dimensions and minimum and maximum scales between healthy controls and patients using a Mann Whitney test corrected for multiple comparisons with the Holm-Bonferroni procedure (to control the family-wise error rate) using a corrected significance p-value < 0.05.

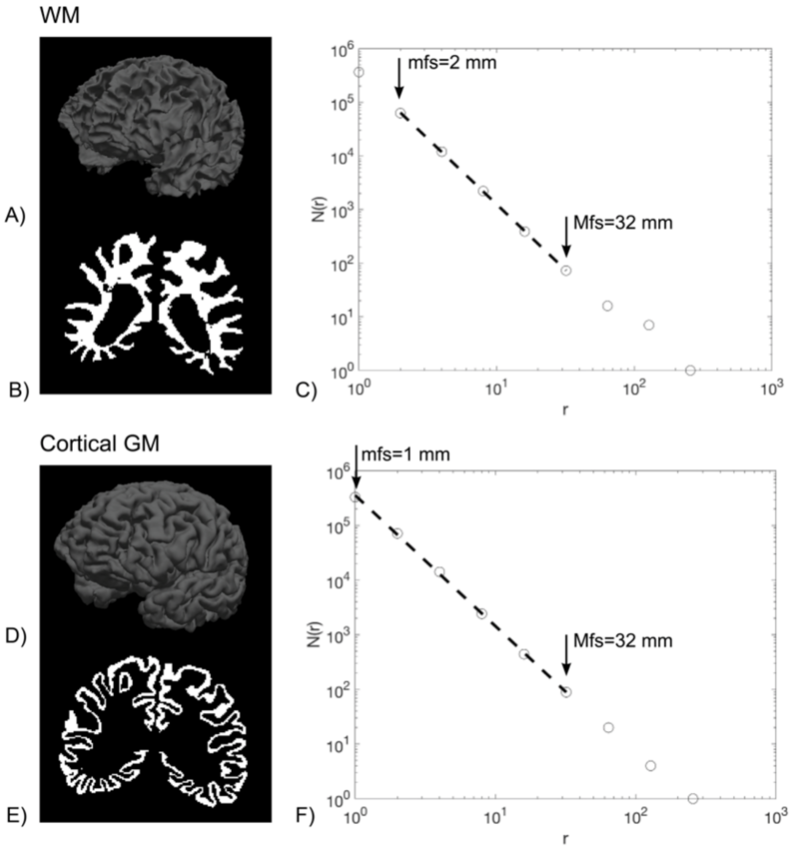

Figure 22: Example of a WM and a cortical GM segmentation mask in one patient with SVD and MCI. A) A 3D view of the GM/WM interface surface; B) A coronal slice of the WM volume mask; C) The log-log plot of N(r) counts vs. cube side r (mm) is shown for the cerebral WM volume mask. The regression line, which showed the highest R2adj (0.9999) and a sign changed slope (i.e., FD) equal to 2.4530, is also superimposed. The WM mfs was $2^1 = 2$ mm and the WM Mfs was $2^5 = 32$ mm; D) A 3D view of the pial surface; E) A coronal slice of the GM volume mask; F) The log-log plot of N(r) counts vs. cube side r (mm) is shown for the cortical GM volume mask. The regression line, which showed the highest R2adj (0.9996) and a sign changed slope (i.e., FD) equal to 2.4429, is also superimposed. The GM mfs was $2^0 = 1$ mm and the GM Mfs was $2^5 = 32$ mm (Pantoni et al., 2019).

LASSO regression

We fitted a separate regression model for each neuropsychological test. In particular, we studied the potential of all neuroimaging features (see Fig. 21) in predicting cognitive adjusted scores using the least-square linear regression with regularization by the L1-norm (LASSO regression method) (Hastie et al., 2013). In detail, we determined the fitted regression coefficients β by minimizing the residual sum of squares plus a penalty term proportional to the L1-norm of the coefficients:

$$\beta(\alpha) = \mathrm{argmin}_{\beta}\left(\frac{1}{2N}||y - X\beta||_2^2 + \alpha||\beta||_1\right) \tag{19}$$

where α is a positive weighting parameter on the L1 penalty, X the vector of explanatory variables (neuroimaging and demographic features),$||\ ||_1$ the L1-norm, $||\ ||_2$ the L2-norm and N the number of samples (patients) used for fitting. The α penalty weights the degree of sparsity, so that higher values of α enforce sparsity in the regression coefficients, i.e., drive more coefficients in the model to be exactly zero. In this way, the regression fit and feature selection are carried out at the same time.

For each model, in order to reduce the possibility of overfitting and for hyperparameter (α weight) optimization, the regression task was performed in a nested 10-fold cross-validation (CV) loop (Mueller and Guido, 2017). In this procedure, for each fold of the outer 10-fold CV, the training set is used for an inner 10-fold CV in order to evaluate the performance of the inner classifier while varying the α penalty term in the set $\{h \times 10^p, 1\}$, where h={1, 2, . . . , 9} and p={-4, -3, -2, -1}. Once α value that minimized the out-of-sample prediction error (Hastie et al., 2013) has been found in the inner CV, the model with that α value is re-trained on the outer training set and tested on the test set kept out from the outer CV. This procedure is repeated for each fold of the outer CV. Before each training of the LASSO regression (both in the inner and in the outer CV), each feature was standardized with reference to the training set only. Test set data were not used in any way during the learning process, thus preventing any form of peeking effect (Diciotti et al., 2013). Performance was quantified in terms of the Pearson correlation coefficient between predicted and actual values of the neuropsychological test computed on the test set of the outer CV.

Since the selected features may vary depending on how the data are split in each fold of the CV, for each neuropsychological test, we repeated the nested CV procedure 1,000 times recording the frequency that each feature was selected and the sign of the regression coefficient estimates from each fold of the round of the outer CV. In fact, the frequency of selection of a feature indicates to what extent that feature is more likely to be included in the model and the 1,000 repetitions allow investigating a robust statistical association between neuropsychological scores and features. Average and standard deviation of the results from all repetitions (correlation coefficients r between real and predicted labels in the test set of the outer CV) were computed to get a final model assessment score.

For each neuropsychological test, statistical significance of prediction performance was determined via permutation analysis – recommended especially when the sample size is small (Noirhomme et al., 2014). Thus, for each neuropsychological test, 5,000 new models were created using a random permutation of the labels (i.e., neuropsychological scores), such that the explanatory variables were dissociated from its corresponding neuropsychological score, to simulate the null distribution of the performance measure against which the observed value was tested (Nichols and Holmes, 2002). Correlations were considered significant if the p-value computed using permutation tests was < 0.05.

We used own code developed in Python programming language (release 3.7.1, available at https://www.python.org/) for data analysis. In particular, the linear regression model was implemented by using the LassoCV function of the scikit-learn module (version 0.20.1).

Experimental tests

The computational analyses performed for the extraction of advanced neuroimaging features were carried out on a Dell PowerEdge T620 workstation equipped with two 8-core Intel Xeon E5-2640 v2, for a total of 32 CPU threads, and 128 GB RAM, using the Oracle Grid Engine batch-queuing system. For each subject, the processing time required approximately 30 minutes for the quantification of WM lesions volume, 9 hours of a single core CPU time (with additional about 5 hours after each manual editing) for *FreeSurfer* segmentation, and about 2 minutes for the calculation of both WM FD and GM FD. The total computation time for the 1,000 nested CV loop and 5,000 random permutations for all neuropsychological tests was about 3 hours on a single core of a Linux workstation equipped with a 4-core (8 threads) INTEL i7-7700K CPU and 64 GB RAM.

4.2.2 *Results*

Descriptive statistics and between-group analysis

Distributions of the neuropsychological tests mean and SD adjusted scores, and percentages of patients with an abnormal performance in each test are shown in Table 13. Four patients did not complete the TMT-A and one the immediate copy of the ROCF.

Descriptive statistics of neuroimaging features and available comparisons between healthy subjects and patients with SVD and MCI have been reported in Table 14. As compared to healthy controls, the group of patients with SVD and MCI showed significantly reduced WM FD and GM normalized cortical volume and increased mfs of GM.

Table 13: Distributions of the neuropsychological tests adjusted scores and of percentages of patients with an abnormal performance.

Neuropsychological test	Number of patients	Patients with an abnormal performance (%)	Mean (standard,deviation)	Min, max
Montreal cognitive assessment	64	28 (44%)	20.6 (4.5)	11.95, 29.29
Visual search	64	27 (42%)	31.8 (8.5)	14.35, 0.17
Symbol digit modalities test	64	27 (42%)	36.9 (9.6)	22.02, 59.04
Color word stroop test	64	30 (47%)	38.5 (28.7)	-3.45, 155.09
Trail making test - part A	60	25 (39%)	62.3 (46.4)	3.77, 202.2
Rey–osterrieth complex figure (immediate copy)	63	49 (78%)	22.9 (8.3)	4, 36

Table 14: Descriptive statistics of neuroimaging features [mean (SD), minimum and maximum values], and comparisons between healthy subjects and patients with SVD and MCI.

		Feature	Healthy subjects (N = 24)	Patients with SVD and MCI (N = 64)[b]	P-value (corrected)
Standard features	Visual rating	Lacunar infarcts (categorical)[c]	0	2.09 (0.81) [1–3]	NA
		Microbleeds (number)	-	1.27 (3.71) [0–18]	NA
		EPVS basal ganglia (categorical)°	-	1.72 (0.77) [0–4]	NA
		EPVS centrum semiovale (categorical)°	-	1.77 (0.77) [1–3]	NA
	Quantitative	WM lesion load (unitless)	-	0.07 (0.05) [0.01–0.20]	NA
Volumes		GM volume (unitless)	0.24 (0.02) [0.21–0.28]	0.23 (0.02) [0.20–0.27]	0.002 (0.015)[a]
		WM volume (unitless)	0.30 (0.02) [0.25–0.32]	0.29 (0.02) [0.24–0.34]	0.040 (0.161)
Fractal analysis		GM FD (unitless)	2.4407 (0.0203) [2.4010–2.4819]	2.4359 (0.0167) [2.3969–2.4746]	0.097 (0.120)
		GM mfs (mm)	1.83 (0.64) [1–4]	2.13 (0.50) [2–4]	7×10^{-4} (0.006)[a]
		GM Mfs (mm)	31.3 (3.27) [16–32]	31.5 (2.81) [16–32]	0.412 (0.412)
		WM FD (unitless)	2.4874 (0.0311) [2.4135–2.5297]	2.4650 (0.0341) [2.3960–2.5316]	0.002 (0.015)[a]
		WM mfs (mm)	1.67 (0.48) [1–2]	1.48 (0.50) [1–2]	0.070 (0.120)
		WM Mfs (mm)	16.67 (3.27) [16–32]	20.25 (7.12) [16–32]	0.011 (0.054)

EPVS=enlarged perivascular spaces, FD=fractal dimension, GM=gray matter, Mfs=maximum fractal scale, mfs=minimum fractal scale, N=number of participants, NA=not applicable, SD=standard deviation, WM=white matter. WM and GM volumes are normalized to the estimated intracranial volume.

[a] Significant at a Mann Whitney test corrected for multiple comparison with the Holm-Bonferroni procedure (to control the family-wise error rate) using a corrected significance p-value<.05.

[b] Except for microbleeds, where N=63.

[c] 0=(absent), 1=(1–3), 3=(> 3).° 0=(absent), 1=($\leqslant$10), 2=(11–20), 3=(21–40), 4=($\geqslant$40). - = not measured.

LASSO regression

In Table 15, the results obtained for all LASSO regression models are displayed. We found that the statistically significant models were those for MoCA (r=0.321, p-value=0.039), SDMT (r=0.324, p-value=0.039) and TMT-A (r=0.354, p-value=0.025). Significant prediction above-chance of these scores was obtained using different sets of neuroimaging features. A ranking of all neuroimaging features according to the LASSO feature selection frequency is shown in Fig. 23. The average frequency, among significant models (MoCA, SDMT and TMT-A scores), with which each feature was selected (regression coefficient different from zero) across all outer CV folds in 1,000 repetitions of LASSO regression is shown in Fig. 24. The WM FD was the most frequent feature consistently selected in the significant models.

Table 15: Mean and standard deviation of the Pearson coefficient of correlation r between the LASSO predicted values of the test set of the outer CV and the actual values using 1000 repetitions of the nested 10-fold CV. P-values indicate the probability that the empirical r score could arise by chance. They have been computed using 5000 permuted-data CV scores simulating the null distribution.

Neuropsychological test	Mean r (SD)	p-value
MoCA	0.321 (0.079)	0.039
Visual search	0.106 (0.091)	0.318
SDMT	0.324 (0.073)	0.039
TMT-A	0.354 (0.094)	0.025
Stroop	0.222 (0.082)	0.106
ROC-F immediate copy	0.295 (0.090)	0.090

MoCA, montreal cognitive assessment; ROC-F, Rey–Osterrieth complex figure; SD, standard deviation; SDMT, symbol digit modalities test; TMT-A, trail making test - part A. Significant at the permutation-test using a significant p-value<.05.

Finally, Table 16 shows the neuroimaging features selected with frequency >80% based on 1,000 repetitions of the nested CV along with the direction (positive/negative) of the most frequent sign of the corresponding regression coefficient. The WM FD was the only feature consistently selected in all three models.

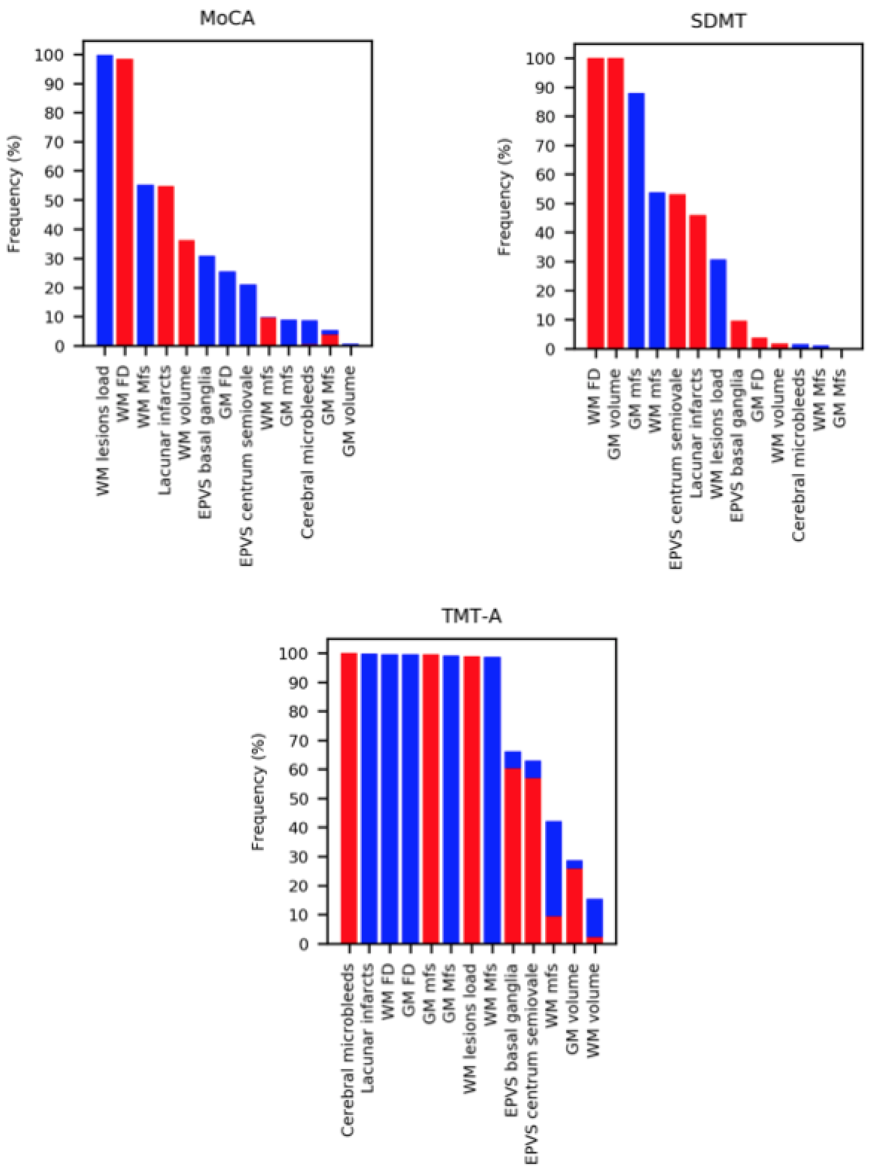

Figure 23: Ranking of LASSO-based neuroimaging feature selection. For each significant model, the frequency with which each feature was selected (coefficient different from zero) across all outer CV folds in 1,000 repetitions of LASSO regression is shown. The features have been reordered based on the occurring average frequencies. Red bars indicate the frequency with which the corresponding coefficient was positive (direct association with the neuropsychological scores) – whereas blue bars, the frequency with which the corresponding coefficient was negative (inverse association with the neuropsychological scores) (Pantoni et al., 2019).

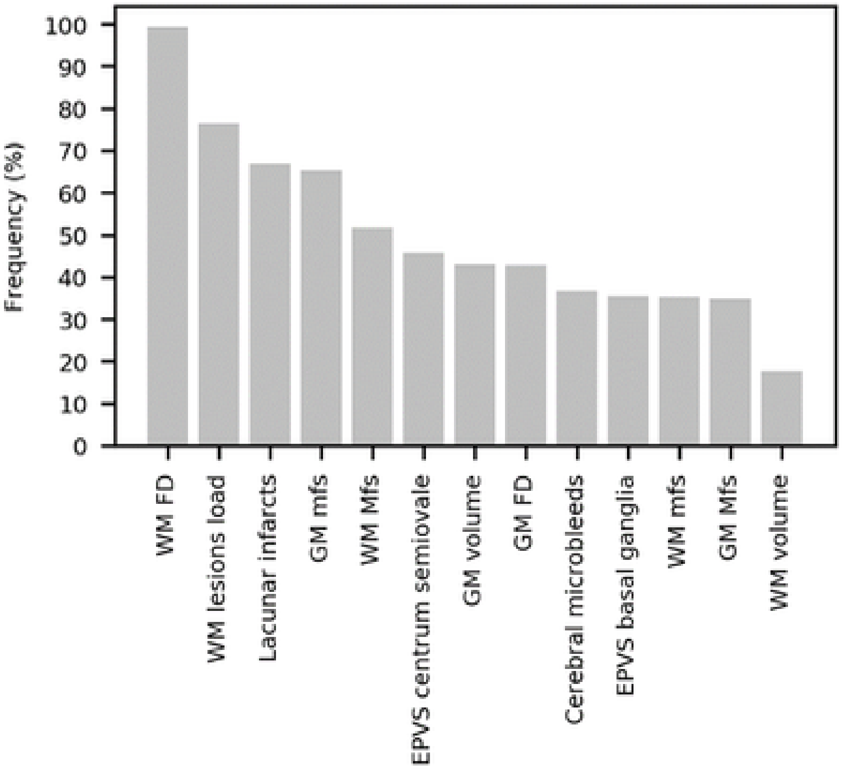

Figure 24: The average frequency among MoCA, SDMT and TMT-A tests with which each neuroimaging feature was selected (coefficient different from zero) across all outer CV folds in 1,000 repetitions of LASSO regression among MoCA, SDMT and TMT-A tests is shown (Pantoni et al., 2019).

Table 16: Neuroimaging features selected with frequency > 80% based on 1000 repetitions of the nested cross-validation along with the direction (positive/negative) of the most frequent sign of the regression coefficient have been reported. For each neuropsychological test, the score interpretation has been also indicated.

Neuropsychological test	Cognitive scores interpretation (worst to best performance)	Relevant features
MoCA	Low to high values	WM FD (+), WM lesions load (-)
SDMT	Low to high values	WM FD (+), GM volume (+), GM mfs (-)
TMT-A	High to low values	Cerebral microbleeds (+), Lacunar infarcts (-), WM FD (-) GM FD (-), GM mfs (+), GM Mfs (-), WM lesions load (+), WM Mfs (-)

MoCA, montreal cognitive assessment; SDMT, symbol digit modalities test; TMT-A, trail making test - part A. (+): a positive direction of the regression coefficient sign indicating a direct association. (-): a negative direction of the regression coefficient sign indicating an inverse association.

4.2.3 *Discussion*

Potentials of WM FD in predicting cognitive performance in patients with SVD and MCI

In this study of patients with SVD and MCI, we used the capability of machine learning in predicting neuropsychological scores on tests sensitive to attention and executive dysfunctions. We found that WM FD was, on average, the feature most consistently selected for predicting neuropsychological scores among the statistically significant models. The WM FD was significantly reduced in patients with SVD and MCI as compared to healthy controls. Also, among the significantly predicted scores, we observed that the trend of the relationship between the WM FD and cognitive performance is univocal. Accordingly, a decrease in WM FD, i.e., a reduction of structural complexity of WM, was associated with a worsening in cognitive performance. It is conceivable that cognitive impairment observed in patients with subcortical WM damage associated with SVD derives from the effect of a diffuse cortical-subcortical disconnection syndrome rather than from a localized mere tissue loss. Of note, in our study, the WM volume was a negligibly selected feature - the latest in feature ranking. We submit the hypothesis that FD represents a marker of global disarrangement of the WM in SVD patients. These pieces of evidence are in line with a previous study in healthy subjects in which individuals with reduced WM FD had lower intelligence scores and more age-related cognitive decline (Mustafa et al., 2012).

As compared to healthy controls, the group of patients with SVD and MCI also showed a significantly higher mfs of the cortical GM, automatically determined by the fractal analysis. Consistently, in the patient group, the GM mfs increased when cognitive performance was worsened. A recent study analyzed the minimum and maximum spatial scales in healthy subjects (Krohn et al., 2019). Although ours and Krohn *et al.*, studies differ for some methodological and pre-processing differences, we observed a similar preference of the automatic selection of the fractal scaling window for smaller minimal scales and shorter interval lengths (number of data points employed in the selected scale range). Indeed, in the patient sample, the most frequent combinations were, for WM, mfs=1 mm and interval length=5 data points and mfs=2 mm and interval lenght=4 data points, while, for GM, mfs=2 mm and interval length=5 data points. However, further studies are needed to investigate the impact of each disease condition on the spatial scales. In our patient sample, we hypothesize that the behavior of the GM mfs might reflect an initial disruption of the cortical GM – which is known to be present in this patient population (Wardlaw et al., 2013), and is also in line with the reduced GM normalized cortical volume – at a finer spatial scale.

WM FD as a feature of structural complexity

The WM FD assumes a fractional value between 2 and 3, capturing the structural complexity of a highly complex object which fills the space more than a smooth surface (2D), but less than a filled volumetric structure (3D). In our study, we observed a mean FD of cerebral WM of 2.4650 in patients with cerebral SVD and MCI that was significantly lower than that observed in healthy controls. These results are in line with previous works regarding other neurological diseases (Esteban et al., 2007; Cook et al., 1995; Takahashi et al., 2009; Takahashi et al., 2006)

Similarly to the FD of the cortical ribbon (King et al., 2010), the value of the WM FD may depend not only on volumetric changes of subcortical WM, but also on volumetric changes of basal ganglia and lateral ventricles. This is due to the fact that both FDs (of cortical ribbon and WM) are affected by alterations of the GM/WM interface. Ventricular enlargement of lateral ventricles has been described in patients with SVD (Jokinen et al., 2012). We are not aware of studies reporting basal ganglia volume loss in SVD even though this possibility might exist.

FD as a complementary feature in the SVD research field

Our results suggest that the WM FD might be a marker of cognitive performance in patients with SVD and MCI. This result has potentially relevant implications. In fact, FD is a measurement that can be computed in the field of SVD research using standard high-resolution T1-weighted imaging and does not require further dedicated acquisitions. We observed that also other features obtained from quantitative neuroimaging procedures (e.g., WM lesion load) provided predictive value beyond what is available from visual rating of standard features in SVD, which are likely to be easier and less expensive to assess.

Besides WM FD, neuroimaging features frequently selected (> 80%) in our sample of SVD MCI patients included WM lesions load, GM volume, GM mfs, cerebral microbleeds, GM FD, lacunar infarcts, WM Mfs and GM Mfs. Of note, the degree of importance of these features varied across different neuropsychological scores. Overall, the results suggest that the models for prediction of MoCA and SDMT scores are sparser as compared to that obtained for TMT-A. As expected, due to the inherent complexity of the behavioral measurement of cognitive performance, the obtained results also support the view that more than one neuroimaging feature is needed to reliably predict cognitive scores in this patient population and that, in general, different sets of features may be required to predict different scores. This is in accordance with the fact that these features quantify complementary aspects of SVD-related modifications occurring in the brain. In particular, the joint analysis through the FD and brain volumes might provide greater prediction abilities than the use of each measurement separately (King et al., 2009). In fact, it is well known that the FD and volume examine and quantify different structural aspects, thus generally being complementary to each other (Farahibozorg et al., 2015; Free et al., 1996; King et al., 2009).

Taken together, our data suggest that different neuroimaging tools should be used when evaluating the cerebral cortex and the subcortical WM to obtain significant outcomes.

Methodological considerations

We explored predictive abilities of a wide set of standard and advanced neuroimaging features with a machine learning approach (using the out-of-sample error), in line with the goals of achieving the clinical diagnosis on an individual basis. This approach is different from the conventional linear regression analysis applied to the entire dataset in which the possibility of overfitting may not be negligible. In particular, we used LASSO regression in order to perform, at the same time, a multivariate linear regression and feature selection.

Considering the exploratory nature of our study, mainly aimed at evaluating the possible role of WM FD as an additional MRI marker potentially associated with cognitive performance in SVD, we repeated the same model of analysis on several cognitive tests to explore the consistency of the associations across 1) different measurements within the same cognitive domain and 2) several rounds of a nested CV loop (1,000 repetitions). In particular, we chose a 10-fold CV because it offers a favorable bias-variance trade-off (Hastie et al., 2013; Lemm et al., 2011) and is also adequate for model selection (Breiman and Spector, 1992). Fitting all neuropsychological scores simultaneously into a single comprehensive model could also be carried out, but it would probably require a larger dataset in order to learn the different and complex pattern of associations among neuropsychological scores and neuroimaging features.

We considered the main standard features in SVD research in order to take into account important explanatory variables in the models, such as the WM lesion load (accounting for lesions extent), cerebral microbleeds, EPVS, and lacunes. WM and GM volumes have been introduced in the analysis to further consider the impact of macroscopic structural alterations, such as brain atrophy, on cognitive performance. The effect of age, sex, and education has been accounted for using neuropsychological scores corrected according to normative data and using demographic variables as predictors in the models to account for potential residual effects in the patient population. We used both standard and advanced neuroimaging features; in particular, we adopted our algorithm for the estimation of the FD using an automated selection of the fractal scaling window. We feel that the fact that both mfs and Mfs vary across patients with SVD and MCI does not limit the between-scan comparability. In fact, each patient has been studied in his/her optimal fractal scaling window, automatically determined according to the maximization of a best-fit regression. Moreover, spatial scales are 1-D measurements like cortical thickness and we feel that spatial scales should not be normalized, following recommendations suggested for cortical thickness (Ad-Dab'bagh et al., 2005; Schwarz et al., 2016). However, future studies should examine this aspect in more detail.

Limitation and future developments

We enrolled a rather small number of patients. Therefore, our results need to be confirmed in other studies using independent and larger samples. The number of included patients also restricted the possibility of performing analyses with a larger number of neuropsychological tests assessing also different cognitive domains, and with a larger set of neuroimaging features. We thus decided to limit our analyses to tests known to assess cognitive functions that are mainly affected in patients with subcortical vascular disease and using a limited number of features. Admittedly, a more extensive neuropsychological evaluation could offer a more complete appreciation of the respective role of the WM FD and other neuroimaging features in outlining cognitive deficits in patients with SVD.

Our results suggest that, in a sample of patients with SVD and MCI, a set of neuroimaging features (in which the WM FD was the most relevant) predicts cognitive performance and we feel that this is important per se for the SVD research field. At present, we are not able to assess if such significant predictions are due to the SVD and/or MCI condition. This could be investigated in future studies in which a sample of patients with SVD only, a sample of patients with MCI only, and a group of healthy controls will be examined using the same MRI scanner and protocols and the same neuropsychological battery. A larger sample group of healthy subjects would be also valuable for a deeper investigation of possible associations of mfs and Mfs with aging or cognition.

Future studies using longitudinal patient evaluations will investigate whether WM FD might represent an earlier marker of WM damage.

Finally, in our study, we computed the FD of the general structure of the WM. Future studies may explore the structural complexity of the WM surface and WM skeleton. In particular, the skeleton retains peculiar characteristics of the WM morphology (Liu et al., 2003) with a reduced influence of atrophic changes of WM or surrounding brain regions which may increase the variance of the FD estimates in the sample population (Krohn et al., 2019). A joint FD analysis of WM general structure, surface and skeleton may thus more completely characterize the structural complexity of WM in both normal aging and neurological diseases (Zhang et al., 2007b).

We showed that a machine learning approach could be useful in SVD using standard and advanced neuroimaging features. Our study results raise the possibility that FD may represent a consistent feature in predicting cognitive decline in SVD that can complement standard imaging and clinical features in SVD.

4.3 THE MORPHOLOGICAL COMPLEXITY OF THE BRAIN IN PATIENTS WITH CAA

During the second year of my Ph.D., I spent three months abroad, in Boston, where I have worked with the group of the Massachusetts General Hospital, Stroke Research Center, Department of Neurology at Harvard Medical School. The project, granted both by the UNIBO Marco Polo program and the Massachusetts General Hospital, was entitled "Fractal dimension as a measure of cortical complexity of patients with Cerebral Amyloid Angiopathy (CAA)". In this project we propose to study the cortical morphology of patients with CAA, using traditional and fractal morphological descriptors from MR T1-weighted images, acquired at the Massachussets General Hospital (MGH), Boston, MA, USA.

4.3.1 *Materials and methods*

Dataset

CAA is a common microangiopathy in the elderly and is characterized by macroscropic and microscopic lesions both in the cortex and in subcortical structures. Cortical lesions include cerebral microbleeds (Ni et al., 2015), and cortical microinfarcts. The detection of a single microinfarct in a CAA patient potentially indicates the presence of thousands more in the brain (Westover et al., 2013). The cumulative effect of these lesions presumably disrupts cortical architecture which consequently results in cognitive deficits.

A total of 82 patients with probable CAA according to the Modified Boston Criteria were identified from an established large prospective cohort of consecutive patients admitted to the Massachusetts General Hospital with spontaneous symptomatic ICH between January 2006 and July 2017 (for further details see Linn et al., 2010; Xiong et al., 2019). Patients with deep locations of ICH/microbleeds (except cerebellar microbleeds) and patients with inadequate quality of MRI scans were excluded. In particular we excluded 58 patients, since the ICHs visible in the MR T1-weighted images, had altered the brain structure of interest (20 patients presented ICH in the right hemisphere, 15 in the left hemisphere and 23 in both of them). Another patient has been excluded because *FreeSurfer* segmentations were not satisfactory. A total of 23 patients with CAA were included into the final analysis.

In the same way, a sample of 19 healthy controls has been acquired. One subject has been excluded because the *FreeSurfer* procedures failed. A total of 18 healthy controls were included into the final analysis.

All subjects have been acquired on a clinical 1.5 T scanner (Siemens Healthcare, Magnetom Avanto, Erlange, Germany) (further details in Linn et al., 2010).

GM/WM segmentation

In this project we processed all the MR T1-weighted images using the *FreeSurfer* software (Fischl, 2012). The processing time, for each subject, took about 10-13 hours.

The editingprocedure has required a strong collaboration between neurologists/neuroradiologists (for detection and editing of segmentation errors) and biomedical engineers (for translation of the clinicians' information into the software pipeline).

Standard morphological descriptors

We estimated standard morphological measures (i.e., volume, cortical thickness and curvature), by using the *FreeSurfer* suite. We computed both vertex-wise and global measures. In particular, we were interested in the computation of the curvature of the GM/WM interface and pial surfaces, which are the inner and outer boundary of the cortical ribbon, i.e. the cortical GM volume, respectively.

In differential geometry the curvature of a curve in a point is equal to the rate of change of the direction of the tangent with respect to arc length (Lipschutz, 1969). Thus, along a curve which has a rapidly changing tangent direction with respect to arc length, such a circle with a small radius, the curvature is relatively large, or, equivalently, the radius of curvature is small (Lipschutz, 1969). In three dimensions, each point of the surface has different values of curvature, depending on the different directions of the plane normal to the surface at that point. Two main directions can be defined, in which the curvature values assume the maximum (K_1) and minimum (K_2) values. The Gaussian (G) and Mean (H) curvature are a combination of K_1 and K_2 values:

$$G = K_1 * K_2 \tag{20}$$

$$H = \frac{K_1 + K_2}{2} \tag{21}$$

FreeSurfer is able to estimate the Mean and Gaussian curvature for each vertex of the surface under examination. Conventionally, negative curvature values are attributed to the cortical gyri, while positive ones to the curvature of the sulci. In order to keep separated the contributions of gyri and sulci to Gaussian and Mean curvature, we have improved the *FreeSurfer* procedures, to compute and export more detailed information about curvatures of gyry and sulci, separately.

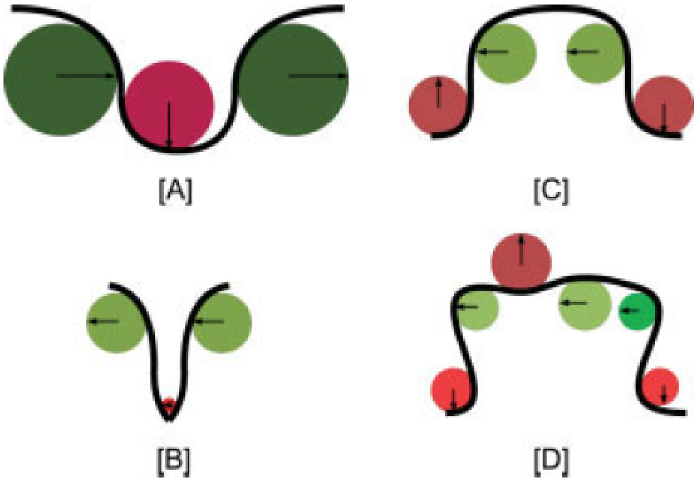

Figure 25: A conceptual illustration of curvature. The measure of "curvature" of a curve can be understood by taking a series of circles that just smoothly "touch" each of the undulations of the curve. The curvature of the curve is proportional to the sum of the inverse radii of each circle. Red circles are in the sulci; green cirles are in the gyri. [A] and [B], effect on curvature by "compressing" sulcal extent; [C] and [D], effect of higher order "bumps" on overall curvature (Pienaar et al., 2008).

Fractal Analysis

We used the improved 3D box counting algorithm with the automated selection of the fractal scaling window to compute the global FD of the cerebral cortical GM (see chapter 3).

All fractal analysis computations have been performed on a Dell PowerEdge T620 workstation equipped with two 8-core Intel Xeon E5-2640 v2, for a total of 32 CPU threads, and 128 GB RAM, using the Oracle Grid Engine batch-queuing system.

Statistical Analysis

Differences between groups (CAA patients vs. healthy subjects) for morphological indexes were evaluated through both surface-based (vertex-wise) and volumetric (global) group analyses. The surface-based group analyses were carried out using the *Freesurfer* suite, to compare morphological measurements of volume (V), cortical thickness (CT) and mean curvature of the GM/WM interface surface (H_white) and of the pial surface (H_pial). We have a chosen a vertex-wise/cluster-forming threshold *th* equal to 1.3 (equivalent to a vertex p-value of 0.05) and a cluster-wise p-value equal to 0.05 for the multiple comparison correction.

The volumetric group analysis to assess differences in global volume (gV), average cortical thickness (aCT), average mean curvature of the GM/WM interface surface sulci (aH_white_sulci) and gyri (aH_white_gyri), average mean curvature of the pial surface sulci (aH_pial_sulci) and gyri (aH_pial_gyri) and fractal dimension (FD) were evaluated through the non-parametric Mann Whitney test. For each test, a significance threshold of 0.05 was applied.

4.3.2 *Results and discussion*

The descriptive statistics of volumetric (global) morphological indices are reported in Table 17.

The average mean curvature of the sulci of the GM/WM interface surface was significantly higher in CAA patients than in healthy controls. The same result has been found also for the pial surface. No significant differences between CAA patients and healthy controls have been found for cerebral cortical GM volume, mean cortical thickness, mean curvature of the gyri and FD values.

The surface-based group analyses results are summarized in Table 18.

CAA patients show higher volume in the left lateral occipital lobe and higher cortical thickness in the left fusiform and in rigth middle temporal lobe than healthy controls. No significant differences have been found between CAA patients and healthy controls in mean curvature values.

From the results of the two different group analyses it can be deduced that the different morphological measures behave differently in the disease: for example, the volume and the cortical thickness are different between CAA and HS only in some delimited areas (left lateral occipital lobe and left fusiform, right middle temporal lobe, respectively), while no difference was found by the Mann-Whitney test on global values.

The mean curvature seems to have an opposite behavior compared to volume and cortical thickness: for the sulci, no differences between CAA patients and healthy subjects have been assessed through the surface-based analyses, while the overall average curvature of the sulci (both of the GM/WM interface surface and of the pial surface) assumes higher values in the CAA than in healthy subjects. Morphologically, this translates into narrower sulci, i.e., a smaller radius of curvature, in CAA patients than in healthy subjects.

Both group analyses revealed no differences in cerebral GM FD values between CAA patients and healthy subjects.

Table 17: Descriptive statistics of volumetric (global) morphological indices.

Morphological feature	CAA patients		Healthy subjects	
	Median	Interquartile range	Median	Interquartile range
Cerebral GM gV	402657.741	72799.8352	394194.603	30493.6732
aCT	2.228	0.140	2.168	0.090
aH_white_sulci	0.137*	0.010	0.130*	0.005
aH_white_gyri	0.159	0.010	0.156	0.010
aH_pial_sulci	0.188*	0.020	0.179*	0.011
aH_pial_gyri	0.180	0.018	0.175	0.010
FD	2.50	0.04	2.50	0.03

* pvalue < 0.05 at Mann Whitney test.

Table 18: Surface-based group analyses results.

Morphological feature	Vertex-wise results
Cerebral GM V	CAA patients show higher volume in left lateral occipital lobe
CT	CAA patients show higher cortical thickness in left fusiform and in right middle temporal lobe
aH_white	No differences between CAA patients and healthy subjects
aH_pial	No differences between CAA patients and healthy subjects

5

DIFFUSION MRI: THE COMPLEXITY OF THE BRAIN MICROSTRUCTURE

Magnetic resonance provides a unique opportunity to quantify the diffusional characteristics of a wide range of human tissues. Because diffusional processes are influenced by the geometrical structure of the environment, MR can be used to probe the microstructural environment non-invasively. This is particularly important in studies that involve biological samples in which the characteristic length of the boundaries influencing diffusion are typically so small that they cannot be resolved by conventional MRI techniques (Johansen-Berg and Behrens, 2009; Jones, 2011). Diffusion is a mass transport process arising in nature, which results in molecular or particle mixing without requiring bulk motion (Johansen-Berg and Behrens, 2009). In particular, 60-80% of our body is made up of water and the heat associated with our body temperature energizes the water molecules, causing them to "jerk" around randomly. This phenomenon is called "Brownian motion", after the scientist who first described it (Brown, 1928; Moritani et al., 2009; Doob, 1942). Three straightforward models can be used to describe water diffusion in tissues: free diffusion in free water and hindered or restricted diffusion in the presence of boundaries such as cell membranes (Van-Hecke et al., 2016). The diffusive properties of water molecules can be analyzed by estimating the diffusion coefficient (formalized in Fick's first law (Fick, 1855a; Fick, 1855b) and then by Einstein (Einstein, 1905; Einstein, 1926)), that is an intrinsic property of the medium, and its value depends on a number of factors which include the size of the diffusing molecules, the temperature and microstructural features of the environment. The sensitivity of the diffusion coefficient on the local microstructure enables its use as a probe of molecular dynamics and structural and physical properties of biological tissue (Johansen-Berg and Behrens, 2009; Jones, 2011). Taking typical values for water diffusion D and diffusion times T_d achievable on conventional MRI equipment (e.g., $D \sim 10^{-3}$ mm²/s at body temperature and $T_d \sim 50$ ms), the root mean squared displacement of water molecules is on the order of 10 μm, which is about the size of many tissue structures, such as cells. Hence, the noninvasive observation of the water diffusion–driven displacement distributions in vivo creates a new source of contrast for MRI, which provides unique clues to the fine structural features and geometric organization of neural tissues according to their physiological or pathological states (Jones, 2011).

Water diffusion

5.1 DIFFUSION TENSOR IMAGING (DTI)

In various tissues, such as white matter, we expect diffusion transport properties to vary with orientation since water molecules are likely to encounter different barriers and obstacles according to the direction in which they move (Jones, 2011; Mori, 2007) (Fig. 26).

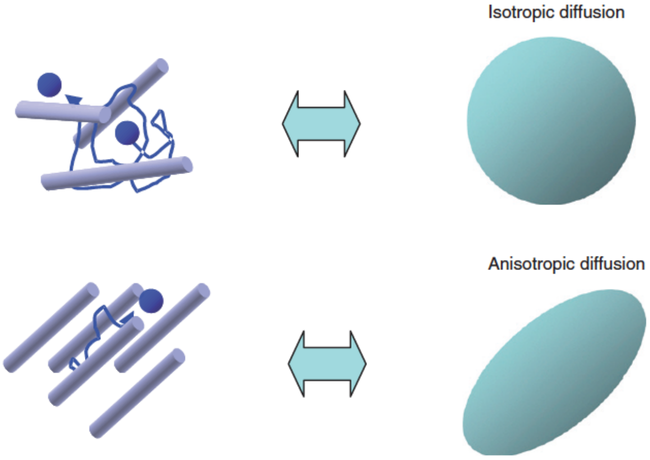

Figure 26: Water diffusion carries information on whether the environment organization is random (isotropic diffusion) or ordered (anisotropic diffusion) (Mori, 2007).

Apparent Diffusion Coefficient

Apparent Diffusion Tensor

In this situation, we can no longer characterize the behavior of the water molecules adequately with a scalar diffusion coefficient. The apparent diffusion coefficient (ADC) we measure will depend on the direction along which we measure it (Johansen-Berg and Behrens, 2009) or, in other words, that it is only sensitive to diffusion with a component along this direction (Van-Hecke et al., 2016). A more general description of anisotropic diffusion uses a 3D Gaussian model of molecular displacements, which contains a symmetric apparent diffusion tensor (ADT) of water (e.g., see Crank, 1975), in place of a scalar ADC to describe the orientation dependence of diffusion (Jones, 2011). The diffusion tensor is often thought of in terms of an ellipsoid – a surface representing the distance that a molecule will diffuse to with equal probability from the origin (Johansen-Berg and Behrens, 2009). We definitely need six parameters to define the tensor (as for an ellipsoid) (Fig. 27): three lengths for the longest, middle and shortest axes that are perpendicular to each other (they are usually called λ_1, λ_2, and λ_3 respectively, or eigenvalues) and three unit vectors to define the orientation of the principal axes (they are called v_1, v_2, and v_3 respectively, or eigenvectors) (Mori, 2007).

In order to measure six diffusion constants along six independent axes, at least seven diffusion-weighted images are needed (one image without the diffusion-weighting, the so called "bo image", and

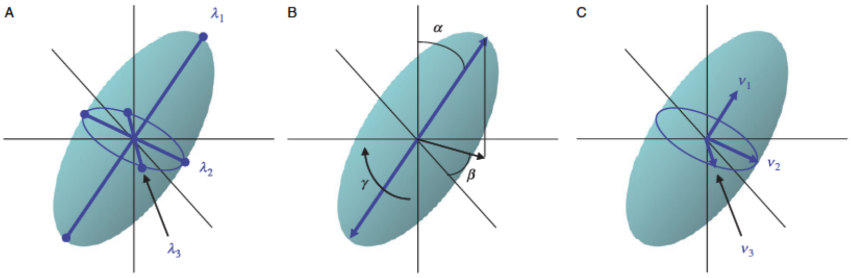

Figure 27: Parametrs needed to define a 3D ellipsoid (Mori, 2007).

six images acquired applying diffusion gradients along six non-collinear and non-coplanar directions) (Fig. 28). In practical situations, we often perform more than seven measurements using different gradient strengths, gradient orientations, or signal averaging to reduce the rotational variance in tensor estimation due to noise, as well as to obtain more reliable diffusion indices (Jones, 2011; Mori, 2007).

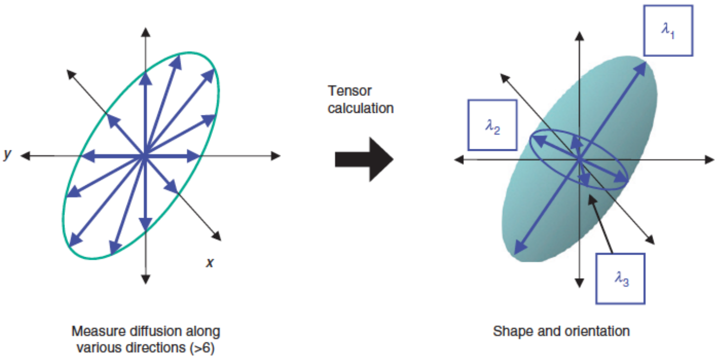

Figure 28: A diffusion ellipsoid can be fully characterized from diffusion measurements along six indipendent axes (Mori, 2007).

DTI-derived indices

Various rotationally invariant DTI indices can be derived from the eigenvalues of the diffusion tensor such as mean diffusivity (MD), axial diffusivity (AxD), radial diffusivity (RD), fractional anisotropy (FA) and mode of anisotropy (MO) (Fig. 29). In particular, MD quantifies water molecules diffusivity independently of direction and is proportional to the trace of the diffusion tensor (Equation 22):

$$MD = \frac{\lambda_1 + \lambda_2 + \lambda_3}{3} = \frac{\mathrm{Trace}(ADT)}{3} = M_1(\lambda) \tag{22}$$

where $M_1(\lambda)$ is the moment of the first order, the mean value, of the λ_i eigenvalues.

Also, AxD (i.e., the largest eigenvalue, $AxD = \lambda_1$) quantifies the amount of water mean diffusivity along the direction of the principal eigenvector. RD is the average of the medium and smallest eigenvalues ($RD = \frac{\lambda_2+\lambda_3}{2}$) and quantifies water diffusivity in the plane perpendicular to the principal eigenvector.

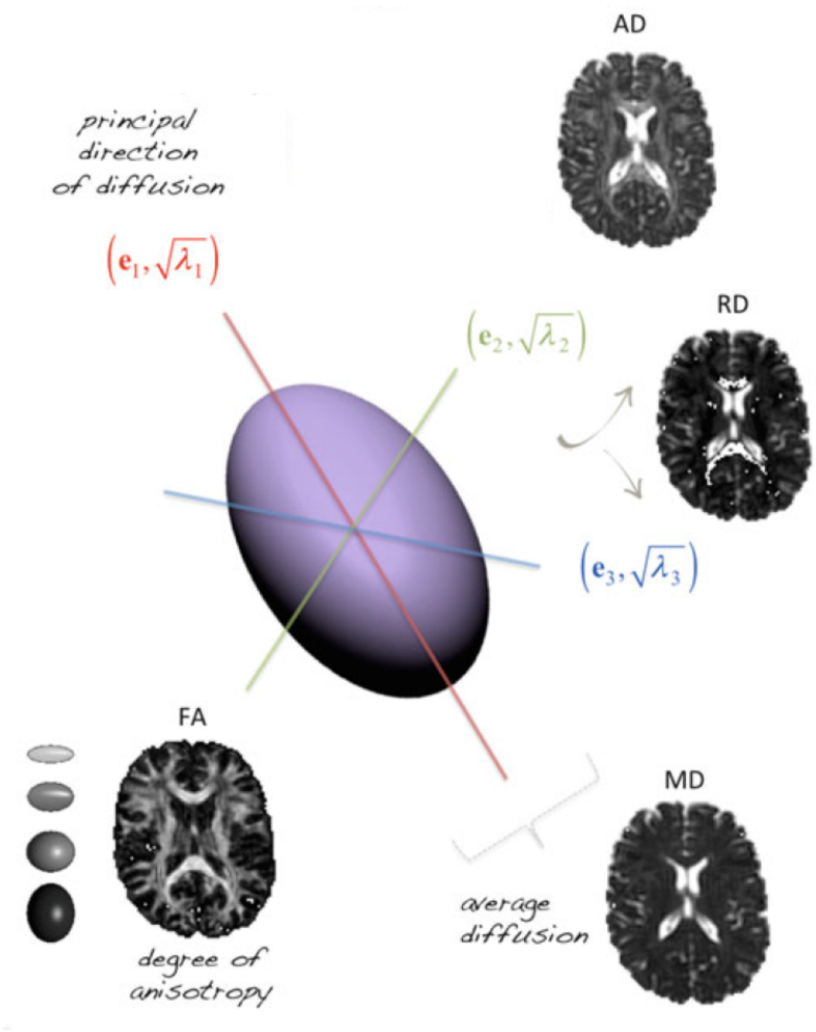

Figure 29: A geometric representation of the diffusion tensor and maps of DTI-derived indices. The longest axis is the first eigenvector and represents the direction of maximal diffusion, along which the axial diffusivity (AxD) is calculated (sometimes referred to as $\lambda_{\|}$, longitudinal, or parallel diffusivity). The second and third eigenvalues are used to calculate the radial diffusivity (RD) (sometimes referred to as $\lambda_{\perp}$, transverse or perpendicular diffusivity). The mean diffusivity (MD) is a measure of the overall diffusivity in a particular voxel regardless of direction and is calculated as the average of the eigenvalues. The degree of diffusion anisotropy can be represented by the fractional anisotropy (FA), a scalar measure (unitless) ranging between 0 (isotropic diffusion—darkest grey on a standard FA map) and 1 (completely anisotropic—lightest grey on a standard FA map) (Van-Hecke et al., 2016).

FA (dimensionless) is the normalized standard deviation of the eigenvalues (Equation 23) and measures the degree of water diffusion anisotropy, ranging from 0 (isotropic diffusion) to 1 (completely anisotropic diffusion).

$$\begin{aligned} FA &= \sqrt{\frac{3}{2}}\frac{\sqrt{(\lambda_1 - M_1)^2 + (\lambda_2 - M_1)^2 + (\lambda_3 - M_1)^2}}{\sqrt{\lambda_1^2 + \lambda_2^2 + \lambda_3^2}} = \\ &= \sqrt{\frac{3}{2}}\frac{\sqrt{M_2(\lambda)}}{\sqrt{\lambda_1^2 + \lambda_2^2 + \lambda_3^2}} \end{aligned} \tag{23}$$

where $M_2(\lambda)$ is the moment of the second order, i.e. the variance, of the λ_i eigenvalues.

MO is a dimensionless measure of anisotropy type, proportional to the skewness, ranging from -1 to +1 (Equation 24).

$$MO = \sqrt{2}M_3M_2^{-3/2} \tag{24}$$

where $M_3(\lambda)$ is the moment of the third order of the λ_i eigenvalues. As we can see in Fig. 30, negative MO values describe planar anisotropy (i.e., two large and one small eigenvalue, as observed for instance in regions of crossing fiber bundles), whereas positive MO values indicate linear anisotropy (i.e., one large and two small eigenvalues, as observed for instance in major fiber bundles) (Ennis and Kindlmann, 2006; Kindlmann et al., 2007).

DTI-derived indices are proven to be sensitive to brain tissue microstructure, which is characterized by various factors including cell and axonal density/size, membrane permeability and integrity, fiber orientation dispersion and myelin sheath. Accordingly, the pattern of variation of DTI-derived indices can provide information about the microstructural changes underlying various brain diseases (Focke et al., 2014; Goveas et al., 2015; Jiang et al., 2014).

5.1.1 *Histogram analysis of DTI-derived indices reveals pontocerebellar degeneration and its progression in SCA2*

Spinocerebellar ataxia type 2 (SCA2) is the second more frequent SCA after SCA3 worldwide (further details about the disease are described in section 4.1).

Brain DWI- or DTI-derived indices have proven to be correlated with severity of clinical deficit in several cross-sectional studies of patients with SCA2 (Mascalchi and Vella, 2012; Hernandez-Castillo et al., 2015; Mandelli et al., 2007; Hernandez-Castillo et al., 2016), and may represent potential biomarkers of disease progression in longitudinal studies of neurodegenerative diseases including inherited or sporadic degenerative ataxias (Baldarcara et al., 2015). So far, this possibility has been explored through regions of interest

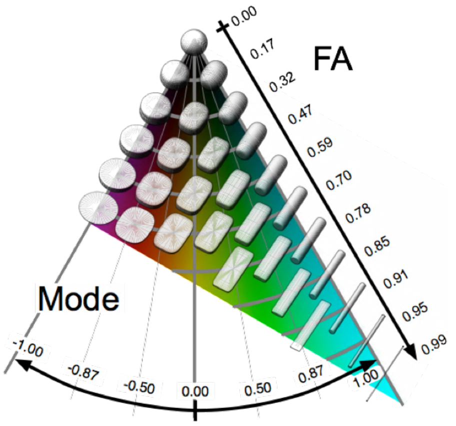

Figure 30: Demonstration of the space of anisotropy decomposed into two orthogonal channels: fractional anisotropy (FA) and mode (MO). Each glyph represents the shape of diffusion tensors with constant tensor norm rendered with superquadric glyphs. Increasing distance from the top left spherical glyph indicates increasing FA, whereas the angular deviation from the left edge indicates increasing mode as it transitions from planar anisotropic ($\mathrm{MO} = -1$), to orthotropic ($\mathrm{MO} = 0$), to linear anisotropic ($\mathrm{MO} = 1$). Glyphs along constant radii (constrained to an arc) are of constant fractional anisotropy, but of varying mode. This figure shows that increases in FA do not necessarily indicate increasing linear anisotropy. The space of FA and mode is correctly diagrammed as an isosceles triangle; note that isocontours of FA are orthogonal to isocontours of mode (Ennis and Kindlmann, 2006).

(ROIs) (Pellecchia et al., 2011; Reginold et al., 2014) or voxel-wise tract based spatial statistics (TBSS) (Smith et al., 2006) analysis of DTI data (Mascalchi et al., 2015; Mascalchi et al., 2016). While TBSS can provide whole brain and unbiased local information on the changes caused by disease, it is inherently restricted to WM skeleton (Smith et al., 2006) assessment. Moreover, TBSS requires accurate normalization of maps of DTI-derived indices to a template (Keihaninejad et al., 2012) and is based on a number of assumptions which may not be satisfied, affecting the reliability of results (Bach et al., 2014). In particular, small choices in the preprocessing pipeline may have a relevant effect on test-retest reliability, therefore influencing the power to detect change within a longitudinal study (Madhyastha et al., 2014).

A histogram analysis of DWI- or DTI-derived indices of the whole or segmented brain structures to assess microstructural damage in degenerative ataxias (including SCA2) has been previously proposed (Della Nave et al., 2008b). This approach has a number of advantages as compared to ROI and TBSS methods, albeit it implies loss of spatial information on local changes. Notably, given that correction for multiple comparisons across several voxels or ROIs is not needed, a higher statistical power may be obtained. Also, histogram analysis can be extended to GM regions. Finally, in principle, analysis of normalized histograms can be performed without coregistration of maps of diffusion indices to a template. To date, there is only one longitudinal study that used histogram analysis of DTI-derived indices of the whole brain and whole WM in a neurodegenerative disorder, namely, Huntington disease (Odish et al., 2015).

In this longitudinal study, we carried out, in SCA2, histogram analysis of several DTI-derived indices of the segmented cerebrum and brainstem-cerebellum, including both WM and GM, in order to: 1) investigate whether such a relatively straightforward approach has the potential to reveal and track progression of microstructural damage; 2) preliminarily assess if the rate of change of histogram metrics of DTI-derived indices correlates with clinical deterioration.

5.1.1.1 *Materials and methods*

SUBJECTS

We examined 9 patients (3 women and 6 men; age 48.7±12.9 years, mean ± standard deviation) with a genetically determined SCA2 and 16 age- and gender-matched healthy subjects (7 women and 9 men; age 50.3±18.8 years, mean ± standard deviation). All subjects underwent MRI twice. More details are described in section 4.1.

MRI EXAMINATION

A 1.5 T MRI scanner (Philips Intera, Best, The Netherlands) equipped with 33 mT/m maximum gradient strength and 6-channel phased-array head coil was utilized for baseline and follow- up MRI examinations in all patients and controls. The acquisition parameters of the T1-weighted images are described in section 4.1. In addition, axial diffusion-weighted images were obtained with a single-shot echo-planar imaging sequence (TR = 9394 ms, TE = 89 ms, FOV = 256 mm × 256 mm, matrix size = 128×128, 50 slices, slice thickness = 3 mm, no gap, number of excitations = 3). Diffusion sensitizing gradients were applied along 15 non-collinear and non-coplanar directions with b-value of 0 (b_0 image) and 1000 s/mm². T1-weighted and diffusion-weighted images were visually evaluated by a neuroradiologist for the identification of artifacts before entering further image processing. After this visual quality control, all images were retained for further processing.

GRAY AND WHITE MATTER SEGMENTATION

Completely automated cortical reconstruction and segmentation of the subcortical WM of each subject were performed by means of T1-weighted images and *FreeSurfer* image analysis suite v. 5.3, as described in section 4.1. For each subject, the segmentation masks of GM/WM of cerebrum were merged in order to obtain a unique region mask for cerebrum, while the segmentation masks of GM/WM of brainstem and cerebellum were merged in order to obtain a unique region mask for brainstem-cerebellum (Fig. 31). Cerebral segmentation and brainstem-cerebellum segmentation for a representative SCA2 patient are shown in Fig. 32.

DTI PROCESSING

Diffusion-weighted images were corrected for head motion and eddy current distortions using FDT (FMRIB's Diffusion Toolbox 2.0; FMRIB, Oxford Center for Functional MRI of the Brain), part of FSL (FMRIB Software Library) version 5.0.8 (Smith et al., 2004). Skull was removed using the FSL brain extraction tool (BET) (Smith, 2002). The b-matrix was reoriented by applying the rotational part of the affine transformation employed in the head motion and eddy current correction procedure (Leemans and Jones, 2009). Then, using the RESTORE diffusion tensor estimation (Chang et al., 2005) implemented in the CAMINO software package (Cook et al., 2006), a tensor model was fitted to processed DWI data. In this study, the DTI-derived indices of MD, FA, AxD, RD and MO were estimated using DTI-TK version 2.3.1 (Zhang et al., 2007a), FSL tools and in-house Bash shell scripts.

HISTOGRAM ANALYSIS

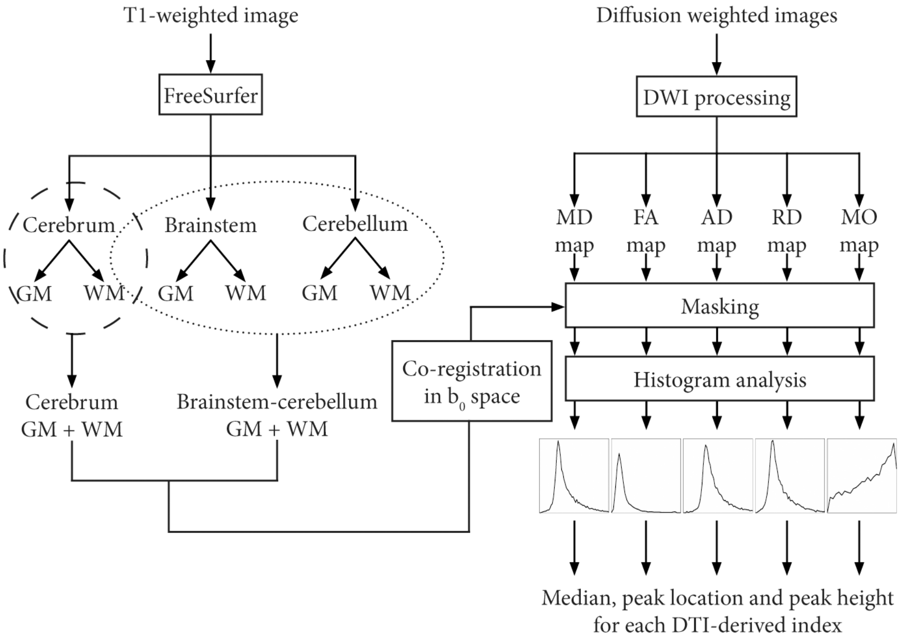

Figure 31: Processing pipeline for T1-weighted and diffusion-weighted images of a single subject (Mascalchi et al., 2018).

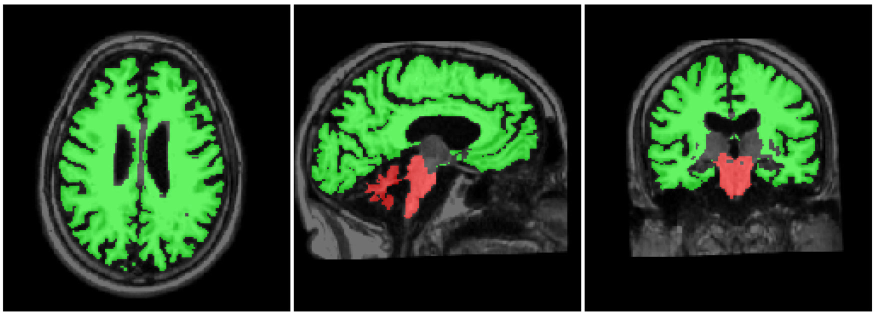

Figure 32: Example of GM/WM matter segmentation of cerebrum (green) and brainstem-cerebellum (red) in a representative SCA2 patient (Mascalchi et al., 2018).

For each subject, the cerebrum and brainstem-cerebellum segmentations were converted from the *FreeSurfer* space back to the native anatomical space, and the T1-weighted image in the native space was co-registered to the b0 image using the 12 degrees of freedom affine transformation implemented in FSL FLIRT (FMRIB's Linear Image Registration Tool) (Jenkinson et al., 2002). This affine transformation was then applied to cerebrum and brainstem-cerebellum segmentation (Fig. 31).

For each cerebrum and brainstem-cerebellum segmentation in the b0 space, the histogram (normalized over the total number of voxels) of MD/FA/AxD/RD/MO was computed. The normalization allows to correct for individual differences in brain size. In this study, we used three histogram metrics of DTI-derived indices: the median value, the peak location and peak height (Fig 33). The median is the value of the DTI-derived index (i.e., MD, FA, AxD, RD or MO) that divides the higher half of the data sample from the lower half. The peak location is the mode of the histogram, i.e. the most frequent value assumed by the DTI-derived index; the value of the histogram assumed at the peak location is the histogram peak height which is the maximum value of the histogram.

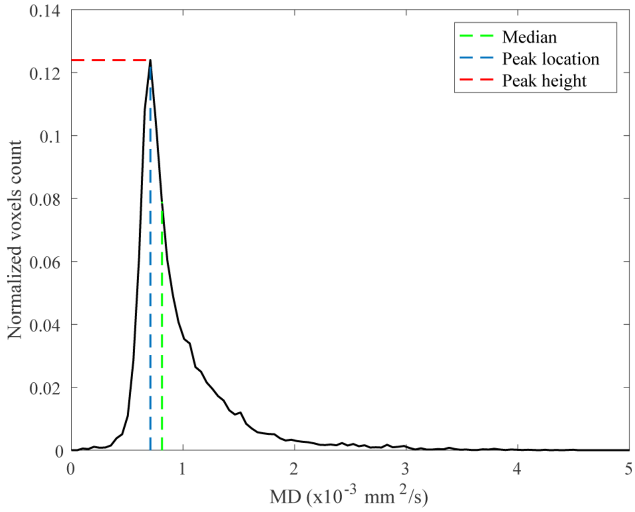

Figure 33: Example of histogram showing the 3 three histogram metrics we used: The median value, the peak location and peak height (Mascalchi et al., 2018).

DATA ANALYSIS

At baseline, differences in histogram metrics of DTI-derived indices between SCA2 patients and control subjects were assessed through the non-parametric Mann Whitney test. For each histogram metric, the rate of change (i.e., the ratio between the change over time and the time to- follow-up) was computed. Then, the non-parametric Mann Whitney test was employed in order to assess any difference in rate of change between SCA2 patients and control subjects. In SCA2 patients, the Pearson coefficient was employed in order to assess any linear correlation between the rate of change of histogram metrics of DTI-derived indices and clinical data (i.e., number of triplets in the longer allele, disease duration at baseline, clinical progression as assessed by the rate of change in IACRS and ICARS). For each test, the Holm-Bonferroni correction for multiple comparisons was applied (significance threshold of 0.05), in order to control the family wise error rate. Finally, in order to evaluate the sensitivity to change of ICARS, IACRS and histogram metrics of those DTI-derived indices showing rate of change significantly different between SCA2 patients and controls, we used the standardised response mean (SRM).

5.1.1.2 *Results*

The descriptive statistics of histogram metrics of DTI-derived indices are reported in Table 19.

Histograms of DTI-derived indices of control subjects and SCA2 patients groups are shown in Fig. 34.

At baseline, significant differences between SCA2 patients and controls were confined to brainstem-cerebellum. In particular, median values of MD/AxD/RD and FA/MO were significantly ($p<0.001$) higher and lower, respectively, in SCA2 patients than controls (Table 19). Also, peak location values of MD/AxD/RD and FA were significantly ($p<0.001$) higher and lower, respectively, in SCA2 patients than controls (Table 19). Peak height values of FA and MD/AxD/RD/MO were significantly ($p<0.001$) higher and lower, respectively, in SCA2 patients than controls (Table 19).

The rate of change of MD median values was significantly ($p<0.001$) higher (i.e., increased) in SCA2 patients than controls in the brainstem-cerebellum (Table 19). No other significant difference in rates of change of histogram metrics of MD and other DTI-derived indices between SCA2 patients and controls was found.

No significant correlation between the rate of change of histogram metrics of DTI-derived indices and disease duration, number of triplets or rate of change of the IACRS or ICARS scores was observed.

The SRM of the median MD in cerebellum-brainstem was intermediate (SRM = 1.2) between that of ICARS (SRM = 1.0) and IACRS (SRM = 1.3).

5.1.1.3 *Discussion*

SCA2 belongs to the polyglutamine diseases group that comprises nine neurodegenerative conditions which share abnormal expansion

Table 19: Histogram metrics of DTI-derived indices in control subjects and SCA2 patients. Median (interquartile range) data are reported. MD/AxD/RD median and peak location are expressed in x10^{-3} mm^2/s, while FA/MO median and peak location are unitless.

	Baseline		Rate of change	
	Controls	SCA2 patients	Controls	SCA2 patients
Cerebrum				
MD median	0.81 (0.02)	0.82 (0.03)	0.002 (0.005)	0.004 (0.007)
MD peak location	0.76 (0.00)	0.76 (0.05)	0.000 (0.000)	0.000 (0.000)
MD peak height	0.14 (0.02)	0.13 (0.03)	-0.001 (0.003)	-0.002 (0.003)
FA median	0.21 (0.02)	0.21 (0.01)	-0.001 (0.004)	-0.001 (0.003)
FA peak location	0.09 (0.00)	0.09 (0.00)	0.000 (0.000)	0.000 (0.004)
FA peak height	0.11 (0.01)	0.10 (0.01)	0.001 (0.002)	0.000 (0.001)
AxD median	1.05 (0.05)	1.06 (0.03)	0.002 (0.007)	0.003 (0.005)
AxD peak location	0.96 (0.05)	1.01 (0.01)	0.000 (0.013)	0.000 (0.000)
AxD peak height	0.1 (0.02)	0.09 (0.01)	-0.001 (0.003)	-0.001 (0.003)
RD median	0.69 (0.02)	0.71 (0.02)	0.001 (0.005)	0.004 (0.008)
RD peak location	0.63 (0.05)	0.66 (0.01)	0.000 (0.000)	0.000 (0.000)
RD peak height	0.11 (0.01)	0.11 (0.02)	0.000 (0.002)	-0.001 (0.002)
MO median	0.37 (0.03)	0.35 (0.03)	0.001 (0.004)	-0.003 (0.005)
MO peak location	0.92 (0.00)	0.92 (0.00)	0.000 (0.000)	0.000 (0.000)
MO peak height	0.09 (0.00)	0.09 (0.00)	0.000 (0.001)	0.000 (0.001)
Brainstem-cerebellum				
MD median	0.8 (0.03)	1.11 (0.12)*	-0.003 (0.006)*	0.010 (0.014)*
MD peak location	0.71 (0.00)*	0.91 (0.1)*	0.000 (0.000)	0.000 (0.026)
MD peak height	0.14 (0.02)*	0.07 (0.02)*	0.001 (0.006)	-0.001 (0.002)
FA median	0.20 (0.02)*	0.14 (0.02)*	0.001 (0.006)	-0.001 (0.006)
FA peak location	0.18 (0.03)*	0.12 (0.00)*	0.000 (0.000)	0.000 (0.010)
FA peak height	0.15 (0.02)*	0.2 (0.03)*	-0.001 (0.005)	-0.002 (0.007)
AxD median	1.00 (0.05)*	1.3 (0.12)*	-0.002 (0.011)	0.010 (0.018)
AxD peak location	0.91 (0.05)*	1.11 (0.18)*	0.000 (0.006)	0.000 (0.051)
AxD peak height	0.11 (0.02)*	0.06 (0.01)*	0.001 (0.004)	-0.001 (0.002)
RD median	0.7 (0.03)*	1.03 (0.11)*	-0.004 (0.008)	0.011 (0.018)
RD peak location	0.63 (0.05)*	0.81 (0.13)*	0.000 (0.006)	0.000 (0.016)
RD peak height	0.12 (0.02)*	0.07 (0.01)*	0.000 (0.005)	-0.001 (0.002)
MO median	0.41 (0.11)*	0.19 (0.13)*	-0.003 (0.029)	-0.006 (0.023)
MO peak location	0.92 (0.00)	0.92 (0.00)	0.000 (0.000)	0.000 (0.025)
MO peak height	0.09 (0.02)*	0.07 (0.01)*	-0.001 (0.006)	-0.002 (0.004)

$*$ significant differences ($p<0.001$) between controls and SCA2 patients after Holm-Bonferroni correction for multiple comparisons (Mascalchi et al., 2018).

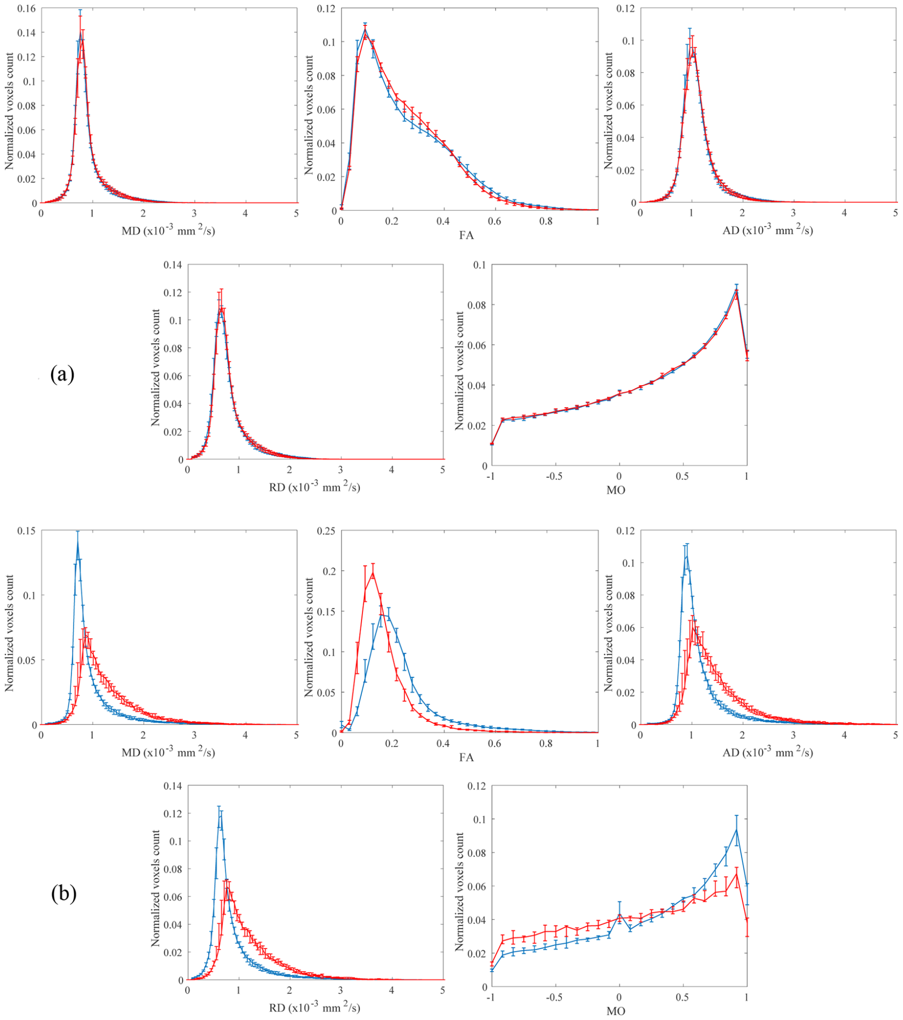

Figure 34: The histograms (median with the interquartile range) of control subjects (blue line) and SCA2 patients (red line) groups of DTI-derived indices of cerebrum (a) and cerebellum-brainstem (b) are shown. The bin width is 0.05x10^{-3} mm²/s for MD/AxD/RD, 0.03 for FA and 0.08 for MO. MD/AxD/RD (median, peak location) and FA/MO (median, peak location) are reported as x10^{-3} mm²/s and unitless, respectively (Mascalchi et al., 2018).

of a CAG triplet in the coding region of the mutated gene as fundamental pathogenetic mechanism (Auburger, 2012).

SCA2 is a neurodegenerative disease that is progressive and ultimately fatal. So far, the therapeutic window to slow, halt and hopefully reverse the degenerative process in SCA2 has not been established yet. Identification and comparison of reliable and sensitive markers of disease progression potentially serving as primary or surrogate markers in future trials, including quantitative MRI (Baldarcara et al., 2015), represent hence active areas of research. Several clinical measurements of disease progression in SCA2 and in ataxias in general have been proposed (Filla et al., 1990; Trouillas et al., 1997). However, all clinical scales are subjective and are deemed not to be fairly sensitive to disease progression (Sakai and Miyoshi, 2002).

The results of this study suggest that histogram metrics of DTI-derived indices may be a useful tool to reveal microstructural changes associated with the brainstem-cerebellum degeneration in SCA2 patients. In particular, MD is able to track modification over time of the microstructural changes and can represent a potential biomarker of disease progression.

The modifications of the histogram metrics and distribution of DTI-derived indexes in SCA2 patients, as compared to control subjects, at baseline (and follow-up) are in line with the general features of DTI changes in neurodegenerative diseases (Goveas et al., 2015). In fact, both the increase (implying a more pronounced peak) of voxels exhibiting lower values (implying a shift to the left), in case of FA, and the decrease (implying a less pronounced peak) of voxels exhibiting variably higher values (implying a shift to the right), in case of MD/AxD/RD, is likely to reflect tissue loosening. In case of MO, the peak height is reduced, and the histogram values are higher for negative values of MO, meaning that the mode of anisotropy tends to change from linear anisotropy (MO = 1) to planar anisotropy (MO = -1).

Notably, while increased MD and RD and decreased FA of the affected nervous tissue are generally observed in patients with various neurodegenerative disorders as compared to healthy controls (Goveas et al., 2015), AxD and MO can have a dual (increase/decrease) pattern of change in the same patient group (Mascalchi et al., 2015; Della Nave et al., 2008b). In the present study, at baseline we observed higher median and peak location values of AxD in SCA2 patients as compared to control subjects. This is consistent with previous data in Friedreich's ataxia and Huntington disease (Odish et al., 2015; Della Nave et al., 2011; Rosas et al., 2010), suggesting that, neurodegeneration may be associated with increased AxD. The pathophysiological interpretation of this phenomenon is not well established, albeit some studies have hypothesized an increased extracellular water content secondary to atrophy of the WM fibers, which would allow faster water molecule movement parallel to axons, alterations of axonal water content and flux secondary to breakdown or accumulation of certain constituents of the cytoskeleton and a possible contribution of glial alterations (Rosas et al., 2010).

The capability of histogram analysis of the MD to track progression of pontocerebellar degeneration integrates previous findings (Mascalchi et al., 2015) and further supports the potential of DTI in assessing longitudinal changes in SCA2. In a previous TBSS study (Mascalchi et al., 2015), AxD and MO indices showed longitudinal changes in SCA2 patients as compared to control subjects. In particular, AxD changes were significantly greater (i.e., increased) in patients with SCA2 than in controls in WM tracts of the right cerebral hemisphere and corpus callosum, but not in the brainstem or cerebellum, whereas longitudinal MO changes were significantly lower (i.e., decreased) in patients with SCA2 than controls in hemispheric cerebral WM, corpus callosum, internal capsules, pons and left cerebellar peduncles, cerebral peduncles and WM of the left paramedian vermis. In this histogram study, longitudinal changes of the median values of MD were significantly greater (i.e., increased) in patients with SCA2 than controls in the whole brainstem-cerebellum. Importantly, this capability of MD to reveal progression of neurodegeneration in SCA2 is consistent with an increase of tissue loosening and replicates findings obtained with ROIs or TBSS analyses in other neurodegenerative disorders, including MSA, Huntington disease and Alzheimer disease (Reginold et al., 2014; Goveas et al., 2015).

In this study, we preliminary explored whether the rate of changes of histogram metrics of DTI-derived indices correlated with disease duration and the rate of change of the clinical deficit. In agreement with a previous TBSS study (Mascalchi et al., 2015), no significant correlation was observed. Nonetheless, our results support the hypothesis that DTI-derived indices, in particular MD, may constitute potential non-invasive and sensitive biomarkers of disease progression in degenerative ataxias (Baldarcara et al., 2015).

The SRM of the two clinical scales in our SCA2 patients were comparable to those of other clinical scales in a morphometric study of SCA1, SCA3 and SCA6 (Reetz et al., 2013). The slightly higher value of IACRS presumably reflect inclusion of additional non-cerebellar deficits in this scale and the degeneration of additional neural structures beside the cerebellum in SCA2 (Auburger, 2012). In our study, the SRM of the median MD in cerebellum-brainstem was intermediate between the two clinical scales, but lower than those reported for several morphometric features in the above study of SCA1, SCA3 and SCA6 (Reetz et al., 2013). This might imply a relatively lower sensitivity of the microstructure changes revealed by DTI as compared to those of morphometry or reflect disease specific differences. However, this issue deserves to be addressed in future studies.

We recognize some limitations of this study. First, due to hardware and software constraints, we used a DTI acquisition protocol with only 15 diffusion weighting directions, resulting in a potential reduction of statistical power of the study. However, given that our histogram analysis includes mostly gray matter with relatively isotropic diffusion and white matter regions with low/moderate diffusion anisotropy (i.e., FA < 0.6) (see Fig. 34), the use of 15 diffusion weighting directions, albeit not optimal, can be assumed to be sufficient to minimize the rotational variance due to noise in the estimation of DTI-derived indices of MD and FA (Jones, 2004). Second, admittedly, we arbitrarily decided to re-scan the patients (and controls) only once after a relatively long period of time since basal MRI. However, this interval is clinically reasonable (and tentatively adequate for therapeutic trials) and was justified, on the one hand, by the lack of any clue about the minimum time required to observe changes of DTI-derived indices in SCA2 and inherited pontocerebellar degenerations and, on the other hand, by the small number of patients in our cohort that might have entailed a possible beta error if they were rescanned in a shorter period. Additional time points and greater sample sizes might enable a more accurate assessment of the dynamic of the neurodegenerative process. Finally, we performed a single center study, while using of DTI-derived indices as biomarker in rare diseases such as SCA2 would greatly benefit of multi-center studies. In this regard, histogram analysis of DTI-derived indices of segmented brain, given its simplicity and high reproducibility (Steens et al., 2004), might be adopted in future multi-centric studies such as the ENIGMA-Ataxia project (enigma@ini.usc.edu).

In conclusion, histogram analysis of DTI-derived indices including MD, FA, AxD, RD and MO is a relatively straightforward approach that is capable to reveal WM and GM microstructural changes associated with pontocerebellar degeneration in SCA2. Moreover, the median value of MD in the brainstem-cerebellum is capable to track progression of pontocerebellar degeneration. Histogram metrics of DTI-derived indices could hence serve as biomarkers of disease status and progression in SCA2.

5.2 ADVANCED DTI-DERIVED FRACTAL DESCRIPTORS

Fractal analysis using the box-counting algorithm and the automated selection of the fractal scaling window can also be performed on representations of the human brain other than the general structure, i.e. the volume obtained from MR T1-weighted images. For the WM, in particular, it is interesting to study the fractal properties of the skeleton, which preserves the topology of the general structure and the connections between different areas. In the previous literature, several works have analyzed the WM skeleton (Liu et al., 2003; Ha et al., 2005; Zhang et al., 2006; Zhang et al., 2007b; Esteban et al., 2007; Rajagopalan et al., 2013; Farahibozorg et al., 2015; Sheelakumari et al., 2017), showing results complementary to those obtained from the study of the T1-weigthing-derived volumes only. There are several techniques for obtaining the skeleton of an image and the majority of works in literature (Liu et al., 2003; Ha et al., 2005; Zhang et al., 2006; Zhang et al., 2007b; Esteban et al., 2007; Farahibozorg et al., 2015) have computed firstly 2D slice-by-slice skeleton in one direction, e.g., sagittal, and then, the skeletonized slices were integrated into a 3D skeleton volume, which represented cortical folding pattern (Ha et al., 2005). We think that a useful representation of the WM skeleton can be obtained from the diffusion-weighted images, using the FA map, derived from the diffusion tensor.

In this section, the preliminary results of the fractal analysis of DTI-derived skeleton in two different neurological diseases will be presented.

5.2.1 *Materials and methods*

PARTICIPANTS

The first dataset is the aforementioned (see section 4.1) SCA2 dataset, including 9 patients with spinocerebellar ataxia of type 2 and 16 age- and gender-matched healthy controls. Each subject has been scanned twice (for further details see Mascalchi et al., 2018; Marzi et al., 2018a).

The second dataset contains 22 patients with cerebral autosomal dominant arteriopathy with subcortical infarcts and leukoencephalopathy (CADASIL) and 16 age- and gender-matched healthy controls. CADASIL is the most frequent inherited brain SVD. Common clinical manifestations of CADASIL are migraine, transient ischemic attacks or strokes, psychiatric disorders, and progressive cognitive impairment in midage adults (Chabriat et al., 2009). Conventional MRI shows a leukoencephalopathy very similar to that observed in elderly hypertensive patients, especially in the WM tracts (Chabriat et al., 2009).

All the MR examinations of this dataset were performed on a 3 T system (Achieva, Philips Healthcare, Best, The Netherlands, Release 2.6.3.7) equipped with an eight-channel phased-array headcoil and the details of MRI protocol are showed in Table 20.

After the segmentation process using the *FreeSurfer* suite, the dataset was composed by 21 CADASIL patients (9 men and 12 women, age 41.7 ± 10.9 years [mean ± standard deviation], range 25 - 63 years) and 16 controls (8 men and 8 women, mean age 42.4 ± 12.6 years, range 27 - 63 years). No significant differences between age (p-value = 0.87 at t-test) and gender (p-value = 0.67 at χ^2-test) in the two groups was found.

Table 20: MRI examination protocol of CADASIL dataset.

	Sagittal 3D T1-weighted turbo gradient echo	Axial single-shot echo planar imaging
TR / TE / TI (ms)	8.1 / 3.7 / 926	9364 / 60
FLA	8	-
FOV	220 mm x 220 mm	256 mm x 256 mm
matrix size	220 x 220	128 x 128
number of slices	155	75
slice thickness	1 mm	2 mm
interslice gap	0 mm	0 mm
NEX	1	2
b-values (s/mm^2)	-	[0, 1000]
diffusion weighting directions	-	32

METHODS

The same T1-weighted and DW-image processing was performed for both datasets (Fig. 35).

Firstly, the DWI data were processed as described in Mascalchi et al., 2018. Briefly, the tensor model was fitted to processed DWI data using the RESTORE diffusion tensor estimation (Chang et al., 2005), implemented in the CAMINO software package (Cook et al., 2006). Then the DTI-derived index of FA was estimated using DTI-TK version 2.3.1 (Zhang et al., 2007a), FSL tools and in-house Bash shell scripts. The skeleton of the FA map was created using FSL's tbss_skeleton script (Smith et al., 2006) and thresholded at FA>0.2 to obtain a binary image (Fig. 36).

The T1-weighted images were processed by using *FreeSurfer* suite (Fischl, 2012) (v. 5.3 for SCA2 dataset and v. 6 for CADASIL dataset), in order to obtain the WM segmentation of each subject. In this preliminary study, we chose to analyze the WM only because it is well represented by the skeleton.

Then, the cerebral (and cerebellar for SCA2 dataset, since the patients present predominant structural alterations at the cerebellar level) WM segmentations were converted from the *FreeSurfer* space back to the native anatomical space, and the T1-weighted images in the native space were co-registered to the b_0 image using the affine (with 12 degrees of freedom) transformation implemented in FSL FLIRT (FMRIB's Linear Image Registration Tool) (Jenkinson et al., 2002). This affine transformation was then applied to cerebral (and cerebellar for SCA2 dataset) WM segmentation in order to mask the FA skeleton image (Fig. 35).

The fractal analysis with the automated selection of the fractal scaling window (for further details see chapter 3) was then computed on cerebral (and cerebellar for SCA2 dataset) WM skeleton images, i.e. the FA-derived skeletons masked by the WM segmentations obtained from the T1-weighted images.

In addition, with the aim of harmonizing the analyses with the works already published on SCA2 patients (Mascalchi et al., 2018; Marzi et al., 2018a), in the CADASIL dataset, the maps of FA and MD of the cerebral WM were investigated by histogram analysis (Mascalchi et al., 2018). The fractal analysis was also applied to the general structure of the cerebral WM extracted from the T1-weighted images using *FreeSurfer* (Marzi et al., 2018a).

In the SCA2 dataset, differences in FD values of cerebral and cerebellar WM skeletons were evaluated at baseline through a Mann-Whitney test. For each FD value, the rate of change (defined as the ratio between the modification over time and time-to-follow-up) was computed and differences between groups evaluated through a Mann-Whitney test.

In the CADASIL dataset, differences between groups were assessed through the non-parametric Mann Whitney test on histogram metrics of DTI-derived indices (FA and MD maps) and FD values of cerebral WM general structure and skeleton.

For both datasets, the significance threshold was set at 0.05.

5.2.2 *Results and discussion*

Table 21 shows the results for the SCA2 dataset. To simplify the discussion of the preliminary results of the fractal analysis applied to the skeletons of the cerebral WM, Table 21 also shows the main results of the same dataset concerning the histogram analysis of the FA and MD maps (Mascalchi et al., 2018) and the FD values of cerebral and cerebellar WM (Marzi et al., 2018a). As already mentioned in section 2.1.4, the FD values of the skeletons are lower than those of the general structure in both patients and controls. In the SCA2 dataset, the fractal analysis applied to skeletons did not add information compared to the study of the general structure alone. In the cerebrum, the FD values of either the WM general structure and the WM skeleton, were not able to significantly

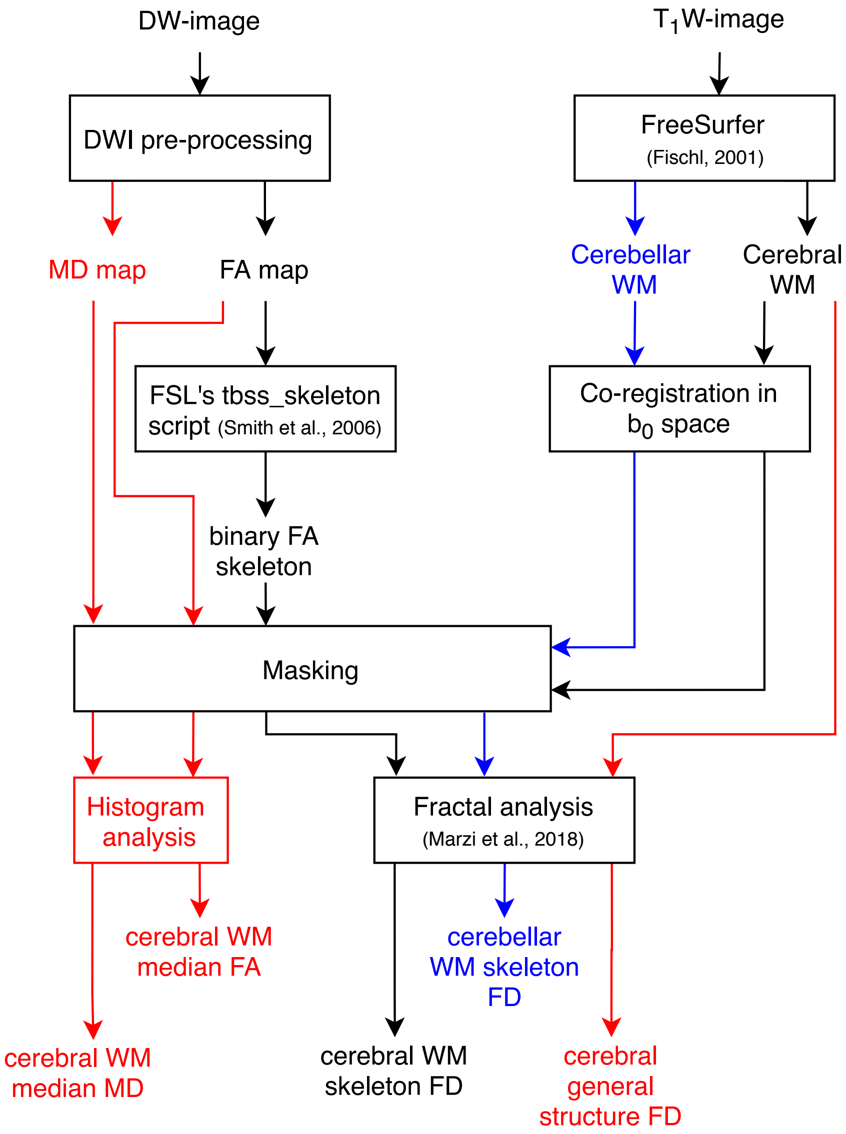

Figure 35: Processing pipeline for T1-weighted and diffusion-weighted images of a single subject in this preliminary study. Red text and lines indicate analyses performed only on the CADSIL dataset. Blue text and lines indicate analyses performed only on the SCA2 dataset. Black text and lines indicate analyses performed on both the CADASIL and SCA2 datasets.

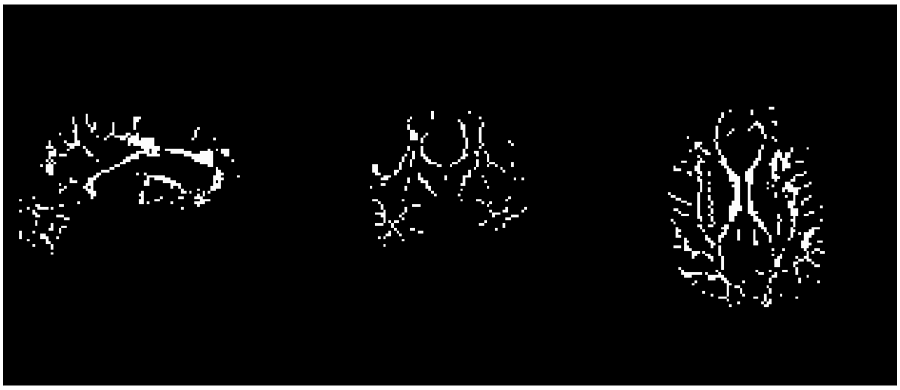

Figure 36: A sagittal, coronal and axial slice of the cerebral WM skeleton in one CADASIL patient.

discriminate SCA2 patients and controls, both at baseline and using the rate of change. Differently, at the cerebellar level, SCA2 patients showed significant lower FD values than those of controls, both for the T1-derived WM general structure for the DTI-derived WM skeleton. The reduction of the morphological complexity of the cerebellar WM in SCA2 patients has been already figured out in Marzi et al., 2018a, where only the WM general structure was analyzed by means of fractal analysis with the automated selection of the fractal scaling window.

Table 22 shows the results for the CADASIL dataset. Even in this dataset, the FD values of the skeleton are lower than those of the general structure in both groups. In this case, the FD values of WM skeleton added complementary information. Indeed, there are no significant differences between CADASIL patients and healthy controls in the FD values of the general structure, while FD of skeletons were lower in CADASIL patients than in healthy subjects. Similarly, significant differences were found in the histograms medians values of MD and FA maps between CADASIL patients and healthy controls. These preliminary results suggest that changes in MD and FA indices, which quantify the water molecules diffusivity and its degree of anisotropy, respectively, could be due by real subtle modifications of the WM microstructure and morphological complexity, as measured by the FD values of the WM skeleton.

5.3 DIFFUSION KURTOSIS IMAGING (DKI)

We have already covered the case of Gaussian diffusion and shown how to characterize its properties in biological tissues using DTI (see section 5.1). However, biological tissues such as the cerebral WM are highly heterogeneous media that consist of various individual

Table 21: Histogram medians of MD and FA indices [from Mascalchi et al., 2018], FD values of cerebral and cerebellar WM general structure [from Marzi et al., 2018a] and skeletons in control subjects and SCA2 patients. Median (interquartile range) data are reported. MD median is expressed in $x10^{-3}$ mm^2/s, while FA median and FD are unitless.

	Baseline		Rate of change	
	Controls	SCA2 patients	Controls	SCA2 patients
Cerebrum				
MD median	0.81 (0.02)	0.82 (0.03)	0.002 (0.005)	0.004 (0.007)
FA median	0.21 (0.02)	0.21 (0.01)	-0.001 (0.004)	-0.001 (0.003)
WM FD	2.52 (0.02)	2.53 (0.02)	0.000 (0.003)	-0.002 (0.007)
WM skeleton FD	2.22 (0.04)	2.23 (0.03)	0.000 (0.010)	-0.010 (0.010)
Brainstem-cerebellum				
MD median	0.8 (0.03)*	1.11 (0.12)*	-0.003 (0.006)*	0.010 (0.014)*
FA median	0.20 (0.02)*	0.14 (0.02)*	0.001 (0.006)	-0.001 (0.006)
WM FD	2.56 (0.19)*	1.74 (0.10)*	0.001 (0.033)	0.009 (0.092)
WM skeleton FD	1.80 (0.04)*	1.63 (0.06)*	0.000 (0.010)	0.000 (0.030)

$*$ significant differences ($p<0.01$) between controls and SCA2 patients at Mann-Whitney test.

Table 22: Histogram medians of MD and FA indices, FD values of WM general structures and skeletons in control subjects and CADASIL patients. Median (interquartile range) data are reported. MD median is expressed in $x10^{-3}$ mm^2/s, while FA median and FD are unitless.

	Controls	CADASIL patients
MD median	0.71 (0.03)*	0.78 (0.08)*
FA median	0.42 (0.03)*	0.39 (0.08)*
WM FD	2.53 (0.02)	2.51 (0.03)
WM skeleton FD	2.25 (0.03)*	2.23 (0.03)*

$*$ significant differences ($p<0.05$) between controls and CADASIL patients at Mann-Whitney test.

compartments (e.g., intracellular, extracellular, neurons, glial cells, and axons) and barriers (e.g., cell membranes and myelin sheaths). Therefore, the random movement of water molecules is hindered and/or restricted by compartmental boundaries and other molecular obstacles (Van-Hecke et al., 2016).

Restricted diffusion

Restricted diffusion occurs when water molecules are constrained by impermeable boundaries, which impedes the progress of water molecules beyond a certain maximum displacement in a particular direction. In the context of biological tissues, this kind of diffusion occurs for water molecules trapped inside a cell boundary, otherwise known as the "intracellular" region. For instance, the diffusion of water molecules confined within the intra-axonal spaces is expected to be restricted. In this regime, the diffusion properties of water are largely governed by the geometric properties of the constraining membrane (Van-Hecke et al., 2016).

Hindered diffusion

Differently, *Hindered* diffusion occurs when the progress of water molecules, as they diffuse, is impeded by obstacles, but not completely confined by a continuous boundary as in the case of restricted diffusion. In biological tissue, this type of diffusion is exhibited by water present in the interstitial space between cells, otherwise known as the "extracellular" region (Van-Hecke et al., 2016). A graphical representation of restricted and hindered diffusion is shown in Fig. 37.

As we can see in Fig. 38, in case of free and hindered diffusion, the mean squared displacement linearly increases with the diffusion time. Thus, like free diffusion, hindered diffusion can still be described by a Gaussian distribution. However, the width of the distribution will be smaller than one might expect based on properties of the tissue water itself (Van-Hecke et al., 2016).

For restricted diffusion, on the other hand, the mean squared displacement converges to an upper bound, which relates to the size of the bounding microstructure (Van-Hecke et al., 2016).

Given the size of a typical diffusion-weighted MRI voxel (about 2x2x2 - 3x3x3 mm^3), the biological tissue within a voxel is expected to contain a mixture of free, hindered and restricted compartments with different diffusion properties (Assaf et al., 2004; Assaf and Basser, 2005; Van-Hecke et al., 2016). Therefore, the assumption of Gaussian diffusion made in DTI (Basser, 1995), is no longer satisfied (Van-Hecke et al., 2016). A more advanced diffusion model is required, that allows to properly describe the deviation from a Gaussian distribution (Van-Hecke et al., 2016). This deviation from Gaussian behavior can be quantified using a convenient dimensionless metric called the excess kurtosis, shortened to kurtosis (Jensen et al., 2005). The kurtosis is a dimensionless statistical metric for quantifying the non-Gaussianity of an arbitrary probability distribution (Decarlo, 1997). If M_n is the nth moment of

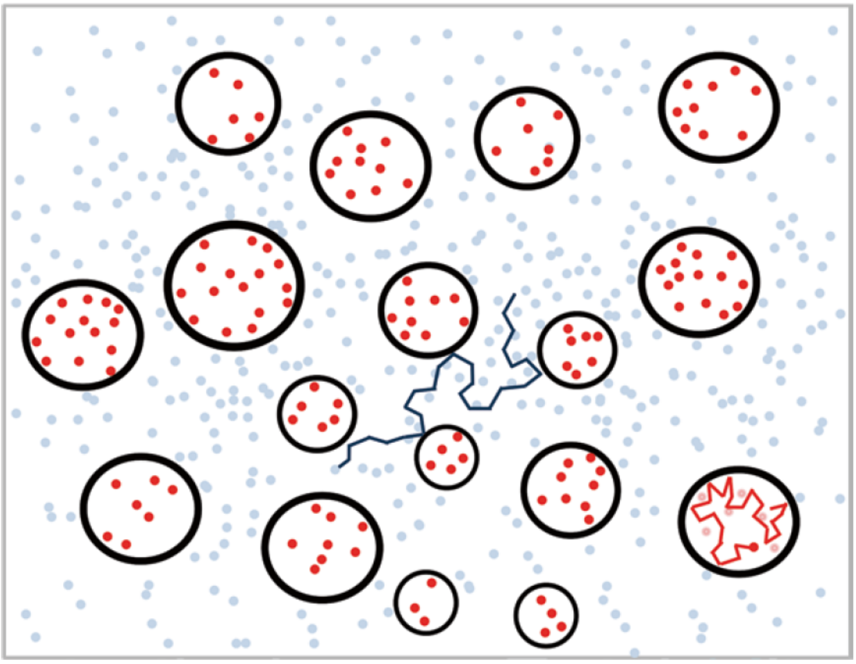

Figure 37: Illustration of hindered and restricted water diffusion inside and around boundaries, such as cell membranes. The red dots represent molecules which are restricted by the presence of the boundaries while the blue dots represent molecules which are hindered by the presence of the boundaries (Van-Hecke et al., 2016).

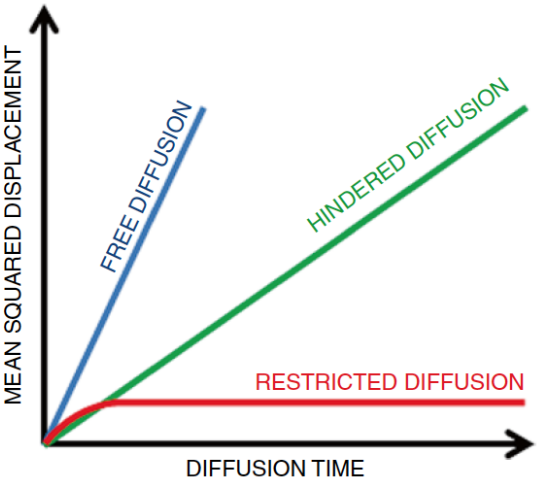

Figure 38: Mean squared displacements are shown as a function of the diffusion time for free (blue), hindered (green), and restricted (red) diffusion (Van-Hecke et al., 2016).

a distribution about its mean value, then the kurtosis may be defined as $K = \frac{M_4}{M_2} - 3$ (Jensen and Helpern, 2010). As it is shown in Fig. 39, the kurtosis is a measure of peakedness or sharpness of an arbitrary distribution. For a Gaussian distribution $K = 0$, while a positive kurtosis indicates that distribution is more peaked than a Gaussian distribution (Jensen and Helpern, 2010; Van-Hecke et al., 2016).

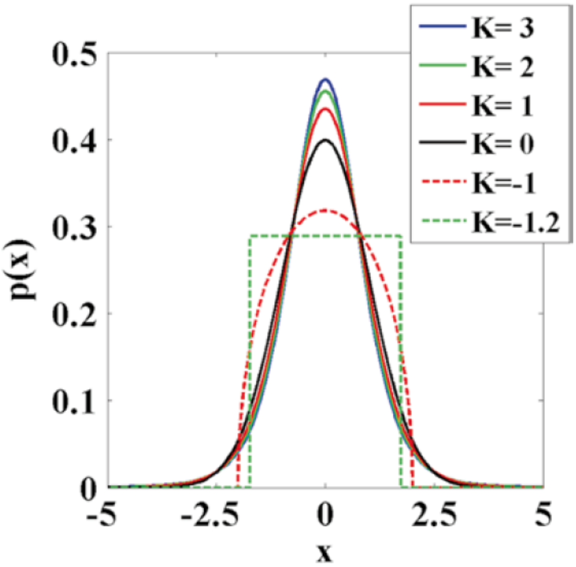

Figure 39: Distributions with varying kurtosis, but with the same mean and variance are shown (Van-Hecke et al., 2016).

Diffusion Kurtosis Tensor

In general, as that happens for the ADC (see section 5.1), the measured diffusional kurtosis is dependent on the direction (Jensen et al., 2005). This directional dependence can be represented by a diffusion kurtosis tensor (Jensen et al., 2005; Lu et al., 2006; Van-Hecke et al., 2016). Thus, Diffusional Kurtosis Imaging (DKI) is a clinically feasible extension of DTI that enables the characterization of non-Gaussian diffusion by estimating the kurtosis of the displacement distribution (Tabesh et al., 2011). The DKI model is parameterized by the symmetric rank 2 diffusion tensor (DT) (6 independent elements) and symmetric rank 3 kurtosis tensor (KT) (15 independent elements) from which several rotationally invariant scalar measures are extracted. As we have already seen in section 5.1, the most common DT-derived measures are mean, axial, and radial diffusivity (MD, AD, RD, respectively), as well as fractional anisotropy (FA). The KT-derived measures include axial, radial, and mean kurtoses (Jensen et al., 2005; Lu et al., 2006; Hui et al., 2008; Tabesh et al., 2011). The axial kurtosis is the apparent kurtosis along the principle diffusion direction (Hui et al., 2008). The radial kurtosis is the average apparent kurtosis coefficient, measured in the equatorial plane (Poot et al., 2010), whereas the mean kurtosis is the average of apparent diffusion kurtosis coefficients along all directions (Lu et al., 2006; Van-Hecke et al., 2016).

In terms of data acquisition, DKI is also a straightforward extension of DTI, because the same type of pulse sequences employed for conventional DWI can be used to record the images (Jensen et al., 2005; Van-Hecke et al., 2016). Diffusion-weighted images along at least 15 non-collinear and non-coplanar diffusion directions and with a minimum of 3 distinct b-values (including b-value = 0 s/mm²) are needed to estimate the diffusion and kurtosis tensors in DKI. Typically, the highest b-value is somewhat higher than in DTI acquisitions and it has been shown that b-values of about 2000 s/mm² are sufficient to measure the degree of non-Gaussianity with an acceptable precision (Fig. 40) (Jensen and Helpern, 2010; Van-Hecke et al., 2016).

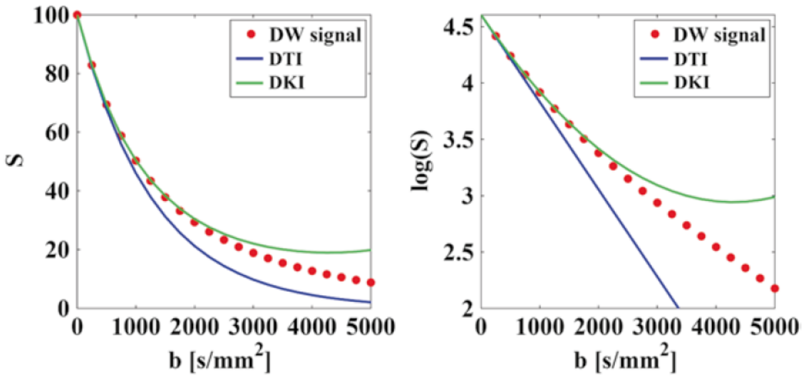

Figure 40: Diffusion-weighted signals (left), as well as their log-transformation (right) are shown as a function of the b-value: measured values (red dots), DTI model (blue), and DKI model (green). Owing to the non-Gaussian diffusion the DKI model improves the accuracy of the fit. This is mainly noticeable up to intermediate/high b-values. At very high b-values, severe approximation errors can affect also DKI (Van-Hecke et al., 2016).

5.3.1 *Body Diffusion Kurtosis Imaging*

DKI-derived indices are sensitive to tissue microstructure also in extra-cranial regions such as prostate, liver, kidney, bladder and breast (Giannelli and Toschi, 2016). The interpretability of the kurtosis metrics is influenced by reliable estimation of the kurtosis tensor (Tabesh et al., 2011). In body DKI, there is currently no standardized approach to characterize and quantify the non-Gaussian component of water diffusion from DWIs. In this regard, a few studies (Quentin et al., 2014; Pentang et al., 2014; Huang et al., 2015; Wu et al., 2014) have computed a DKI-derived index of mean diffusional kurtosis (Jensen and Helpern, 2010) by estimating the kurtosis tensor or averaging diffusional kurtosis estimated along multiple ($\geqslant$ 15) acquired diffusion weighting directions (as is common practice in neuroimaging applications of DKI (Fieremans et al., 2013; Falangola et al., 2013; Lee et al., 2013; Cauter et al., 2012; Raab et al., 2010; Coutu et al., 2014; Falangola et al., 2008). On the other hand, given the practical and stringent need to contain acquisition time in most routine body MRI exams, acquisition of only three DWIs along the main x, y, z orthogonal directions is becoming the de facto standard in body DKI. In this scenario, given that the full kurtosis tensor cannot be estimated, the best-possible approximation for mean diffusional kurtosis can be obtained by separately fitting the DKI model along each diffusion weighting direction x, y, z prior to averaging. However, there is a widespread and growing tendency to perform a single fit of the non-Gaussian DKI model using the geometric means of diffusion-weighted images (i.e., diffusion tensor trace-weighted images (Basser and Jones, 2002), commonly known as trace-weighted (TW) images) (Jambor et al., 2014; Suo et al., 2014; Bourne et al., 2014; Mazzoni et al., 2014; Quentin et al., 2012; Rosenkrantz et al., 2012b; Rosenkrantz et al., 2012a; Nogueira et al., 2014; Iima et al., 2015; Rosenkrantz et al., 2015). Given that geometrical averaging of DWIs implicitly assumes Gaussian signal attenuation as a function of b-value (which incidentally would imply zero diffusional kurtosis and hence eliminate the advantages of the DKI approach), it has been hypothesized that this practice can represent a source of inaccuracy in quantitative DKI (Giannelli and Toschi, 2016), as demonstrated in head and neck application of DKI (Marzi et al., 2018b).

For these reasons, we wrote two letters, published on "Radiology" (Giannelli et al., 2017) and "American Journal of Neuroradiology (AJNR)" (Giannelli et al., 2019), respectively. The aim of these letters is to underline the importance of performing DKI only under the conditions previously described [acquisition of at least 15 diffusion-weighted directions and a minimum of 3 distinct b-values (including b-value = 0 s/mm^2)], so that the results are accurate, reproducible and comparable.

5.4 NEURITE ORIENTATION DISPERSION AND DENSITY IMAGING (NODDI)

Whilst DTI and DKI are matemathical models of the diffusion/weighted signal and do not assume a specific biophysical tissue model, other MRI based frameworks aim to incorporate additional features into their models that reflect some properties of tissue microstructure such as the different behavior of water in intracellular and extracellular compartments (Panagiotaki et al., 2012; Van-Hecke et al., 2016). The complexity of the brain microstructure may depend on the morphology of the neurites, which corresponds to the protrusions of the neuronal soma, i.e., axons and dendrites (Fig. 41).

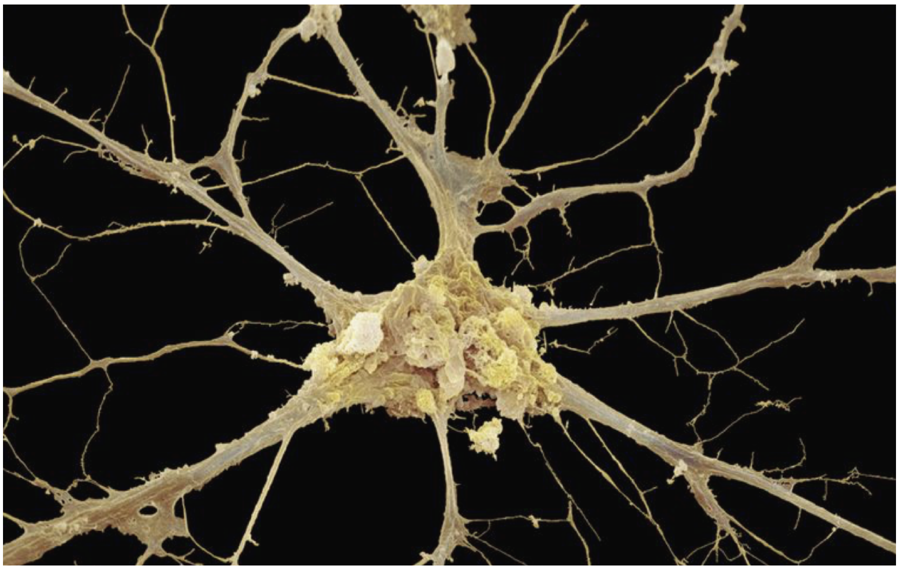

Figure 41: This is a colored scanning electron micrograph (SEM) of a neuron (nerve cell). The cell body is the central structure with neurites (long and thin structures) radiating outwards from it. A neurite is a general term used for processes connecting nerve cells together to form a network of nervous tissue (Abbott, 2010).

The neurite morphology can be quantitatively described by its density and orientation distribution; it contributes to the knowledge of the morphological basis of brain function both in healthy and diseased subjects (Zhang et al., 2012). To describe the neurites morphology, Zhang and colleagues, (Zhang et al., 2012), proposed a non-Gaussian diffusion technique called "neurite orientation dispersion and density imaging (NODDI)", based on a biophysical model of the brain tissue. The NODDI tissue model is sufficiently simple, but complex enough to capture the key features of neurite morphology (Zhang et al., 2012). NODDI adopts a tissue model that distinguishes three types of microstructural environment: intra-cellular, extra-cellular and CSF compartments. The water diffusion is different in each compartment (Le Bihan and Warach, 1995) and produces differentiated normalized MR signal. The full normalized signal A can be written as:

$$A = (1 - \nu_{iso})[\nu_{ic} A_{ic} + (1 - \nu_{ic}) A_{ec}] + \nu_{iso} A_{iso} \tag{25}$$

where:

A_{ic} = normalized signal of the intra-cellular compartment;

v_{ic} = volume fraction of the intra-cellular compartment;

A_{ec} = normalized signal of the extracellular compartment;

A_{iso} = normalized signal of the CSF compartment;

v_{iso} = volume fraction of the CSF compartment.

The intra-cellular compartment refers to the space bounded by the membrane of neurites. They modeled this space as a set of sticks, i.e., cylinders of zero radius, with restricted diffusion (Behrens et al., 2003; Panagiotaki et al., 2012; Sotiropoulos et al., 2012; Zhang et al., 2012). The extra-cellular compartment refers to the space around the neurites, which is occupied by various types of glial cells and, additionally in GM, cell bodies (somas). The neurites hinder, but not restrict, the water molecules diffusion in the extracellular compartment and thus it is modeled with Gaussian anisotropic diffusion (Zhang et al., 2012). The CSF compartment models the space occupied by cerebrospinal fluid and is modeled as isotropic Gaussian diffusion (Zhang et al., 2012).

The procedure to fit the model to data is an adapted version of the routine described in Alexander et al., 2010. Briefly, the procedure determines the maximum likelihood estimates of the parameters, using a Rician noise model, with the Gauss-Newton nonlinear optimization technique (Zhang et al., 2012). The fitting procedure allows the estimation of the three main parameters of the NODDI model, which can be displayed in maps:

1. v_{ic} is the neurite density and represents the intra-cellular volume fraction

2. *OD* is the "Orientation Dispersion" index; $\mathrm{OD} = \frac{2}{\pi}\arctan(\frac{1}{k})$, where k is the concentration parameter that measures the extent of orientation dispersion about the mean orientation, μ, of neurites (Zhang et al., 2012)

3. v_{iso} is the isotropic volume fraction

As we can see in Figs. 42 and 43, the v_{ic} map shows the expected pattern of neurite density (Jespersen et al., 2010). The v_{ic} value is lower in GM than in WM and it takes its highest values in the major WM tracts, such as the corpus callosum and the internal capsules (Zhang et al., 2012). Furthermore the neurite density seems to be a good measure of structural alterations in demyelination disorders (e.g. multiple sclerosis) (Jespersen et al., 2010; Zhang et al., 2012).

Also the *OD* map demonstrates an expected trend that is similarly expected (Figs. 42 and 43). The *OD* value is higher in GM than in WM and it takes its lowest values in the corpus callosum. The orientation dispersion index of neurites has two broad applications. The bending and fanning of axons in WM can be measured by the orientation dispersion index, which is helpful for mapping brain connectivity (Kaden et al., 2007). In particular, it will be useful to decide whether many voxels currently classified as having crossing fibers (Jeurissen et al., 2010) may consist of orientation-dispersed fibers with only a single dominant orientation. Mapping orientation dispersion overtime may shed new light into the process of brain development (Jespersen et al., 2012). In GM, the index quantifies the pattern of sprawling dendritic processes (Zhang et al., 2012).

Similarly, expected results were also found in the map of v_{iso}, which takes its highest values for the CSF regions, such as the ventricles (Figs. 42 and 43) (Zhang et al., 2012).

In principle, NODDI offers an opportunity to extend the application of neurite morphology quantification from being confined within the realm of postmortem histology to becoming a part of routine clinical practice (Zhang et al., 2012). Indeed, NODDI has been developed for clinically feasible and in vivo analyses. With this aim, Zhang and colleagues proposed an acquisition protocol for NODDI model, under scanner hardware and acquisition time constraints typical in clinical setting (Zhang et al., 2012): one shell of b-value=711 s/mm^2 and 30 diffusion directions, one shell of b-value=2855 s/mm^2 and 60 diffusion directions and diffusion-weighted images with null b-value. This acquisition protocol allows a total scanning time of about 25 minutes (Zhang et al., 2012). However, the estimation of the model parameters performed on the whole brain is computationally very expensive: on a standard workstation with two quad-core 3.0 GHz Intel processors, by splitting the computation over 8 cores, the whole brain fitting requires about 3 h (Zhang et al., 2012).

For this reason, Daducci and colleagues, in 2015 (Daducci et al., 2015), have proposed a general framework for Accelerated Microstructure Imaging via Convex Optimization (AMICO) and have shown how to re-formulate the NODDI model as convenient linear systems which can be efficiently solved using fast algorithms (Daducci et al., 2015). Their results demonstrate that AMICO represents an effective means to drastically accelerate the fit of existing techniques (up to four orders of magnitude faster) while preserving accuracy and precision in the estimated model parameters (coefficient of correlation above 0.9). Although Daducci and colleagues have asserted that AMICO is able to preserve a good accuracy and precision in the estimation of the parameters of the NODDI model derived from simulated data, only a qualitative comparison has been made in the case of real data. They showed difference maps between the original and the convex approach: v_{iso} maps estimated by the two approaches appear almost identical; in fact, the average absolute difference between the original NODDI and their AMICO approach over the whole brain is 0.004 ± 0.009

(mean and standard deviation). Also, no significant discrepancies can be observed in the maps of the intra-cellular volume fraction v_{ic}, with the exception of few voxels, especially at the boundary with CSF. The average absolute difference is a bit higher in this case, i.e., 0.032 ± 0.119; however, if they exclude these boundary voxels from the analysis, they obtain a more indicative measure of the actual discrepancy between the two methods in the brain, i.e., 0.015 ± 0.028. The *OD* maps estimated with the two algorithms are almost indistinguishable, with an average absolute difference of 0.018 ± 0.022.

In the following section, the preliminary results of a quantitative comparison of two estimations of the main NODDI model-derived indices, i.e., v_{ic}, *ODI* and v_{iso}, will be presented. In particular, the NODDI model-derived indices have been calculated on a sample of real data (diffusion-weighted images acquired from healthy subjects), using both the original toolbox [NODDI toolbox on Matlab, (Zhang et al., 2012)] and the one proposed by Daducci and colleagues [AMICO on Python, (Daducci et al., 2015)].

5.4.1 *NODDI vs. AMICO*

The sample used in this analysis consists of 17 healthy subjects (12 men and 5 women, age 64 ± 7 years, mean ± standard deviation, range $54 - 77$ years), which underwent diffusion MRI scanning with a single-shot echo-planar imaging sequence (TR = 8500 ms, TE = 101 ms, FOV = 269 mm x 269 mm, matrix size = 96 x 96, 60 slices, slice thickness 2.8 mm, no gap). Diffusion sensitizing gradients were applied along 64 non-collinear and non-coplanar directions with b-value of 1000 and 2500 s/mm^2 (NEX = 1, time 9 minutes and 38 seconds). The b_0 images (b-value = 0 s/mm^2) were also acquired (NEX = 9, time 1 minute and 42 seconds).

5.4.1.1 *Methods*

DWI PRE-PROCESSING

The preliminary visual evaluations of all b_0 and diffusion-weighted images revealed no motion artifacts in any subject. Diffusion weighted-images were corrected for head motion and eddy current distortions by using the FMRIB Diffusion Toolbox, part of the FMRIB Software Library (FSL 5.0.8) (Smith et al., 2006). Afterwards, brain tissue was segmented by using the FSL Brain Extraction Tool. The b-matrix was subsequently reoriented by applying the rotational part of the affine transformation used in the motion- and eddy current-correction step (Leemans and Jones, 2009).

NODDI MODEL-DERIVED INDICES COMPUTATION

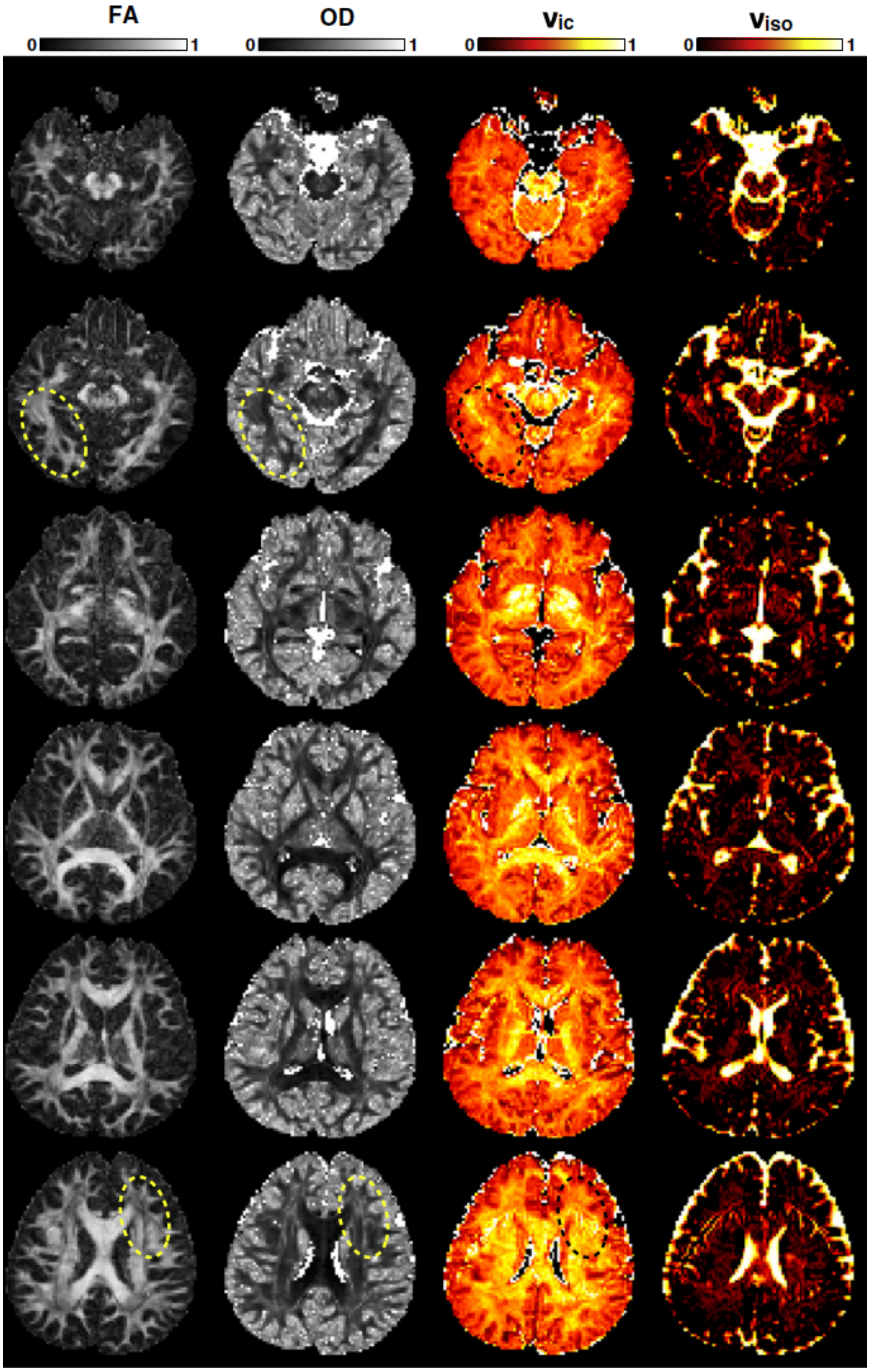

Figure 42: Maps of *FA*, orientation disperison index *OD*, intra-cellular volume fraction (v_{ic}), and isotropic (CSF) volume fraction v_{iso}, showing every 4th slice of the inferior half of the brain (modified from Zhang et al., 2012).

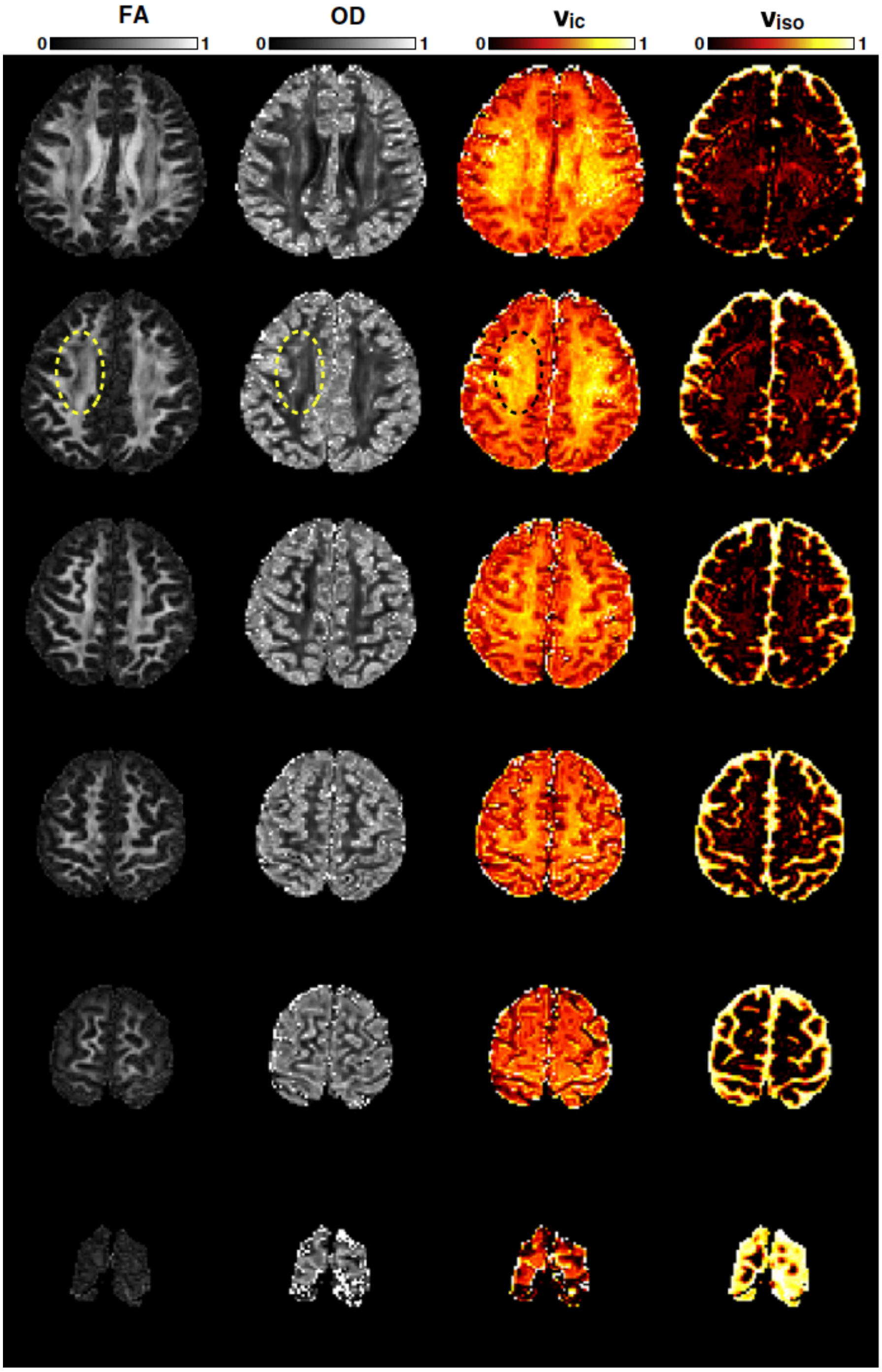

Figure 43: As in Fig. 42, but for the superior half of the brain (modified from Zhang et al., 2012).

Each NODDI model-derived index, i.e., v_{ic}, ODI and v_{iso}, was calculated using both the original toolbox [NODDI toolbox version 1.0.1 available at https://www.nitrc.org/projects/noddi_toolbox (Zhang et al., 2012)], and the procedure proposed by Daducci and colleagues [AMICO toolbox available at https://github.com/daducci/AMICO (Daducci et al., 2015)]. The original NODDI toolbox was performed by using MATLAB R2018a on a Dell PowerEdge T620 platform equipped with two 8-core Intel Xeon E5-2640 v2, for a total of 32 CPU threads and 128 GB of RAM. The computation of the NODDI tissue model for each subject took 16 cores. AMICO toolbox, instead, was written and executed in Python version 3.7.0 and executed on a Mac notebook, equipped with a dual-core Intel Core i7 processor, 16 GB of RAM memory. The NODDI model computation using the AMICO toolbox has been performed using only one core.

For each subject, we obtained six 3D maps: v_{ic_NODDI}, ODI_{NODDI}, v_{iso_NODDI} and v_{ic_AMICO}, ODI_{AMICO}, v_{iso_AMICO} (Fig. 44).

STATISTICAL ANALYSIS

The two different approaches for computing the NODDI model have been compared quantitatively both in terms of computational performances, i.e., the execution time of NODDI model computation, and results, considering as the gold-standard the maps produced by the original toolbox. The three NODDI model-derived maps have been compared using Tract-Based Spatial Statistics (TBSS) (Smith et al., 2006) as well as whole brain woxel-wise statistical analysis. The former has been carried out using FSL's suite scripts, while for the latter we have previously created an anatomical specific template for our 17 healthy subjects and performed a tensor-based co-registration of each subject's map on the template, by using DTI-TK version 2.3.1 (Zhang et al., 2007a). We performed a within-subjects comparison of NODDI model-derived indices between NODDI original and AMICO toolbox outputs through a GLM analysis. The p-values were calculated employing permutation-based statistics (5,000 permutations) and corrected for multiple comparisons using the parameter settings with threshold-free cluster enhancement (TFCE), thereby avoiding the use of an arbitrary threshold for the initial cluster formation (Smith and Nichols, 2009). A p-value < 0.05 corrected for multiple comparisons across space (family-wise error rate correction) was considered statistically significant (Winkler et al., 2014).

5.4.1.2 *Results and discussion*

As already demonstrated by Daducci and colleagues (Daducci et al., 2015) using simulated images, even in our sample of MR images belonging to a group of healthy subjects, the computation of NODDI

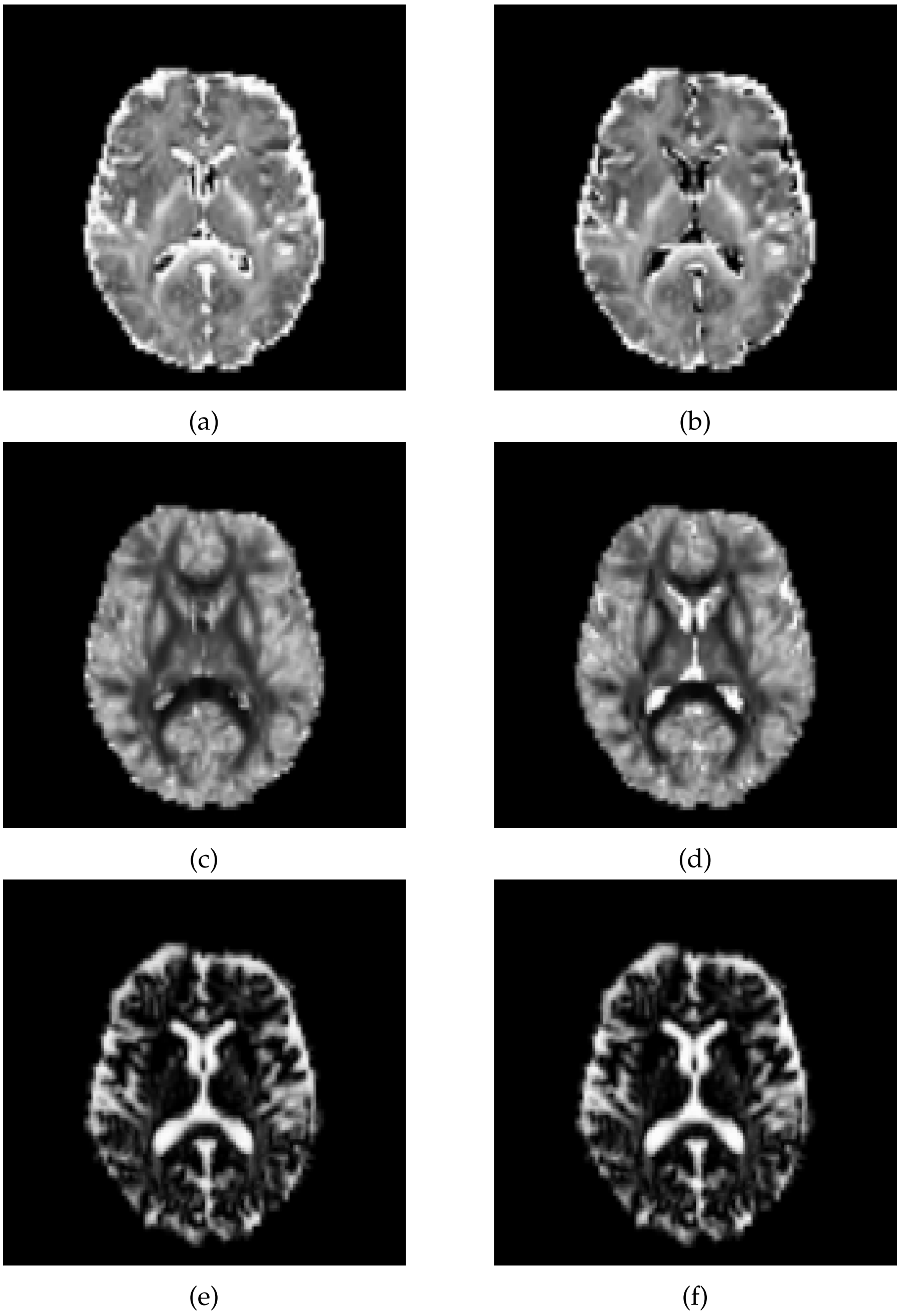

Figure 44: Examples of the 32nd axial slice of NODDI model-derived indices of one healthy subject, computed by using both the original and the AMICO toolboxes: (a), (c) and (e) are, respectively, v_{ic}, *ODI*, and v_{iso} maps computed using the original NODDI toolbox (Zhang et al., 2012), while (b), (d) and (f) are, respectively, v_{ic}, *ODI*, and v_{iso} maps calculated using AMICO toolbox (Daducci et al., 2015).

model-derived indices by means of convex optimization, i.e., AMICO toolbox, is much faster (7.9 ± 0.6, mean ± standard deviation, minutes for each subject) than using the original toolbox (176.9 ± 17.3 minutes for each subject), proposed by Zhang and colleagues (Zhang et al., 2012). It is important to underline that these preliminary results were obtained by working on two different platforms; the NODDI model computation using the original toolbox has been performed on a high performance platform, using 16 of 32 cores available, but it showed worse performances in terms of computation time.

TBSS

Fig. 45 graphically shows the results of TBSS analysis on v_{ic}, OD and v_{iso} indices. In the majority of voxels belonging to the skeleton, the AMICO toolbox seems to underestimate the values of v_{ic}, OD and v_{iso}, compared to the values obtained with the original toolbox (corrected p-value < 0.05).

WHOLE BRAIN VOXEL-WISE STATISTICAL ANALYSIS

The results of the whole brain voxel-wise within-subjects analysis confirms the TBSS results. The values assumed by the majority of the voxels of the v_{ic} map calculated using the original toolbox are significantly higher than those obtained with the AMICO toolbox (Fig. 46a). The OD and v_{iso} maps show a different behaviour of the two toolboxes, according to the different brain tissues. Both the OD and v_{iso} maps obtained with the original toolbox have higher values than those calculated with the AMICO toolbox in the voxels belonging mainly to GM and WM (Fig. 46c and 46e), while the result is opposite in the voxels contained in the CSF of the ventricles (Fig. 46d and 46f).

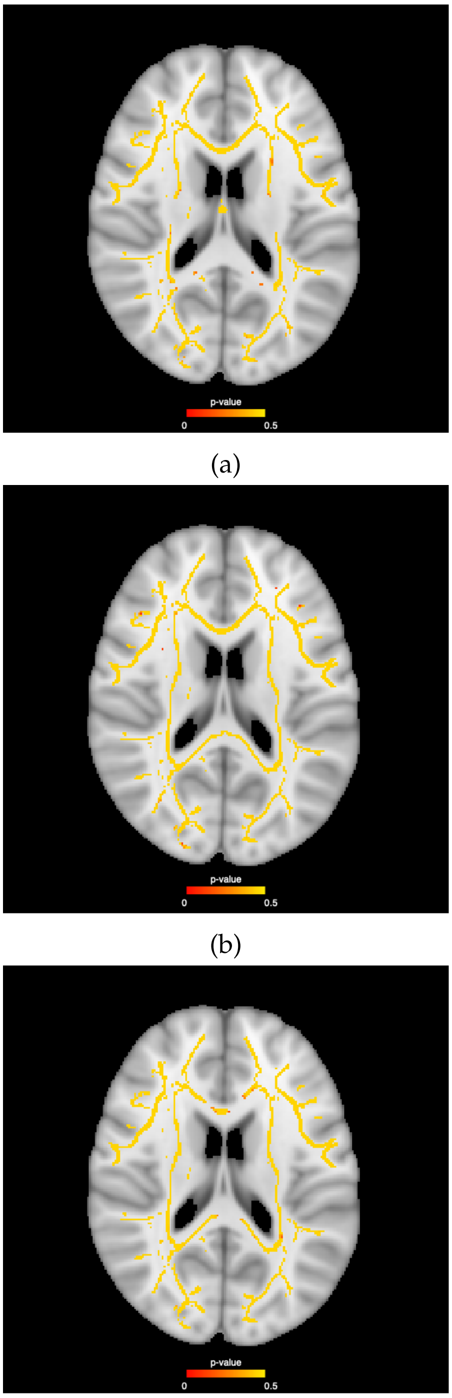

(a)

(b)

(c)

Figure 45: Within-subjects TBSS analysis at anatomic level Z = 90 (Z coordinate in Montreal Neurological Institute standard space), between NODDI and AMICO toolbox results [(a) for v_{ic} map, (b) for *OD* map and (c) for v_{iso} map]. Red-yellow identifies the WM tracts showing a significant (p value < 0.05 corrected, threshold-free cluster enhancement) difference between results obtained with NODDI and AMICO toolbox. This difference is positive for each voxel belonging to the skeleton (i.e. AMICO maps underestimate the corresponding maps calculated using the original NODDI toolbox)

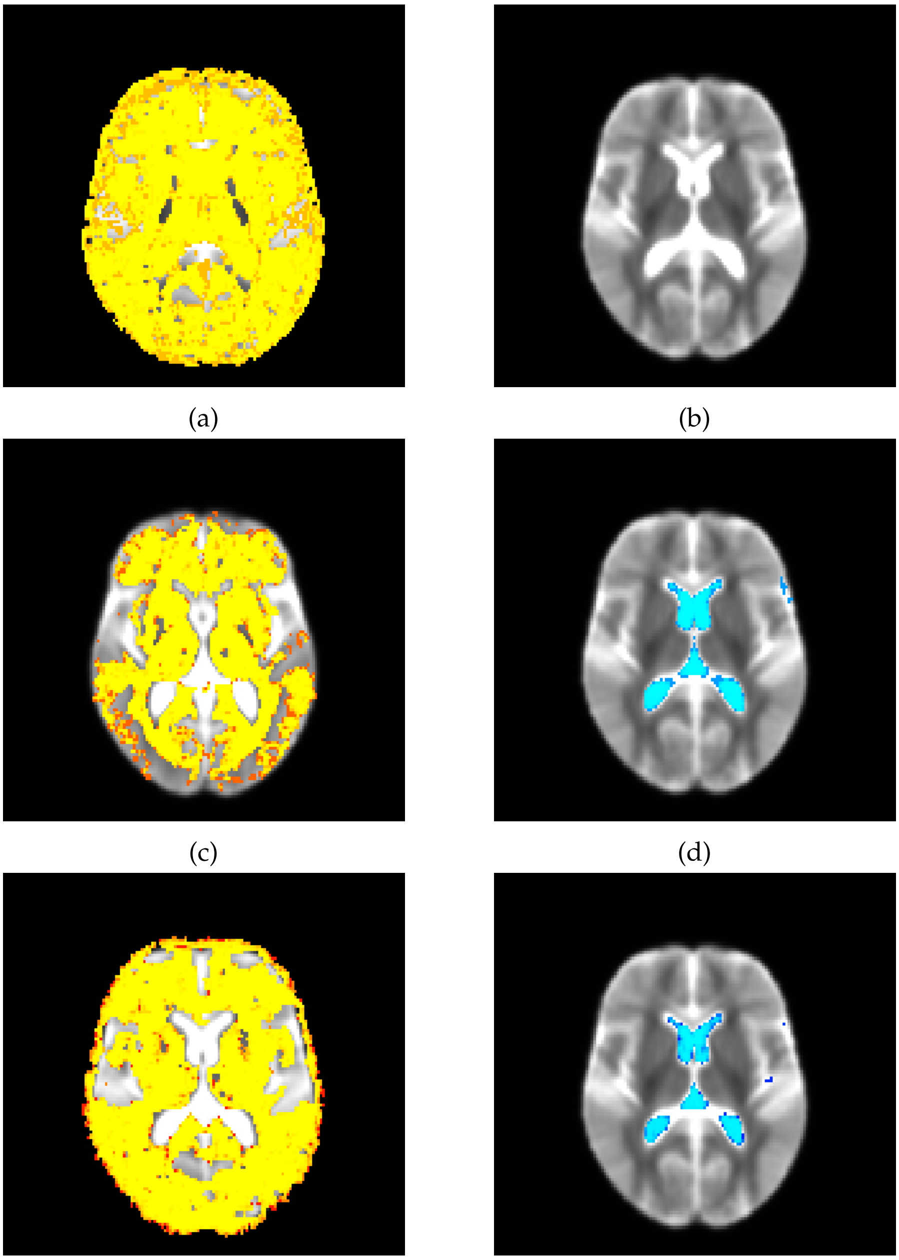

(a) (b)

(c) (d)

(e) (f)

Figure 46: Example of within-subjects whole-brain analysis at 20th axial slice. The colored voxels identify a significant (corrected p-value < 0.05, threshold-free cluster enhancement) difference between results obtained by the original and the AMICO toolboxrs. Yellow voxels represent significant higher values of (a) v_{ic}, (c) OD and (e) $\mathrm{v}_{\mathrm{iso}}$ indices, computed with the original toolbox as compared to those obtained with AMICO toolbox, while light-blue voxels represent lower values of (b) v_{ic}, (d) OD and (f) $\mathrm{v}_{\mathrm{iso}}$ maps, computed with the original toolbox as compared to those obtained with AMICO toolbox.

CONCLUSIONS

In this thesis, we showed that the selection of the interval of the fractal scaling window of the brain in MRI may be critical in the FD estimation. Our approach allows to determine the automated fractal scaling window in which each brain structure actually manifests fractal properties. In particular, we have proposed two new fractal descriptors: the mfs and Mfs, in additon to the FD computed with the automatically selected fractal scaling window. Using our method, we have demonstrated that the FD is a useful marker of morphological complexity changes occurred during brain development and normal aging. To this purpose, we employed a large population of healthy subjects belonging to several datasets, using different scanners at several magnetic field intensities. In addition, we proved that the FD appears a candidate marker able to assess brain changes due to various neurological diseases. For example, in a study regarding patients with SCA2, the brain complexity measured by FD of the cerebellar cortical GM and WM, as well as of the cerebral cortex, is reduced in SCA2 patients as compared to a healthy controls group. Furthermore, using a machine learning approach with standard and advanced neuroimaging features, the FD was found to be a consistent feature in predicting cognitive decline in patients with SVD and MCI, that can complement standard imaging and clinical features.

For the first time, we have also investigated the fractal properties of the brain imaged at ultra-high magnetic field (7T). The structural complexity of the cerebral GM seems to manifest fractal properties also below the spatial scale of 1 mm, suggesting that the human brain may be more complex than what we are able to observe with clinical MRI scanners. Future studies investigating this phenomenon in larger datasets at ultra-high field will be extremely warranted.

During my Ph.D. program, we were also interested in the analysis of brain complexity in diffusion-MRI images. Firstly, we have studied the conventional DWI morphological measures (DTI-, DKI-, NODDI-derived indices) and, in this thesis, we have proposed for the first time the investigation of the fractal properties of skeletons derived from DTI analysis, performed in two different samples of patients with neurological diseases. The fractal properties of the skeleton, which preserves the topology of the general structure, complement those of the general structure derived from T1-weighted images, altough different FD results have been obtained investigating DTI-derived skeletons or T1-weighted images. In structural MRI (T1-weighting- and diffusion-MRI), the combination of conventional morphological indices with these new fractal desriptors may be fundamental for an accurate description of the morphological changes and alterations that characterize brain development, normal aging, and also neurological diseases.

In conclusion the FD, mfs and Mfs computed with the automated selection of the fractal scaling window, are candidate biomarkers to detect subtle morphological changes of the brain during development, normal aging and also in neurological diseases.

BIBLIOGRAPHY

Abbott, A. (2010). "Healthy prions protect nerves." *Nature*.

Ad-Dab'bagh, Y., Singh, V., Robbins, S., Lerch, J.P., Lyttelton, O.C., Fombonne, E., and Evans, A. (2005). "Native-Space Cortical Thickness Measurement And The Absence of Correlation to Cerebral Volume." In: *11th Annual OHBM Meeting*.

Ahmadlou, M., Adeli, H., and Adeli, A. (2010). "Fractality and a wavelet-chaos-neural network methodology for EEG-based diagnosis of autistic spectrum disorder." *Journal of clinical neurophysiology: official publication of the American Electroencephalographic Society* 27 5, pp. 328–33.

Ahmadlou, M., Adeli, H., and Adeli, A. (2011). "Fractality and a wavelet-chaos-methodology for EEG-based diagnosis of Alzheimer disease." *Alzheimer disease and associated disorders* 25 1, pp. 85–92.

Alexander, D.C., Cristinacce, P.L.H., Hall, M.G., Moore, E.A., Ptito, M., Parker, G.J.M., and Dyrby, T.B. (2010). "Orientationally invariant indices of axon diameter and density from diffusion MRI." *NeuroImage* 52, pp. 1374–1389.

Andrews-Hanna, J.R., Snyder, A.Z., Vincent, J.L., Lustig, C., Head, D., Raichle, M.E., and Buckner, R.L. (2007). "Disruption of Large-Scale Brain Systems in Advanced Aging." *Neuron* 56, pp. 924–935.

Armstrong, E. and Falk, D., eds. (1982). *Primate brain evolution Methods and concepts*. Plenum Press New York and London.

Assaf, Y. and Basser, P.J. (2005). "Composite hindered and restricted model of diffusion (CHARMED) MR imaging of the human brain." *NeuroImage* 27, pp. 48–58.

Assaf, Y., Freidlin, R.Z., Rohde, G.K., and Basser, P.J. (2004). "New modeling and experimental framework to characterize hindered and restricted water diffusion in brain white matter." *Magnetic resonance in medicine* 52 5, pp. 965–78.

Auburger, G.W. (2012). "Spinocerebellar ataxia type 2." *Handb Clin Neurol* 103, pp. 423–36.

Avnir, D., Biham, O., Lidar, D.A., and Malcai, O. (1998). "Is the Geometry of Nature Fractal." In: *Science*.

Bach, M., Laun, F.B., Leemans, A., Tax, C.M., Biessels, G.J., Stieltjes, B., and Maier-Hein, K.H. (2014). "Methodological considerations on tract-based spatial statistics (TBSS)." *Neuroimage* 100, pp. 358–69.

Bakkour, A., Morris, J.C., Wolk, D.A., and Dickerson, B.C. (2013). "The effects of aging and Alzheimer's disease on cerebral cortical anatomy: Specificity and differential relationships with cognition." *NeuroImage* 76, pp. 332–344.

Baldarcara, L. et al. (2015). “Consensus paper: radiological biomarkers of cerebellar diseases.” *Cerebellum* 14.2, pp. 175–96.

Barnsley, M.F. (1988). *Fractals Everywhere*. Dover Publications.

Basser, P.J. (1995). “Inferring microstructural features and the physiological state of tissues from diffusion-weighted images.” *NMR in biomedicine* 8 7-8, pp. 333–44.

Basser, P.J. and Jones, D.K. (2002). “Diffusion-tensor MRI: theory, experimental design and data analysis - a technical review.” *NMR Biomed*.

Behrens, T.E., Woolrich, M.W., Jenkinson, M., Johansen-Berg, H., Nunes, R.G., Clare, S., Matthews, P.M., Brady, J.M., and Smith, S.M. (2003). “Characterization and propagation of uncertainty in diffusion-weighted MR imaging.” *Magn Reson Med* 50.5, pp. 1077–88.

Blanton, R.E., Levitt, J.G., Thompson, P.M., Narr, K.L., Capetillo-Cunliffe, L., Nobel, A., Singerman, J.D., McCracken, J.T., and Toga, A.W. (2001). “Mapping cortical asymmetry and complexity patterns in normal children.” *Psychiatry Research: Neuroimaging* 107.1, pp. 29 –43.

Bourne, R.M., Panagiotaki, E., Bongers, A., Sved, P.D., Watson, G., and Alexander, D.C. (2014). “Information theoretic ranking of four models of diffusion attenuation in fresh and fixed prostate tissue ex vivo.” *Magnetic resonance in medicine* 72 5, pp. 1418–26.

Breiman, L. and Spector, P.C. (1992). “Submodel Selection and Evaluation in Regression. The X-Random Case.” *International Statistical Review*.

Brenneis, C., Bosch, S.M., Schocke, M., Wenning, G.K., and Poewe, W. (2003). “Atrophy pattern in SCA2 determined by voxel-based morphometry.” *Neuroreport* 14.14, pp. 1799–802.

Brown, R. (1928). “A brief account of microscopical observations made in the months of June, July, and August, 1827,on the particles contained in the pollen of plants; and on the general existence of active molecules in organic and inorganic bodies.” *Phil Mag*.

Bullmore, E., Brammer, M., Harvey, I., Persaud, R., Murray, R., and Ron, M. (1994). “Fractal analysis of the boundary between white matter and cerebral cortex in magnetic resonance images: a controlled study of schizophrenic and maniac-depressive patients.” *Psychological Medicine* 24, pp. 771–781.

Bullmore, E.T., Fadili, J.M., Maxim, V., Sendur, L., and Breakspear, M. (2004). “Wavelets and functional magnetic resonance imaging of the human brain.” *NeuroImage* 23, s234–s249.

Caffarra, P., Vezzadini, G., Dieci, F., Zonato, F., and Venneri, A. (2002a). “Rey-Osterrieth complex figure: normative values in an Italian population sample.” *Neurol Sci* 22.6, pp. 443–7.

Caffarra, P., Vezzadini, G., Dieci, F., Zonato, F., and Venneri, A. (2002b). “Una versione abbreviata del test di Stroop. Dati normativi nella popolazione italiana.” *Nuova Rivista di Neurologia* 12.4, pp. 111–115.

Cao, M. et al. (2014). “Topological organization of the human brain functional connectome across the lifespan.” *Developmental Cognitive Neuroscience* 7, pp. 76–93.

Caserta, F., Eldred, W.D., Fernández, E., Hausman, R.E., and Stanley, H.M.E. (1995). “Determination of fractal dimension of physiologically characterized neurons in two and three dimensions.” *Journal of Neuroscience Methods* 56, pp. 133–144.

Cassot, F., Lauwers, F., Fouard, C., Prohaska, S., and Lauwers-Cances, V. (2006). “A novel three-dimensional computer-assisted method for a quantitative study of microvascular networks of the human cerebral cortex.” *Microcirculation* 13 1, pp. 1–18.

Cauter, S.V. et al. (2012). “Gliomas: diffusion kurtosis MR imaging in grading.” *Radiology* 263 2, pp. 492–501.

Cavallari, M., Falco, T., Frontali, M., Romano, S., Bagnato, F., and Orzi, F. (Apr. 2011). “Fractal Analysis Reveals Reduced Complexity of Retinal Vessels in CADASIL.” *Plos ONE* 6.4, pp. 1–4.

Caviness, V.S., Kennedy, D.N., Richelme, C., Rademacher, J., and Filipek, P.A. (1996). “The human brain age 7-11 years: a volumetric analysis based on magnetic resonance images.” *Cerebral cortex* 6 5, pp. 726–36.

Chabriat, H., Joutel, A., Dichgans, M., Tournier-Lasserve, E., and Bousser, M.-G. (2009). “CADASIL.” *The Lancet Neurology* 8.7, pp. 643 –653.

Chang, L.-C., Jones, D.K., and Pierpaoli, C. (2005). “RESTORE: robust estimation of tensors by outlier rejection.” *Magnetic resonance in medicine* 53 5, pp. 1088–95.

Cheung, C.Y. lui, Tay, W.T., Ikram, M.K., Ong, Y.T., Silva, D.A.D., Chow, K.Y., and Wong, T.Y. (2013). “Retinal Microvascular Changes and Risk of Stroke.” *Stroke* 44.9, pp. 2402–2408.

Cole, M. and Cole, S.R. (1993). *The development of children.* 2nd. New York, NY, US: Scientific American Books.

Conti, S., Bonazzi, S., Laiacona, M., Masina, M., and Coralli, M.V. (2015). “Montreal Cognitive Assessment (MoCA)-Italian version: regression based norms and equivalent scores.” *Neurol Sci* 36.2, pp. 209–14.

Cook, M., Free, S., Manford, M., Fish, R., Shorvon, S., and Stevens, J. (Nov. 1995). “Fractal Description of Cerebral Cortical Patterns in Frontal Lobe Epilepsy.” *European neurology* 35, pp. 327–35.

Cook, P.A., Bai, Y., Nedjati-Gilani, S., Seunarine, K.K., Hall, M.G., Parker, G.J., and Alexander, D.C. (2006). “Camino: Open-Source Diffusion-MRI Reconstruction and Processing.” In: *14th Scientific*

Meeting of the International Society for Magnetic Resonance in Medicine, p. 2759.

Courchesne, E., Chisum, H.J., Townsend, J., Cowles, A, Covington, J., Egaas, B, Harwood, M., Hinds, S., and Press, G.A. (2000). “Normal brain development and aging: quantitative analysis at in vivo MR imaging in healthy volunteers.” *Radiology* 216 3, pp. 672–82.

Coutu, J.-P., Chen, J.J., Rosas, H.D., and Salat, D.H. (2014). “Non-Gaussian water diffusion in aging white matter.” *Neurobiology of Aging* 35, pp. 1412–1421.

Cowan, W.M., Fawcett, J.W., O’leary, D.D., and Stanfield, B.B. (1984). “Regressive events in neurogenesis.” *Science* 225 4668, pp. 1258–65.

Crank, J. (1975). *The Mathematics of Diffusion*. 2nd. Oxford University Press.

D’Agata, F. et al. (2011). “Linking coordinative and executive dysfunctions to atrophy in spinocerebellar ataxia 2 patients.” *Brain Struct Funct* 216.3, pp. 275–88.

Daducci, A., Canales-Rodríguez, E.J., Zhang, H., Dyrby, T.B., Alexander, D.C., and Thiran, J.-P. (2015). “Accelerated Microstructure Imaging via Convex Optimization (AMICO) from diffusion MRI data.” *NeuroImage* 105, pp. 32–44.

Dale, A.M. and Sereno, M.I. (1993). “Improved Localizadon of Cortical Activity by Combining EEG and MEG with MRI Cortical Surface Reconstruction: A Linear Approach.” *Journal of Cognitive Neuroscience* 5, pp. 162–176.

Dale, A., Fischl, B., and Sereno, M.I. (1999). “Cortical Surface-Based Analysis: I. Segmentation and Surface Reconstruction.” *NeuroImage* 9.2, pp. 179 –194.

Dangeti, P. (2017). *Statistics for machine learning : build supervised, unsupervised, and reinforcement learning models using both Python and R*. Birmingham, UK: Packt Publishing, 2017.

De Guio, F. et al. (2016). “Reproducibility and variability of quantitative magnetic resonance imaging markers in cerebral small vessel disease.” *J Cereb Blood Flow Metab* 36.8, pp. 1319–37.

De Luca, A., Arrigoni, F., Romaniello, R., Triulzi, F.M., Peruzzo, D., and Bertoldo, A. (2016). “Automatic localization of cerebral cortical malformations using fractal analysis.” *Physics in medicine and biology* 61 16, pp. 6025–40.

Decarlo, L.T. (1997). “On the meaning and use of kurtosis.” *Psychol. Meth.*

Della Nave, R. et al. (2008a). “Brain structural damage in spinocerebellar ataxia type 2. A voxel-based morphometry study.” *Mov Disord* 23.6, pp. 899–903.

Della Nave, R. et al. (2008b). “Brain white matter damage in SCA1 and SCA2. An in vivo study using voxel-based morphometry, histogram analysis of mean diffusivity and tract-based spatial statistics." *Neuroimage* 43.1, pp. 10–9.

Della Nave, R., Ginestroni, A., Diciotti, S., Salvatore, E., Soricelli, A., and Mascalchi, M. (2011). "Axial diffusivity is increased in the degenerating superior cerebellar peduncles of Friedreich's ataxia." *Neuroradiology* 53.5, pp. 367–72.

Della Sala, S., Laiacona, M., Spinnler, H., and Ubezio, C. (1992). "A cancellation test: its reliability in assessing attentional deficits in Alzheimer's disease." *Psychol Med* 22.4, pp. 885–901.

Desikan, R.S. et al. (2006). "An automated labeling system for subdividing the human cerebral cortex on MRI scans into gyral based regions of interest." *NeuroImage* 31.3, pp. 968 –980.

Di Ieva, A., Esteban, F.J., Grizzi, F., Klonowski, W., and Martin-Landrove, M. (2015). "Fractals in the neurosciences, Part II: clinical applications and future perspectives." *The Neuroscientist : a review journal bringing neurobiology, neurology and psychiatry* 21 1, pp. 30–43.

Diciotti, S., Ciulli, S., Mascalchi, M., Giannelli, M., and Toschi, N. (2013). "The "peeking" effect in supervised feature selection on diffusion tensor imaging data." *AJNR. American journal of neuroradiology* 34 9, E107.

Dickerson, B.C., Feczko, E., Augustinack, J., Pacheco, J., and Buckner, R.L. (2009). "Differential effects of aging and Alzheimer's disease on medial temporal lobe cortical thickness and surface area." *Neurobiology of Aging* 30, pp. 432–440.

Dollinger, J.W., Metzler, R., and Nonnenmacher, T.F. (1998). "Bi-asymptotic fractals: Fractals between lower and upper bounds." *Journal of Physics A: Mathematical and General* 31.16, pp. 3839–3847.

Doob, J.L. (1942). "The Brownian Movement and Stochastic Equations." *Math.*

Doubal, F.N., MacGillivray, T.J., Patton, N., Dhillon, B., Dennis, M., and Wardlaw, J.M. (2010). "Fractal analysis of retinal vessels suggests that a distinct vasculopathy causes lacunar stroke." *Neurology* 74 14, pp. 1102–7.

Driscoll, I., Davatzikos, C., An, Y.S., Wu, X., Shen, D., Kraut, M.J., and Resnick, S.M. (2009). "Longitudinal pattern of regional brain volume change differentiates normal aging from MCI." *Neurology* 72 22, pp. 1906–13.

Durr, A. et al. (1995). "Autosomal dominant cerebellar ataxia type I in Martinique (French West Indies). Clinical and neuropathological analysis of 53 patients from three unrelated SCA2 families." *Brain* 118 (Pt 6), pp. 1573–81.

Einstein, A. (1905). "Ueber die von der molekularkinetischen Theorieder waerme gefordete Bewegung von in ruhenden Fluessigkeitensuspendierten Teilchen." *Ann Physik.*

Einstein, A. (1926). *Investigations on the Theory of the Brownian Movement.* New York: Dover Publications, Inc.

Elderkin-Thompson, V., Kumar, A., Mintz, J., Boone, K., Bahng, E., and Lavretsky, H. (2004). "Executive dysfunction and visuospatial ability among depressed elders in a community setting." *Arch Clin Neuropsychol* 19.5, pp. 597–611.

Ennis, D.B. and Kindlmann, G. (2006). "Orthogonal tensor invariants and the analysis of diffusion tensor magnetic resonance images." *Magn Reson Med* 55.1, pp. 136–46.

Esteban, F.J., Sepulcre, J., Mendizabal, N.V. del, Goni, J., Navas, J., Miras, J.R. de, Bejarano, B., Masdeu, J.C., and Villoslada, P. (2007). "Fractal dimension and white matter changes in multiple sclerosis." *NeuroImage* 36, pp. 543–549.

Esteban, F.J., Sepulcre, J., Miras, J.R. de, Navas, J., and Villoslada, P. (2009). "Fractal dimension analysis of grey matter in multiple sclerosis." *Journal of the Neurological Sciences* 282, pp. 67–71.

Estrada, R., Galarraga, J., Orozco, G., Nodarse, A., and Auburger, G. (1999). "Spinocerebellar ataxia 2 (SCA2): morphometric analyses in 11 autopsies." *Acta Neuropathol* 97.3, pp. 306–10.

Falangola, M., Jensen, J.H., Babb, J.S., Hu, C., Castellanos, F.X., Martino, A.D., Ferris, S.H., and Helpern, J.A. (2008). "Age-related non-Gaussian diffusion patterns in the prefrontal brain." *Journal of magnetic resonance imaging : JMRI* 28 6, pp. 1345–50.

Falangola, M., Jensen, J.H., Tabesh, A., Hu, C., Deardorff, R.L., Babb, J.S., Ferris, S.H., and Helpern, J.A. (2013). "Non-Gaussian diffusion MRI assessment of brain microstructure in mild cognitive impairment and Alzheimer's disease." *Magnetic resonance imaging* 31 6, pp. 840–6.

Falconer, K. (2004). *Fractal Geometry, Mathematical Foundations and Applications*. Second Edition. Wiley.

Farahibozorg, S.R., Hashemi-Golpayegani, S.M., and Ashburner, J. (2015). "Age- and Sex-Related Variations in the Brain White Matter Fractal Dimension Throughout Adulthood: An MRI Study." *Clinical Neuroradiology*.

Feder, J. (1988). *Fractals*. Springer US.

Fick, A. (1855a). "Concerns diffusion and concentration gradient." *AnnPhys Lpz*.

Fick, A. (1855b). "Ueber diffusion." *Ann Phys*.

Fieremans, E. et al. (2013). "Novel white matter tract integrity metrics sensitive to Alzheimer disease progression." *AJNR. American journal of neuroradiology* 34 11, pp. 2105–12.

Filla, A., DeMichele, G., Caruso, G., Marconi, R., and Campanella, G. (1990). "Genetic data and natural history of Friedreich's disease: a study of 80 Italian patients." *J Neurol* 237.6, pp. 345–51.

Fischl, B. (2012). "Freesurfer." *Neuroimage* 62.2, pp. 774–781.

Fischl, B., Liu, A., and Dale, A.M. (2001). "Automated manifold surgery: constructing geometrically accurate and topologically correct models of the human cerebral cortex." *IEEE Medical Imaging* 20.1, pp. 70–80.

Fischl, B. et al. (2002). "Whole brain segmentation: automated labeling of neuroanatomical structures in the human brain." *Neuron* 33, pp. 341–355.

Fischl, B. and Dale, A.M. (2000). "Measuring the thickness of the human cerebral cortex from magnetic resonance images." *Proceedings of the National Academy of Sciences of the United States of America* 97.20, pp. 11050–11055.

Fischl, B., Sereno, M.I., and Dale, A.M. (1999a). "Cortical Surface-Based Analysis: II: Inflation, Flattening, and a Surface-Based Coordinate System." *NeuroImage* 9, pp. 195–207.

Fischl, B., Sereno, M.I., and Dale, A. (1999b). "Cortical Surface-Based Analysis: II: Inflation, Flattening, and a Surface-Based Coordinate System." *NeuroImage* 9.2, pp. 195 –207.

Fischl, B. et al. (2004a). "Automatically Parcellating the Human Cerebral Cortex." *Cerebral Cortex* 14.1, pp. 11–22.

Fischl, B., Salat, D.H., Kouwe, A.J. van der, Makris, N., Ségonne, F., Quinn, B.T., and Dale, A.M. (2004b). "Sequence-independent segmentation of magnetic resonance images." *NeuroImage* 23.Supplement 1, S69 –S84.

Fjell, A.M. et al. (2009). "High consistency of regional cortical thinning in aging across multiple samples." *Cerebral cortex* 19 9, pp. 2001–12.

Fjell, A.M., McEvoy, L.K., Holland, D., Dale, A.M., and Initiative, A.D.N. (2014). "What is normal in normal aging? Effects of aging, amyloid and Alzheimer's disease on the cerebral cortex and the hippocampus." *Progress in Neurobiology* 117, pp. 20–40.

Focke, N.K., Diederich, C., Helms, G., Nitsche, M.A., Lerche, H., and Paulus, W. (2014). "Idiopathic-generalized epilepsy shows profound white matter diffusion-tensor imaging alterations." *Human brain mapping* 35 7, pp. 3332–42.

Foroutan-poor, K., Dutilleul, P., and Smith, D.L. (1999). "Advances in the implementation of the box-counting method of fractal dimension estimation." *Applied Mathematiccs and Computation* 105, pp. 195–210.

Fotenos, A.F., Snyder, A.Z., Girton, L.E., Morris, J.C., and Buckner, R.L. (2005). "Normative estimates of cross-sectional and longitudinal brain volume decline in aging and AD." *Neurology* 64 6, pp. 1032–9.

Free, S.L., Sisodiya, S.M., Cook, M.J., Fish, D.R., and Shorvon, S.D. (1996). "Three-Dimensional Fractal Analysis of the White Matter

Surface from Magnetic Resonance Images of the Human Brain." *Cerebral Cortex* 6, pp. 830–836.

Freeman, R.Q., Giovannetti, T., Lamar, M., Cloud, B.S., Stern, R.A., Kaplan, E., and Libon, D.J. (2000). "Visuoconstructional problems in dementia: contribution of executive systems functions." *Neuropsychology* 14.3, pp. 415–26.

Gandolfi, A. (2008). *Formicai, imperi, cervelli: introduzione alla scienza della complessità*. Bollati Boringhieri.

Gauthier, S. et al. (2006). "Mild cognitive impairment." *Lancet* 367.9518, pp. 1262–70.

Giannelli, M., Marzi, C., Mascalchi, M., Diciotti, S., and Tessa, C. (2019). "Can Trace-Weighted Images Be Used to Estimate Diffusional Kurtosis Imaging–Derived Indices of Non-Gaussian Water Diffusion in Head and Neck Cancer?" *American Journal of Neuroradiology*.

Giannelli, M. and Toschi, N. (2016). "On the use of trace-weighted images in body diffusional kurtosis imaging." *Magnetic resonance imaging* 34 4, pp. 502–7.

Giannelli, M., Marzi, C., Mascalchi, M., Diciotti, S., and Tessa, C. (2017). "Toward a Standardized Approach to Estimate Kurtosis in Body Applications of a Non-Gaussian Diffusion Kurtosis Imaging Model of Water Diffusion." *Radiology* 285.1, 329—331.

Giovagnoli, A.R., Del Pesce, M., Mascheroni, S., Simoncelli, M., Laiacona, M., and Capitani, E. (1996). "Trail making test: normative values from 287 normal adult controls." *Ital J Neurol Sci* 17.4, pp. 305–9.

Giuffrida, S., Saponara, R., Restivo, D.A., Trovato Salinaro, A., Tomarchio, L., Pugliares, P., Fabbri, G., and Maccagnano, C. (1999). "Supratentorial atrophy in spinocerebellar ataxia type 2: MRI study of 20 patients." *J Neurol* 246.5, pp. 383–8.

Goel, G. et al. (2011). "Gray matter volume deficits in spinocerebellar ataxia: an optimized voxel based morphometric study." *Parkinsonism Relat Disord* 17.7, pp. 521–7.

Goldberger, A.L. (1997). "Fractal variability versus pathologic periodicity: complexity loss and stereotypy in disease." *Perspectives in biology and medicine* 40 4, pp. 543–61.

Goldberger, A.L., Amaral, L.A.N., Hausdorff, J.M., Ivanov, P.C., Peng, C.K., and Stanley, H.E. (2002a). "Fractal dynamics in physiology: alterations with disease and aging." *Proceedings of the National Academy of Sciences of the United States of America* 99 Suppl 1, pp. 2466–72.

Goldberger, A.L., Peng, C.-K., and Lipsitz, L.A. (2002b). "What is physiologic complexity and how does it change with aging and disease?" *Neurobiology of Aging* 23, pp. 23–26.

Goni, J. et al. (2013). "Robust estimation of fractal measures for characterizing the structural complexity of the human brain: Optimization and reproducibility." *NeuroImage* 83, pp. 646–657.

Good, C.D., Johnsrude, I.S., Ashburner, J., Henson, R.N.A., Fristen, K.J., and Frackowiak, R.S. (2001). "A voxel-based morphometric study of ageing in 465 normal adult human brains." *5th IEEE EMBS International Summer School on Biomedical Imaging, 2002.* 16 pp.–.

Gorgolewski, K.J. et al. (2014). "A high resolution 7-Tesla resting-state fMRI test-retest dataset with cognitive and physiological measures." *Scientific Data.*

Gould, S.J. (1971). "Geometric Similarity in Allometric Growth: A Contribution to the Problem of Scaling in the Evolution of Size." *The American Naturalist* 105.942, pp. 113–136.

Goveas, J., O'Dwyer, L., Mascalchi, M., Cosottini, M., Diciotti, S., De Santis, S., Passamonti, L., Tessa, C., Toschi, N., and Giannelli, M. (2015). "Diffusion-MRI in neurodegenerative disorders." *Magn Reson Imaging* 33.7, pp. 853–76.

Gregoire, S.M., Chaudhary, U.J., Brown, M.M., Yousry, T., Kallis, C., Jäger, H.R., and Werring, D.J. (2009). "The Microbleed Anatomical Rating Scale (MARS): reliability of a tool to map brain microbleeds." *Neurology* 73 21, pp. 1759–66.

Gronenschild, E.H.B.M., Habets, P., Jacobs, H.I.L., Mengelers, R., Rozendaal, N., van Os, J., and Marcelis, M. (June 2012). "The Effects of FreeSurfer Version, Workstation Type, and Macintosh Operating System Version on Anatomical Volume and Cortical Thickness Measurements." *PLOS ONE* 7.6, pp. 1–13.

Ha, T.H., Yoon, U., Lee, K.J., Shin, Y.W., and Kwon, J.S. (2005). "Fractal dimension of cerebral cortical surface in schizophrenia and obsessive–compulsive disorder." *Neuroscience Letters* 384, pp. 172–176.

Han, X. et al. (2006). "Reliability of MRI-derived measurements of human cerebral cortical thickness: The effects of field strength, scanner upgrade and manufacturer." *NeuroImage* 32.1, pp. 180–194.

Hastie, T.J., Tibshirani, R., and Friedman, J.H. (2013). "The Elements of Statistical Learning: Data Mining, Inference, and Prediction, 2nd Edition." In: *Springer Series in Statistics*.

Hedman, A.M., Haren, N.E.M.V., Schnack, H.G., Kahn, R.S., and Pol, H.E.H. (2012). "Human brain changes across the life span: a review of 56 longitudinal magnetic resonance imaging studies." *Human brain mapping* 33 8, pp. 1987–2002.

Heinzer, S., Krucker, T., Stampanoni, M., Abela, R., Meyer, E.P., Schuler, A., Schneider, P., and Müller, R. (2006). "Hierarchical microimaging for multiscale analysis of large vascular networks." *NeuroImage* 32.2, pp. 626 –636.

Herman, P., Kocsis, L., and Eke, A. (2001). "Fractal branching pattern in the pial vasculature in the rat." *Journal of cerebral blood flow and metabolism : official journal of the International Society of Cerebral Blood Flow and Metabolism* 21 6, pp. 741–53.

Hernandez-Castillo, C.R., Galvez, V., Mercadillo, R., Diaz, R., Campos-Romo, A., and Fernandez-Ruiz, J. (2015). "Extensive White Matter Alterations and Its Correlations with Ataxia Severity in SCA 2 Patients." *PLoS One* 10.8, e0135449.

Hernandez-Castillo, C.R., Vaca-Palomares, I, Gálvez, V., Campos-Romo, A., Díaz, R., and Fernández-Ruiz, J. (2016). "Cognitive Deficits Correlate with White Matter Deterioration in Spinocerebellar Ataxia Type 2." *Journal of the International Neuropsychological Society : JINS* 22 4, pp. 486–91.

Hofman, M.A. (1989). "On the evolution and geometry of the brain in mammals." *Progress in Neurobiology* 32.2, pp. 137 –158.

Hofman, M.A. (1991). "The fractal geometry of convoluted brains." *Journal fur Hirnforschung* 32 1, pp. 103–11.

Hogstrom, L.J., Westlye, L.T., Walhovd, K.B., and Fjell, A.M. (2013). "The structure of the cerebral cortex across adult life: age-related patterns of surface area, thickness, and gyrification." *Cerebral cortex* 23 11, pp. 2521–30.

Huang, S.R., Wu, Y.T., Jao, C.W., Soong, B.W., Lirng, J.F., Wu, H.M., and Wang, P.S. (2017). "CAG repeat length does not associate with the rate of cerebellar degeneration in spinocerebellar ataxia type 3." *Neuroimage Clin* 13, pp. 97–105.

Huang, Y., Chen, X., Zhang, Z., Yan, L., Pan, D.D., Liang, C., and Liu, Z. (2015). "MRI quantification of non-Gaussian water diffusion in normal human kidney: a diffusional kurtosis imaging study." *NMR in biomedicine* 28 2, pp. 154–61.

Hui, E.S., Cheung, M.M., Qi, L., and Wu, E.X. (2008). "Towards better MR characterization of neural tissues using directional diffusion kurtosis analysis." *NeuroImage* 42, pp. 122–134.

Huttenlocher, P. (1979). "Synaptic density in human frontal cortex - developmental changes and effects of aging." *Brain research* 163 2, pp. 195–205.

Hutton, C., Draganski, B., Ashburner, J., and Weiskopf, N. (2009). "A comparison between voxel-based cortical thickness and voxel-based morphometry in normal aging." *NeuroImage*.

Ibanez, L., Schroeder, W., Ng, L., and Cates, J. (2003). *The ITK software guide*. Kitware.

Iima, M., Yano, K., Kataoka, M., Umehana, M., Murata, K, Kanao, S., Togashi, K., and Bihan, D.L. (2015). "Quantitative non-Gaussian diffusion and intravoxel incoherent motion magnetic resonance imaging: differentiation of malignant and benign breast lesions." *Investigative radiology* 50 4, pp. 205–11.

Im, K., Lee, J.M., Yoon, U., Shin, Y.W., Hong, S.B., Kim, I.Y., Kwon, J.S., and Kim, S.I. (2006). "Fractal dimension in human cortical surface: multiple regression analysis with cortical thickness, sulcal depth, and folding area." *Human brain mapping* 27 12, pp. 994–1003.

Jacobs, B., Driscoll, L, and Schall, M. (1997). "Life-span dendritic and spine changes in areas 10 and 18 of human cortex: a quantitative Golgi study." *The Journal of comparative neurology* 386 4, pp. 661–80.

Jambor, I., Merisaari, H., Aronen, H.J., Järvinen, J., Saunavaara, J., Kauko, T., Borra, R., and Pesola, M. (2014). "Optimization of b-value distribution for biexponential diffusion-weighted MR imaging of normal prostate." *Journal of magnetic resonance imaging : JMRI* 39 5, pp. 1213–22.

Jelinek, H.F. and Fernández, E. (1998). "Neurons and fractals: how reliable and useful are calculations of fractal dimensions?" *Journal of Neuroscience Methods* 81, pp. 9–18.

Jelinek, H., Elston, N, and Zietsch, B. (2005). "Fractal analysis: Pitfalls and revelations in neuroscience." English. In: *Fractals in Biology and Medicine*. Ed. by G. Losa, D Merlini, T. Nonnenmacher, and E. Weibel. Vol. 4. Mathematics and Biosciences in Interaction. Birkhauser, pp. 85–94.

Jenkinson, M., Bannister, P., Brady, M., and Smith, S. (2002). "Improved optimization for the robust and accurate linear registration and motion correction of brain images." *Neuroimage* 17.2, pp. 825–41.

Jensen, J.H. and Helpern, J.A. (2010). "MRI quantification of non-Gaussian water diffusion by kurtosis analysis." *NMR in biomedicine* 23 7, pp. 698–710.

Jensen, J.H., Helpern, J.A., Ramani, A., Lu, H., and Kaczynski, K. (2005). "Diffusional kurtosis imaging: the quantification of non-gaussian water diffusion by means of magnetic resonance imaging." *Magnetic resonance in medicine* 53 6, pp. 1432–40.

Jerison, H. (1982). "Primate Brain Evolution." In: ed. by F.D. Armstrong E. Springer, Boston, MA. Chap. Allometry, Brain Size, Cortical Surface, and Convolutedness.

Jernigan, T.L., Trauner, D.A., Hesselink, J.R., and Tallal, P. (1991). "Maturation of human cerebrum observed in vivo during adolescence." *Brain : a journal of neurology* 114 (Pt 5), pp. 2037–49.

Jernigan, T.L., Archibald, S.L., Fennema-Notestine, C., Gamst, A.C., and Hesselink, J.R. (2001). "Effects of age on tissues and regions of the cerebrum and cerebellum." *Neurobiology of Aging* 22, pp. 581–594.

Jespersen, S.N., Bjarkam, C.R., Nyengaard, J.R., Chakravarty, M.M., Hansen, B., Vosegaard, T., Østergaard, L., Yablonskiy, D.A., Nielsen, N.C., and Vestergaard-Poulsen, P. (2010). "Neurite density from magnetic resonance diffusion measurements at ultrahigh field: Comparison with light microscopy and electron microscopy." *NeuroImage* 49, pp. 205–216.

Jespersen, S.N., Leigland, L.A., Cornea, A., and Kroenke, C.D. (2012). "Determination of Axonal and Dendritic Orientation Distributions Within the Developing Cerebral Cortex by Diffusion Tensor Imaging." *IEEE Transactions on Medical Imaging* 31, pp. 16–32.

Jeurissen, B., Leemans, A., Tournier, J., and Sijbers, J. (2010). "Estimating the number offiber orientations in diffusion MR voxels: a constrained spherical deconvolutionstudy." In: *Proc. ISMRM, p. 573*.

Jiang, H., DeBuc, D.C., Rundek, T., Lam, B.L., Wright, C.B., Shen, M., Tao, A.X., and Wang, J. (2013). "Automated segmentation and fractal analysis of high-resolution non-invasive capillary perfusion maps of the human retina." *Microvascular research* 89, pp. 172–5.

Jiang, R., Du, F.Z., He, C., Gu, M., Ke, Z.W., and Li, J.H. (2014). "The Value of Diffusion Tensor Imaging in Differentiating High-Grade Gliomas from Brain Metastases: A Systematic Review and Meta-Analysis." *PloS one*.

Johansen-Berg, H. and Behrens, T.E., eds. (2009). *Diffusion mri: from quantitative measurement to in-vivo neuroanatomy*. Elsevier.

Jokinen, H. et al. (2012). "Brain atrophy accelerates cognitive decline in cerebral small vessel disease: the LADIS study." *Neurology* 78.22, pp. 1785–92.

Jones, D.K. (2004). "The effect of gradient sampling schemes on measures derived from diffusion tensor MRI: a Monte Carlo study." *Magnetic resonance in medicine* 51 4, pp. 807–15.

Jones, D.K., ed. (2011). *Diffusion MRI: Theory, Methods, and Applications*. OXFORD University Press.

Jovicich, J. et al. (2006). "Reliability in multi-site structural MRI studies: Effects of gradient non-linearity correction on phantom and human data." *NeuroImage* 30.2, pp. 436 –443.

Kaden, E., Knösche, T.R., and Anwander, A. (2007). "Parametric spherical deconvolution: Inferring anatomical connectivity using diffusion MR imaging." *NeuroImage* 37, pp. 474–488.

Kalmanti, E. and Maris, T.G. (2007). "Fractal Dimension as an Index of Brain Cortical Changes Throughout Life." *In Vivo* 21.4, pp. 641–646.

Katsaloulis, P., Verganelakis, D.A., and Provata, A. (2009). "Fractal dimension and lacunarity of tractography images of the human brain." *Fractals* 17.2, pp. 181–189.

Kawasaki, R., Azemin, M.Z.C., Kumar, D.M.K., Tan, A.G., Liew, G., Wong, T.Y., Mitchell, P.L., and Wang, J.J. (2011). "Fractal dimension of the retinal vasculature and risk of stroke: a nested case-control study." *Neurology* 76 20, pp. 1766–7.

Keihaninejad, S., Ryan, N.S., Malone, I.B., Modat, M., Cash, D., Ridgway, G.R., Zhang, H., Fox, N.C., and Ourselin, S. (2012). "The importance of group-wise registration in tract based spatial statistics study of neurodegeneration: a simulation study in Alzheimer's disease." *PLoS One* 7.11, e45996.

Kemper, T.L. (1994). "Clinical neurology of aging." In: ed. by M.L. Albert and J.E. Knoefel. New York, NY, US: Oxford University Press. Chap. Neuroanatomical and neuropathological changes during aging and dementia. Pp. 3 –67.

Kindlmann, G.L., Ennis, D.B., Whitaker, R.T., and Westin, C.-F. (2007). "Diffusion Tensor Analysis With Invariant Gradients and Rotation Tangents." *IEEE Transactions on Medical Imaging* 26, pp. 1483–1499.

King, R.D., George, A.T., Jeon, T., Hynan, L.S., Youn, T.S., Kennedy, D.N., Dickerson, B., and the Alzheimer's Disease Neuroimaging Initiative (2009). "Characterization of Atrophic Changes in the Cerebral Cortex Using Fractal Dimensional Analysis." *Brain Imaging and Behavior* 3, pp. 154–166.

King, R.D., Brown, B., Hwang, M., Jeon, T., and George, A.T. (2010). "Fractal dimension analysis of the cortical ribbon in mild Alzheimer's disease." *NeuroImage* 53, pp. 471–479.

Kiselev, V.G., Hahn, K.R., and Auer, D.P. (2003). "Is the brain cortex a fractal?" *NeuroImage* 20, pp. 1765–1774.

Krohn, S., Froeling, M., Leemans, A., Ostwald, D., Villoslada, P., Finke, C., and Esteban, F.J. (2019). "Evaluation of the 3D fractal dimension as a marker of structural brain complexity in multiple-acquisition MRI." *Human brain mapping* 40 11, pp. 3299–3320.

Kuperberg, G.R. et al. (2003). "Regionally localized thinning of the cerebral cortex in Schizophrenia." *Archives of General Psychiatry* 60, pp. 878–888.

Landini, G. and Rigaut, J.P. (1997). "A method for estimating the dimension of asymptotic fractal sets." *Bioimaging* 5.2, pp. 65–70.

Landini, G., Murray, P.I., and Misson, G.P. (1995). "Local Connected Fractal Dimensions and Lacunarity Analysis of 60° Fluorescein Angiograms." *Investigative Ophtalmology & Visual Science* 36.13, pp. 2749–2755.

Landman, B.A. et al. (2011). "Multi-parametric neuroimaging reproducibility: A 3-T resource study." *NeuroImage* 54, pp. 2854–2866.

Lauwers, F., Cassot, F., Lauwers-Cances, V., Puwanarajah, P., and Duvernoy, H. (2008). "Morphometry of the human cerebral cortex microcirculation: General characteristics and space-related profiles." *NeuroImage* 39, pp. 936–948.

Lazzeroni, L.C. and Ray, A. (2012). "The cost of large numbers of hypothesis tests on power, effect size and sample size." *Molecular Psychiatry*.

Le Bihan, D. and Warach, S.J., eds. (1995). *Diffusion and perfusion magnetic resonance imaging : applications to functional MRI*. Raven Press, New York.

Lee, C.-Y., Tabesh, A., Benitez, A., Helpern, J.A., Jensen, J.H., and Bonilha, L. (2013). "Microstructural integrity of early- versus late-myelinating white matter tracts in medial temporal lobe epilepsy." *Epilepsia* 54.10, pp. 1801–1809.

Leemans, A. and Jones, D.K. (2009). "The B-matrix must be rotated when correcting for subject motion in DTI data." *Magn Reson Med* 61.6, pp. 1336–49.

Lemaître, H., Crivello, F., Grassiot, B., Alpérovitch, A., Tzourio, C., and Mazoyer, B. (2005). "Age- and sex-related effects on the neuroanatomy of healthy elderly." *NeuroImage* 26, pp. 900–911.

Lemm, S., Blankertz, B., Dickhaus, T., and Müller, K.R. (2011). "Introduction to machine learning for brain imaging." *NeuroImage* 56, pp. 387–399.

Li, Y.C. and Huang, Y.A. (2014). "Fractal analysis of spontaneous fluctuations of the BOLD signal in the human brain networks." *Journal of Magnetic Resonance Imaging* 39.5, pp. 1118–1125.

Linn, J., Halpin, A., Demaerel, P., Ruhland, J., Giese, A., Dichgans, M., Buchem, M.A. van, Bruckmann, H., and Greenberg, S.M. (2010). "Prevalence of superficial siderosis in patients with cerebral amyloid angiopathy." *Neurology* 74 17, pp. 1346–50.

Lipschutz, M.M. (1969). *Schaum's outline of theory and problems of differential geometry*.

Liu, J.Z., Zhang, L., and Yue, G.H. (2003). "Fractal dimension in human cerebellum measured by magnetic resonance imaging." *Biophysical journal* 85 6, pp. 4041–6.

Losa, G.A. and Nonnenmacher, T.F. (1996). "Self-similarity and fractal irregularity in pathologic tissues." *Modern pathology : an official journal of the United States and Canadian Academy of Pathology, Inc* 9 3, pp. 174–82.

Losa, G. (Jan. 2002). "Fractal morphometry of cell complexity." *Rivista di biologia* 95, pp. 239–58.

Losa, G. (July 2014). "The Fractal Geometry of Life." *Rivista di biologia* 102, pp. 29–59.

Lu, H., Jensen, J.H., Ramani, A., and Helpern, J.A. (2006). "Three-dimensional characterization of non-gaussian water diffusion in humans using diffusion kurtosis imaging." *NMR in biomedicine* 19 2, pp. 236–47.

Madan, C.R. and Kensinger, E.A. (2016). "Cortical complexity as a measure of age-related brain atrophy." *NeuroImage* 134, pp. 617–629.

Madhyastha, T., Merillat, S., Hirsiger, S., Bezzola, L., Liem, F., Grabowski, T., and Jancke, L. (2014). "Longitudinal reliability of tract-based spatial statistics in diffusion tensor imaging." *Hum Brain Mapp* 35.9, pp. 4544–55.

Majumdar, S. and Prasad, R.R. (1988). "The fractal dimension of cerebral surfaces using magnetic resonance images." In:

Mandelbrot, B.B. (1982). *The Fractal Geometry of Nature*. W. H. Freeman and Company.

Mandelbrot, B.B. (1998). "Is Nature Fractal?" *Science* 279.5352, pp. 783–783.

Mandelli, M.L., De Simone, T., Minati, L., Bruzzone, M.G., Mariotti, C., Fancellu, R., Savoiardo, M., and Grisoli, M. (2007). "Diffusion tensor imaging of spinocerebellar ataxias types 1 and 2." *AJNR Am J Neuroradiol* 28.10, pp. 1996–2000.

Marques, J.P., Kober, T., Krueger, G., Zwaag, W. van der, Moortele, P.-F. van de, and Gruetter, R. (2010). "MP2RAGE, a self bias-field corrected sequence for improved segmentation and T1-mapping at high field." *NeuroImage* 49, pp. 1271–1281.

Marzi, C. and Diciotti, S. (2018). "The fractal dimension of the brain at ultra-high field MRI." Abstract presented at Sixth National Conference of Bioingeneering, Milano, Italy.

Marzi, C. and Diciotti, S. (2019). "The Structural Complexity of the Cortical Gray Matter at Ultra-High Field MRI." Abstract presented at XXV Annual International Conference of the Organization of Human Brain Mapping, Rome, Italy.

Marzi, C., Ciulli, S., Giannelli, M., Ginestroni, A., Tessa, C., Mascalchi, M., and Diciotti, S. (2018a). "Structural Complexity of the Cerebellum and Cerebral Cortex is Reduced in Spinocerebellar Ataxia Type 2." *Journal of neuroimaging : official journal of the American Society of Neuroimaging* 28 6, pp. 688–693.

Marzi, S., Minosse, S., Vidiri, A., Piludu, F., and Giannelli, M. (2018b). "Diffusional kurtosis imaging in head and neck cancer: On the use of trace-weighted images to estimate indices of non-Gaussian water diffusion." *Medical physics* 45 12, pp. 5411–5419.

Mascalchi, M. and Vella, A. (2012). "Magnetic resonance and nuclear medicine imaging in ataxias." *Handb Clin Neurol* 103, pp. 85–110.

Mascalchi, M. et al. (2014). "Progression of brain atrophy in spinocerebellar ataxia type 2: a longitudinal tensor-based morphometry study." *PLoS One* 9.2, e89410.

Mascalchi, M. et al. (2015). "Progression of microstructural damage in spinocerebellar ataxia type 2: a longitudinal DTI study." *AJNR Am J Neuroradiol* 36.6, pp. 1096–101.

Mascalchi, M. et al. (2016). "Regional Cerebral Disease Progression in Friedreich's Ataxia: A Longitudinal Diffusion Tensor Imaging Study." *J Neuroimaging* 26.2, pp. 197–200.

Mascalchi, M. et al. (2018). "Histogram analysis of DTI-derived indices reveals pontocerebellar degeneration and its progression in SCA2." *PloS one*.

Mazziotta, J. et al. (2001a). "A probabilistic atlas and reference system for the human brain: International Consortium for Brain Mapping (ICBM)." *Philosophical transactions of the Royal Society of London. Series B, Biological sciences* 356 1412, pp. 1293–322.

Mazziotta, J.C. et al. (2001b). "Application of Information Technology: A Four-Dimensional Probabilistic Atlas of the Human Brain." *Journal of the American Medical Informatics Association : JAMIA* 8 5, pp. 401–30.

Mazzoni, L.N., Lucarini, S., Chiti, S., Busoni, S., Gori, C., and Menchi, I. (2014). "Diffusion-weighted signal models in healthy and cancerous peripheral prostate tissues: comparison of outcomes obtained at different b-values." *Journal of magnetic resonance imaging : JMRI* 39 3, pp. 512–8.

McCarthy, C.S., Ramprashad, A., Thompson, C., Botti, J.A., Coman, I.L., and Kates, W.R. (2015). "A comparison of FreeSurfer-generated data with and without manual intervention." *Front Neurosci* 9, p. 379.

Mercadillo, R.E., Galvez, V., Diaz, R., Hernandez-Castillo, C.R., Campos-Romo, A., Boll, M.C., Pasaye, E.H., and Fernandez-Ruiz, J. (2014). "Parahippocampal gray matter alterations in Spinocerebellar Ataxia Type 2 identified by voxel based morphometry." *J Neurol Sci* 347.1-2, pp. 50–8.

Michail, E., Chouvarda, I., and Maglaveras, N. (2010). "Benzodiazepine administration effect on EEG Fractal Dimension: results and causalities." *2010 Annual International Conference of the IEEE Engineering in Medicine and Biology*, pp. 2350–2353.

Michallek, F. and Dewey, M. (2013). "Fractal analysis in radiological and nuclear medicine perfusion imaging: a systematic review." *European Radiology* 24, pp. 60–69.

Minnich, B., Bartel, H., and Lametschwandtner, A. (2001). "Quantitative microvascular corrosion casting by 2D- and 3D-morphometry." *Italian journal of anatomy and embryology = Archivio italiano di anatomia ed embriologia* 106 2 Suppl 1, pp. 213–20.

Mori, S. (2007). *Introduction to Diffusion Tensor Imaging*. Elsevier.

Moritani, T., Ekholm, S., and Westesson, P.-L., eds. (2009). *Diffusion-Weighted MR Imaging of the Brain*. Springer.

Morse, D.R., Lawton, J.A., Dodson, M.M., and Williamson, M.H. (1985). "Fractal dimension of vegetation and the distribution of arthropod body lengths." *Nature* 314, pp. 731–733.

Mueller, A. and Guido, S. (2017). *Introduction to Machine Learning with Python: A Guide for Data Scientists,* O'Reilly Media, Inc.

Mustafa, N., Ahearn, T.S., Waiter, G.D., Murray, A.D., and Roger T. Staff, L.J.W. abd (2012). "Brain structural complexity and life course cognitive change." *NeuroImage* 61, pp. 694–701.

Narr, K., Bilder, R.M., Kim, S., Thompson, P.M., and Toga, A.W. (2004). "Abnormal gyral complexity in first-episode schizophrenia." *Biological Psychiatry* 55, pp. 859–867.

Nasreddine, Z.S., Phillips, N.A., Bedirian, V., Charbonneau, S., Whitehead, V., Collin, I., Cummings, J.L., and Chertkow, H. (2005). "The Montreal Cognitive Assessment, MoCA: a brief screening tool for mild cognitive impairment." *J Am Geriatr Soc* 53.4, pp. 695–9.

Nenadic, I., Yotter, R.A., Sauer, H., and Gaser, C. (2014). "Cortical surface complexity in frontal and temporal areas varies across subgroups of schizophrenia." *Human brain mapping* 35 4, pp. 1691–9.

Ni, J., Auriel, E., Martínez-Ramírez, S., Keil, B., Reed, A.K., Fotiadis, P., Gurol, E.M., Greenberg, S.M., and Viswanathan, A (2015). "Cortical localization of microbleeds in cerebral amyloid angiopathy: an ultra high-field 7T MRI study." *Journal of Alzheimer's disease : JAD* 43 4, pp. 1325–30.

Nichols, T.E. and Holmes, A.P. (2002). "Nonparametric permutation tests for functional neuroimaging: a primer with examples." *Hum Brain Mapp* 15.1, pp. 1–25.

Nocentini, U., Giordano, A., Di Vincenzo, S., Panella, M., and Pasqualetti, P. (2006). "The Symbol Digit Modalities Test - Oral version: Italian normative data." *Funct Neurol* 21.2, pp. 93–6.

Nogueira, L., Brandão, S., Matos, E., Nunes, R.G., Loureiro, J., Ramos, I., and Ferreira, H.A. (2014). "Application of the diffusion kurtosis model for the study of breast lesions." *European Radiology* 24, pp. 1197–1203.

Noirhomme, Q., Lesenfants, D., Gomez, F., Soddu, A., Schrouff, J., Garraux, G., Luxen, A., Phillips, C., and Laureys, S. (2014). "Biased binomial assessment of cross-validated estimation of classification accuracies illustrated in diagnosis predictions." *NeuroImage: Clinical.*

Nooner, K.B. et al. (2012). "The NKI-Rockland Sample: A Model for Accelerating the Pace of Discovery Science in Psychiatry." *Front. Neurosci.*

O'Brien, J.T. et al. (2003). "Vascular cognitive impairment." *Lancet Neurol* 2.2, pp. 89–98.

Odish, O.F. et al. (2015). “Microstructural brain abnormalities in Huntington’s disease: A two-year follow-up.” *Hum Brain Mapp* 36.6, pp. 2061–74.

Olejarczyk, E. (2007). “Application of fractal dimension method of functional MRI time-series to limbic dysregulation in anxiety study.” In: *2007 29th Annual International Conference of the IEEE Engineering in Medicine and Biology Society*, pp. 3408–3410.

Olivito, G., Lupo, M., Iacobacci, C., Clausi, S., Romano, S., Masciullo, M., Molinari, M., Cercignani, M., Bozzali, M., and Leggio, M. (2017). “Microstructural MRI basis of the cognitive functions in patients with spinocerebellar ataxia type 2.” *Neuroscience* 366, pp. 44–53.

Ong, Y.T., Silva, D.A.D., Cheung, C.Y.L., Chang, H.M., Chen, C.P., Wong, M.C., Wong, T.Y., and Ikram, M.K. (2013). “Microvascular structure and network in the retina of patients with ischemic stroke.” *Stroke* 44 8, pp. 2121–7.

Pakkenberg, B., Pelvig, D.P., Marner, L., Bundgaard, M.J., and Regeur, L. (2003). “Aging and the human neocortex.” *Experimental Gerontology* 38, pp. 95–99.

Panagiotaki, E., Schneider, T., Siow, B., Hall, M.G., Lythgoe, M.F., and Alexander, D.C. (2012). “Compartment models of the diffusion MR signal in brain white matter: A taxonomy and comparison.” *NeuroImage* 59, pp. 2241–2254.

Panerai, R.B. (2009). “Complexity of the human cerebral circulation.” *Philosophical transactions. Series A, Mathematical, physical, and engineering sciences* 367 1892, pp. 1319–36.

Panizzon, M.S. et al. (2009). “Distinct genetic influences on cortical surface area and cortical thickness.” *Cerebral cortex* 19 11, pp. 2728–35.

Pantoni, L. (2010). “Cerebral small vessel disease: from pathogenesis and clinical characteristics to therapeutic challenges.” *Lancet Neurol* 9.7, pp. 689–701.

Pantoni, L., Marzi, C., Poggesi, A., Giorgio, A., De Stefano, N., Mascalchi, M., Inzitari, D., Salvadori, E., and Diciotti, S. (2019). “Fractal dimension of cerebral white matter: A consistent feature for prediction of the cognitive performance in patients with small vessel disease and mild cognitive impairment.” *NeuroImage: Clinical*.

Pardoe, H.R., Hiess, R.K., and Kuzniecky, R. (2016). “Motion and morphometry in clinical and nonclinical populations.” *NeuroImage* 135, pp. 177 –185.

Pareyson, D., Gellera, C., Castellotti, B., Antonelli, A., Riggio, M.C., Mazzucchelli, F., Girotti, F., Pietrini, V., Mariotti, C., and Di Donato, S. (1999). “Clinical and molecular studies of 73 Italian families with autosomal dominant cerebellar ataxia type

I: SCA1 and SCA2 are the most common genotypes." *J Neurol* 246.5, pp. 389–93.

Pasi, M. et al. (2015). "White matter microstructural damage in small vessel disease is associated with Montreal cognitive assessment but not with mini mental state examination performances: vascular mild cognitive impairment Tuscany study." *Stroke* 46.1, pp. 262–4.

Pellecchia, M.T. et al. (2011). "Progression of striatal and extrastriatal degeneration in multiple system atrophy: a longitudinal diffusion-weighted MR study." *Mov Disord* 26.7, pp. 1303–9.

Peng, F., Wang, L., Geng, Z., Zhu, Q., and Song, Z. (2016). "A Cross-Sectional Voxel-Based Morphometric Study of Age- and Sex-Related Changes in Gray Matter Volume in the Normal Aging Brain." *Journal of computer assisted tomography* 40 2, pp. 307–15.

Pentang, G., Lanzman, R.S., Heusch, P., Müller-Lutz, A., Blondin, D.W., Antoch, G., and Wittsack, H.J. (2014). "Diffusion kurtosis imaging of the human kidney: a feasibility study." *Magnetic resonance imaging* 32 5, pp. 413–20.

Peters, A.H., Morrison, J.H., Rosene, D.L., and Hyman, B.T. (1998). "Feature article: are neurons lost from the primate cerebral cortex during normal aging?" *Cerebral cortex* 8 4, pp. 295–300.

Pfefferbaum, A., Mathalon, D.H., Sullivan, E.V., Rawles, J., Zipursky, R.B., and Lim, K.O. (1994). "A quantitative magnetic resonance imaging study of changes in brain morphology from infancy to late adulthood." *Archives of neurology* 51 9, pp. 874–87.

Pienaar, R., Fischl, B., Caviness, V.S., Makris, N., and Grant, P.E. (2008). "A methodology for analyzing curvature in the developing brain from preterm to adult." *International journal of imaging systems and technology* 18 1, pp. 42–68.

Poggesi, A. et al. (2012). "Risk and Determinants of Dementia in Patients with Mild Cognitive Impairment and Brain Subcortical Vascular Changes: A Study of Clinical, Neuroimaging, and Biological Markers-The VMCI-Tuscany Study: Rationale, Design, and Methodology." *Int J Alzheimers Dis* 2012, p. 608013.

Poot, D.H.J., Dekker, A.J. den, Achten, E., Verhoye, M., and Sijbers, J. (2010). "Optimal Experimental Design for Diffusion Kurtosis Imaging." *IEEE Transactions on Medical Imaging* 29, pp. 819–829.

Quentin, M., Blondin, D.W., Klasen, J., Lanzman, R.S., Miese, F.-R., Arsov, C., Albers, P., Antoch, G., and Wittsack, H.J. (2012). "Comparison of different mathematical models of diffusion-weighted prostate MR imaging." *Magnetic resonance imaging* 30 10, pp. 1468–74.

Quentin, M., Pentang, G., Schimmoeller, L., Kott, O., Müller-Lutz, A., Blondin, D.W., Arsov, C., Hiester, A., Rabenalt, R., and Wittsack, H.J. (2014). "Feasibility of diffusional kurtosis tensor imaging in prostate MRI for the assessment of prostate cancer: preliminary results." *Magnetic resonance imaging* 32 7, pp. 880–5.

Raab, P., Hattingen, E., Franz, K., Zanella, F.E., and Lanfermann, H. (2010). "Cerebral gliomas: diffusional kurtosis imaging analysis of microstructural differences." *Radiology* 254 3, pp. 876–81.

Rajagopalan, V., Liu, Z., Allexandre, D., Zhang, L., Wang, X.-F., Pioro, E.P., and Yue, G.H. (Sept. 2013). "Brain White Matter Shape Changes in Amyotrophic Lateral Sclerosis (ALS): A Fractal Dimension Study." *PLOS ONE* 8.9, pp. 1–11.

Rajagopalan, V., Das, A., Zhang, L., Hillary, F., Wylie, G.R., and Yue, G.H. (2019). "Fractal dimension brain morphometry: a novel approach to quantify white matter in traumatic brain injury." *Brain Imaging and Behavior*, pp. 1–11.

Raz, N. and Rodrigue, K.M. (2006). "Differential aging of the brain: Patterns, cognitive correlates and modifiers." *Neuroscience & Biobehavioral Reviews* 30, pp. 730–748.

Raz, N., Gunning, F.M., Head, D., Dupuis, J., McQuain, J, Briggs, S.D., Loken, W.J., Thornton, A.E., and Acker, J.D. (1997). "Selective aging of the human cerebral cortex observed in vivo: differential vulnerability of the prefrontal gray matter." *Cerebral cortex* 7 3, pp. 268–82.

Reetz, K. et al. (2013). "Genotype-specific patterns of atrophy progression are more sensitive than clinical decline in SCA1, SCA3 and SCA6." *Brain* 136.Pt 3, pp. 905–17.

Reginold, W., Lang, A.E., Marras, C., Heyn, C., Alharbi, M., and Mikulis, D.J. (2014). "Longitudinal quantitative MRI in multiple system atrophy and progressive supranuclear palsy." *Parkinsonism Relat Disord* 20.2, pp. 222–5.

Reiss, A.L., Abrams, M.T., Singer, H.S., Ross, J.L., and Denckla, M.B. (1996). "Brain development, gender and IQ in children. A volumetric imaging study." *Brain : a journal of neurology* 119 (Pt 5), pp. 1763–74.

Rensma, S.P., Sloten, T.T. van, Launer, L.J., and Stehouwer, C.D.A. (2018). "Cerebral small vessel disease and risk of incident stroke, dementia and depression, and all-cause mortality: A systematic review and meta-analysis." *Neurosci Biobehav Rev* 90, pp. 164–173.

Rettmann, M.E., Kraut, M.A., Prince, J.L., and Resnick, S.M. (2006). "Cross-sectional and longitudinal analyses of anatomical sulcal changes associated with aging." *Cerebral cortex* 16 11, pp. 1584–94.

Reuter, M., Rosas, H.D., and Fischl, B. (2010). "Highly Accurate Inverse Consistent Registration: A Robust Approach." *NeuroImage* 53.4, pp. 1181–1196.

Reuter, M., Schmansky, N.J., Rosas, H.D., and Fischl, B. (2012). "Within-Subject Template Estimation for Unbiased Longitudinal Image Analysis." *NeuroImage* 61.4, pp. 1402–1418.

Reuter, M., Tisdall, M.D., Qureshi, A., Buckner, R.L., Kouwe, A.J. van der, and Fischl, B. (2015). "Head motion during MRI acquisition reduces gray matter volume and thickness estimates." *NeuroImage* 107, pp. 107 –115.

Rosas, H.D., Liu, A.K., Hersch, S., Glessner, M., Ferrante, R.J., Salat, D.H., van der Kouwe, A., Jenkins, B.G., Dale, A.M., and Fischl, B. (2002). "Regional and progressive thinning of the cortical ribbon in Huntington's disease." *Neurology* 58.5, pp. 695–701.

Rosas, H.D. et al. (2010). "Altered white matter microstructure in the corpus callosum in Huntington's disease: implications for cortical "disconnection"." *Neuroimage* 49.4, pp. 2995–3004.

Rosenkrantz, A.B., Sigmund, E.E., Winnick, A.M., Niver, B.E., Spieler, B.M., Morgan, G.R., and Hajdu, C.H. (2012a). "Assessment of hepatocellular carcinoma using apparent diffusion coefficient and diffusion kurtosis indices: preliminary experience in fresh liver explants." *Magnetic resonance imaging* 30 10, pp. 1534–40.

Rosenkrantz, A.B., Sigmund, E.E., Johnson, G., Babb, J.S., Mussi, T.C., Melamed, J., Taneja, S.S., Lee, V.S., and Jensen, J.H. (2012b). "Prostate cancer: feasibility and preliminary experience of a diffusional kurtosis model for detection and assessment of aggressiveness of peripheral zone cancer." *Radiology* 264 1, pp. 126–35.

Rosenkrantz, A.B., Padhani, A.R., Chenevert, T.L., Koh, D.M., De Keyzer, F, Taouli, B., and Le Bihan, D. (2015). "Body diffusion kurtosis imaging: Basic principles, applications, and considerations for clinical practice." *Journal of magnetic resonance imaging : JMRI* 42 5, pp. 1190–202.

Rubin, D., Fekete, T., and Mujica-Parodi, L.R. (May 2013). "Optimizing Complexity Measures for fMRI Data: Algorithm, Artifact, and Sensitivity." *PLOS ONE* 8.5, pp. 1–16.

Russ, J. (1994). *Fractal Surfaces*. New York: Plenum.

Russell, D.A., Hanson, J.D., and Ott, E. (1980). "Dimension of strange Attractors." *Physical Review Letters* 45.14, pp. 1175–1178.

Rybaczuk, M. and Kedzia, A. (1996). "Fractal analysis of adults cerebellum surface NMR observations." *Folia Morphol (Warsz).* 55.4, pp. 431–3.

Rybaczuk, M., Kedzia, A., and Blaszczyk, E. (1996). "Fractal description of cerebellum surface during fetal period." *Folia Morphol. (Praha)* 55, pp. 434–436.

Sagan, H. (1994). *Space-filling Curves*. Springer-Verlag.

Sakai, T. and Miyoshi, K. (2002). "The use of quantitative methods in clinical trials for spinocerebellar ataxia." *Arch Neurol* 59.6, 1044–5; author reply 1045.

Salat, D., Buckner, R., Snyder, A., Greve, D.N., Desikan, R., Busa, E., Morris, J., Dale, A., and Fischl, B. (2004). "Thinning of the cerebral cortex in aging." *Cerebral Cortex* 14, pp. 721–730.

Salvadori, E., Poggesi, A., Pracucci, G., Inzitari, D., Pantoni, L., and VMCI-Tuscany Study Group (2015). "Development and psychometric properties of a neuropsychological battery for mild cognitive impairment with small vessel disease: the VMCI-Tuscany Study." *J Alzheimers Dis* 43.4, pp. 1313–23.

Salvadori, E., Dieci, F., Caffarra, P., and Pantoni, L. (2018). "Qualitative Evaluation of the Immediate Copy of the Rey-Osterrieth Complex Figure: Comparison Between Vascular and Degenerative MCI Patients." *Arch Clin Neuropsychol*.

Sandu, A.L., Rasmussen, I.A., Lundervold, A., Kreuder, F., Neckelmann, G., Hugdahl, K., and Specht, K. (2008). "Fractal dimension analysis of MR images reveals grey matter structure irregularities in schizophrenia." *Computerized medical imaging and graphics : the official journal of the Computerized Medical Imaging Society* 32 2, pp. 150–8.

Sandu, A.L., Izard, E., Specht, K., Beneventi, H., Lundervold, A., and Ystad, M. (2014a). "Post-adolescent developmental changes in cortical complexity." *Behavioral and Brain Functions* 10.1, p. 44.

Sandu, A.L., Staff, R.T., McNeil, C.J., Mustafa, N., Ahearn, T.S., Whalley, L.J., and Murray, A.D. (2014b). "Structural brain complexity and cognitive decline in late life — A longitudinal study in the Aberdeen 1936 Birth Cohort." *NeuroImage* 100, pp. 558–563.

Sato, K., Sugawara, K., Narita, Y., and Namura, I. (1996). "Consideration of the method of image diagnosis with respect to frontal lobe atrophy." In: *1996 IEEE Nuclear Science Symposium. Conference Record*. Vol. 2, 1467–1471 vol.2.

Savalia, N.K., Agres, P.F., Chan, M.Y., Feczko, E.J., Kennedy, K.M., and Wig, G.S. (2017). "Motion-related artifacts in structural brain images revealed with independent estimates of in-scanner head motion." *Human Brain Mapping* 38.1, pp. 472–492.

Scahill, R.I., Frost, C., Jenkins, R., Whitwell, J.L., Rossor, M., and Fox, N.C. (2003). "A longitudinal study of brain volume changes in normal aging using serial registered magnetic resonance imaging." *Archives of neurology* 60 7, pp. 989–94.

Schmitz-Hubsch, T. et al. (2008). "Spinocerebellar ataxia types 1, 2, 3, and 6: disease severity and nonataxia symptoms." *Neurology* 71.13, pp. 982–9.

Schwarz, C.G. et al. (2016). "A large-scale comparison of cortical thickness and volume methods for measuring Alzheimer's disease severity." *NeuroImage: Clinical*.

Segonne, F., Dale, A.M., Busa, E., Glessner, M., Salat, D., Hahn, H.K., and Fischl, B. (2004). "A hybrid approach to the skull stripping problem in MRI." *NeuroImage* 22.3, pp. 1060 –1075.

Segonne, F., Pacheco, J., and Fischl, B. (2007). "Geometrically accurate topology-correction of cortical surfaces using nonseparating loops." *IEEE Trans Med Imaging* 26, pp. 518–529.

Seidel, K., Siswanto, S., Brunt, E.R., Dunnen, W. den, Korf, H.W., and Rub, U. (2012). "Brain pathology of spinocerebellar ataxias." *Acta Neuropathol* 124.1, pp. 1–21.

Sheelakumari, R., Venkateswaran, R., Chandran, A., Varghese, T., Zhang, L., Yue, G.H., Mathuranath, P.S., and Kesavadas, C. (2017). "Quantitative analysis of grey matter degeneration in FTD patients using fractal dimension analysis." *Brain Imaging Behav.*

Shin, M.S., Park, S.Y., Park, S.R., Seol, S.H., and Kwon, J.S. (2006). "Clinical and empirical applications of the Rey-Osterrieth Complex Figure Test." *Nat Protoc* 1.2, pp. 892–9.

Shishikura, M. (1998). "The hausdorff dimension of the boundary of the Mandelbrot set and Julia sets." *Annals of Mathematics* 147.2, pp. 225–267.

Skullerud, K. (1985). "Variations in the size of the human brain. Influence of age, sex, body length, body mass index, alcoholism, Alzheimer changes, and cerebral atherosclerosis." *Acta neurologica Scandinavica. Supplementum* 102, pp. 1–94.

Sled, J., Zijdenbos, A., and Evans, A. (1998). "A nonparametric method for automatic correction of intensity nonuniformity in MRI data." *IEEE Trans Med Imaging* 17, pp. 87–97.

Smith, C.D., Chebrolu, H., Wekstein, D.R., Schmitt, F.A., and Markesbery, W.R. (2007). "Age and gender effects on human brain anatomy: A voxel-based morphometric study in healthy elderly." *Neurobiology of Aging* 28, pp. 1075–1087.

Smith, S.M. (2002). "Fast robust automated brain extraction." *Hum Brain Mapp* 17.3, pp. 143–55.

Smith, S.M. and Nichols, T.E. (2009). "Threshold-free cluster enhancement: addressing problems of smoothing, threshold dependence and localisation in cluster inference." *Neuroimage* 44.1, pp. 83–98.

Smith, S.M. et al. (2004). "Advances in functional and structural MR image analysis and implementation as FSL." *Neuroimage* 23 Suppl 1, S208–19.

Smith, S.M. et al. (2006). "Tract-based spatial statistics: voxelwise analysis of multi-subject diffusion data." *Neuroimage* 31.4, pp. 1487–505.

Smith, T.G.J., Lange, G.D., and Marks, W.B. (1996). "Fractal methods and results in cellular morphology - dimensions, lacunarity and multifractals." *Journal of Neuroscience Methods* 69, pp. 123–136.

Sotiropoulos, S., Behrens, T., and Jbabdi, S. (2012). "Ball and rackets: Inferring fiberfanning from diffusion-weight MRI." *NeuroImage* 60.2, 1412–1425.

Squarcina, L., De Luca, A., Bellani, M., Brambilla, P., Tukheimer, F.E., and Bertoldo, A. (2015). "Fractal analysis of MRI data for the characterization of patients with schizophrenia and bipolar disorder." *Physics in Medicine and Biology* 60, pp. 1697–1716.

Stanley, H.E. and Ostrowsky, N., eds. (1986). *On Growth and Form*. Springer Netherlands.

Steens, S.C., Admiraal-Behloul, F., Schaap, J.A., Hoogenraad, F.G., Wheeler-Kingshott, C.A., le Cessie, S., Tofts, P.S., and van Buchem, M.A. (2004). "Reproducibility of brain ADC histograms." *Eur Radiol* 14.3, pp. 425–30.

Sunkin, S.M., Ng, L., Lau, C., Dolbeare, T., Gilbert, T.L., Thompson, C.L., Hawrylycz, M.J., and Dang, C. (2012). "Allen Brain Atlas: an integrated spatio-temporal portal for exploring the central nervous system." *Nucleic Acids Research*.

Suo, S., Chen, X., Wu, L., Zhang, X., Yao, Q., Fan, Y., Wang, H., and Xu, J. (2014). "Non-Gaussian water diffusion kurtosis imaging of prostate cancer." *Magnetic resonance imaging* 32 5, pp. 421–7.

Tabesh, A., Jensen, J.H., Ardekani, B.A., and Helpern, J.A. (2011). "Estimation of tensors and tensor-derived measures in diffusional kurtosis imaging." *Magnetic resonance in medicine* 65 3, pp. 823–36.

Takahashi, T., Murata, T., Narita, K., Hamada, T., Kosaka, H., Omori, M., Takahashi, K., Kimura, H., Yoshida, H., and Wada, Y. (2006). "Multifractal analysis of deep white matter microstructural changes on MRI in relation to early-stage atherosclerosis." *NeuroImage* 32, pp. 1158–1166.

Takahashi, T., Kosaka, H., Murata, T., Omori, M., and Wada, Y. (2009). "Application of a multifractal analysis to study brain white matter abnormalities of schizophrenia on T2-weighted magnetic resonance imaging." *Psychiatry Research: Neuroimaging* 171, pp. 177–188.

Thompson, D.W. (1915). "Galileo and the Principle of Similitudine." *Nature*.

Thompson, D.W. (1942). *On growth and form*. Cambridge at the University Press.

Thompson, P.M., Moussai, J., Zohoori, S, Goldkorn, A., Khan, A.A., Mega, M.S., Small, G.W., Cummings, J.L., and Toga, A.W. (1998). "Cortical variability and asymmetry in normal aging and Alzheimer's disease." *Cerebral cortex* 8 6, pp. 492–509.

Thompson, P.M. et al. (2005). "Abnormal cortical complexity and thickness profiles mapped in Williams syndrome." *The Journal of neuroscience : the official journal of the Society for Neuroscience* 25 16, pp. 4146–58.

Thompson, P.M. et al. (2007). "Tracking Alzheimer's Disease." *Annals of the New York Academy of Sciences* 1097.1, pp. 183–214.

Todd, P. (1984). "THE INTRINSIC GEOMETRY OF BIOLOGICAL SURFACE GROWTH." In: *Mathematical Modelling in Science and Technology*. Ed. by X.J. Avula, R.E. Kalman, A.I. Liapis, and E.Y. Rodin. Pergamon, pp. 733 –738.

Toga, A.W. and Thompson, P.M. (2002). "New approaches in brain morphometry." *The American journal of geriatric psychiatry : official journal of the American Association for Geriatric Psychiatry* 10 1, pp. 13–23.

Trouillas, P. et al. (1997). "International Cooperative Ataxia Rating Scale for pharmacological assessment of the cerebellar syndrome. The Ataxia Neuropharmacology Committee of the World Federation of Neurology." *J Neurol Sci* 145.2, pp. 205–11.

Tustison, N.J. et al. (2014). "Large-scale evaluation of ANTs and FreeSurfer cortical thickness measurements." *NeuroImage* 99, pp. 166–179.

Tălu, S. (2011). "Fractal analysis of normal retinal vascular network." *Oftalmologia (Bucharest, Romania : 1990)* 55.4, 11—16.

Van Essen, D.C., Dierker, D.L., Snyder, A.Z., Raichle, M.E., Reiss, A.L., and Korenberg, J. (2006). "Symmetry of cortical folding abnormalities in Williams syndrome revealed by surface-based analyses." *The Journal of neuroscience : the official journal of the Society for Neuroscience* 26 20, pp. 5470–83.

Van-Hecke, W., Emsell, L., and Sunaert, S., eds. (2016). *Diffusion Tensor Imaging A Practical Handbook*. Springer.

Velazquez-Perez, L. et al. (2014). "Comprehensive study of early features in spinocerebellar ataxia 2: delineating the prodromal stage of the disease." *Cerebellum* 13.5, pp. 568–79.

Wardlaw, J.M. et al. (2013). "Neuroimaging standards for research into small vessel disease and its contribution to ageing and neurodegeneration." *Lancet Neurol* 12.8, pp. 822–38.

Westover, M.B., Bianchi, M.T., Yang, C., Schneider, J.A., and Greenberg, S.M. (2013). "Estimating cerebral microinfarct burden from autopsy samples." *Neurology* 80 15, pp. 1365–9.

Winkler, A.M., Ridgway, G.R., Webster, M.A., Smith, S.M., and Nichols, T.E. (2014). "Permutation inference for the general linear model."

Wu, D., Li, G., Zhang, J., Chang, S., Hu, J., and Dai, Y. (2014). "Characterization of Breast Tumors Using Diffusion Kurtosis Imaging (DKI)." *PloS one*.

Wu, Y.T., Shyu, K.K., Chen, T.R., and Guo, W.Y. (2009). "Using three-dimensional fractal dimension to analyze the complexity of fetal cortical surface from magnetic resonance images." *Nonlinear Dynamics* 58, pp. 745–752.

Wu, Y.T., Shyu, K.K., Jao, C.W., Wang, Z.Y., Soong, B.W., Wu, H.M., and Wang, P.S. (2010). "Fractal dimension analysis for quantifying cerebellar morphological change of multiple system atrophy of the cerebellar type (MSA-C)." *NeuroImage* 49, pp. 539–551.

Xiong, L. et al. (2019). "Predictors for Late Post-Intracerebral Hemorrhage Dementia in Patients with Probable Cerebral Amyloid Angiopathy." *Journal of Alzheimer's disease : JAD*.

Zhang, H., Avants, B.B., Yushkevich, P.A., Woo, J.H., Wang, S., McCluskey, L.F., Elman, L.B., Melhem, E.R., and Gee, J.C. (2007a). "High-dimensional spatial normalization of diffusion tensor images improves the detection of white matter differences: an example study using amyotrophic lateral sclerosis." *IEEE Trans Med Imaging* 26.11, pp. 1585–97.

Zhang, H., Schneider, T., Wheeler-Kingshott, C.A.M., and Alexander, D.C. (2012). "NODDI: Practical in vivo neurite orientation dispersion and density imaging of the human brain." *NeuroImage* 61, pp. 1000–1016.

Zhang, L., Liu, J.Z., Dean, D., Sahgal, V., and Yue, G.H. (2006). "A three-dimensional fractal analysis method for quantifying white matter structure in human brain." *Journal of Neuroscience Methods* 150.3, pp. 243–253.

Zhang, L., Dean, D., Liu, J.Z., Sahgal, V., Wang, X., and Yue, G.H. (2007b). "Quantifying degeneration of white matter in normal aging using fractal dimension." *Neurobiology of Aging* 28, pp. 1543–1555.

Zhang, L., Butler, A.J., Sun, C.K., Sahgal, V., Wittenberg, G.F., and Yue, G.H. (2008). "Fractal dimension assessment of brain white matter structural complexity post stroke in relation to upper-extremity motor function." *Brain Research* 1228, pp. 229–240.

Zhao, G., Denisova, K., Sehatpour, P., Long, J., Gui, W., Qiao, J., Javitt, D.C., and Wang, Z. (2016). "Fractal Dimension Analysis of Subcortical Gray Matter Structures in Schizophrenia." *PloS one*.

Zou, H. and Hastie, T.J. (2005). "Regularization and variable selection via the elastic net." *Journal of the Royal Statistical Society. Series B*.